Investigation of High-Z Plasmas Extreme Ultraviolet and Soft X-ray Sources

Takamitsu Otsuka, M.Eng.

Thesis presented for the degree of
Doctor of Engineering

to the
Department of Innovation
Systems Engineering
Utsunomiya University

Research Supervisor
Prof. Noboru Yugami

Head of School
Prof. Tsukasa Ikeda

Contents

Chapter 1

Introduction

Sir Isaac Newton is credited with the first spectrographic experiment, establishing that white light is composed many colours. Classical physics including electromagnetics was expected to be universal and able to describe all physical phenomena. However, some disagreement was found at the end of 19th century. It lead to the establishment of quantum physics which can describe phenomena that can not be described using classical physics. Spectroscopy was a major contributor to the development of quantum theory.

In the author's view, it seems that the first laser oscillation by Maiman was another big turning point for the development of spectroscopy [1]. This big step in the progress of scientific technology allows us to easily make plasmas with temperatures of over 1,000,000 K in a small laboratory. Experimental results under such extreme conditions and numerical calculations by high performance computers allow us to develop modern spectroscopy, in the soft X-ray spectral (SXR) region.

About 350 years has been passed since the first spectrographic experiment, nevertheless, there are regions still under development, for example between the ultraviolet and SXR regions. Radiation in this region, however, has various applications. For example, lithography and SXR microscopy for biological imaging. Details of these applications are described in the following sections.

In this chapter, the basic characteristics of extreme ultraviolet (EUV) and SXR radiation are described. After that, applications of light sources in the EUV and SXR regions and the motivation for this research are also described.

1.1 Extreme Ultraviolet and Soft X-ray Radiation

In this section, the basic characteristics of EUV and SXR radiation are described. Figure 1.1 shows the electromagnetic spectrum from the infrared to the X-ray spectral region. The spectral region around 400-700 nm is called the visible region, which the human eye can see. The spectral region longer than the visible region is called infrared (IR), and the first spectral region shorter than the visible region is called ultraviolet (UV). At wavelength shorter than the UV, are the vacuum ultraviolet (VUV) and the EUV, but the definition of the divisions between two spectral regions are not clear. The last spectral region in the figure 1.1 is called the hard X-ray, which is used for medical X-ray. In this thesis, the spectral range of 5-40 nm (Photon energy: 30-250 eV) is defined as the EUV, and the photon energy range of 250 eV to several keV is defined as the SXR by reference [2].

Because the light in this region has sufficient photon energy to excite or remove inner shell electrons, both resonance and non-resonance absorption occur when the light interacts with materials. For example, as can be seen in 1.1, there are K-absorption edges of carbon and oxygen at 4.36 nm (284 eV) and at 2.28 nm (543 eV), respectively. The spectral region between these two K-absorption edges is called the water window, which is described in section 1.2.2.

Wavelength λ is mainly used in this thesis, however, photon energy $h\nu$ is useful for work on absorption and so on. Therefore, the following equations are

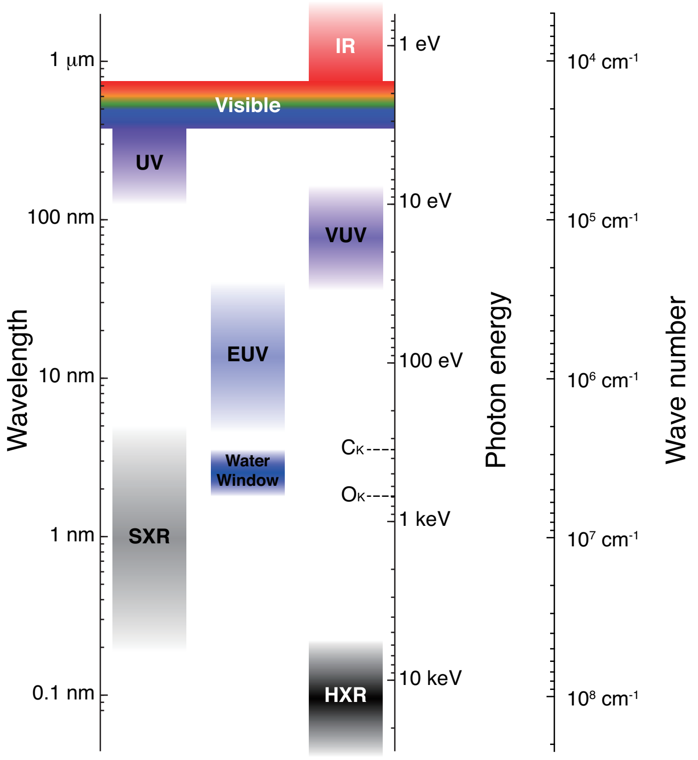

Figure 1.1 The electromagnetic spectrum

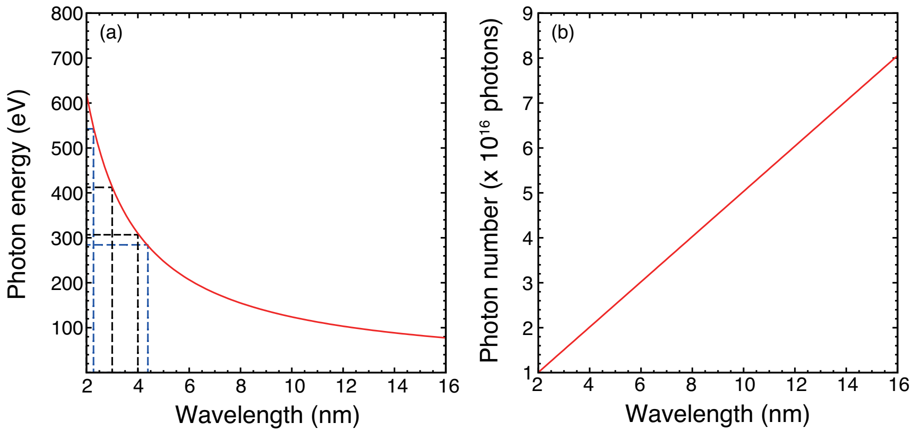

Figure 1.2 (a) Relationship between Wavelength (nm) and Photon energy (eV), (b) Photon number for 1 J.

useful to convert from wavelength to photon energy.

$$\hbar\omega \cdot \lambda = hc = 1239.842[\mathrm{eV}\cdot\mathrm{nm}] \tag{1.1}$$

$$\lambda[\mathrm{nm}] \simeq \frac{1240}{h\nu[\mathrm{eV}]} \tag{1.2}$$

Where c is the speed of light, ν and ω are frequency and angular frequency of the light. Equations 1.2 are derived from $c = \nu\lambda$ and $\omega = 2\pi\nu$. Using the relationship between the electron volt and the joule, the number of photons required for one joule of energy can be simply calculated by the following equation.

$$5.034 \times 10^{15}\lambda[\mathrm{nm}]\mathrm{photons} \tag{1.3}$$

And also, for one watt is

$$5.034 \times 10^{15}\lambda[\mathrm{nm}]\mathrm{photons/s}. \tag{1.4}$$

Figure 1.2 shows the relationship between photon energy and wavelength, and the number of photons required for one joule, which is calculated by equation 1.2 and 1.3. For example, for wavelength $\lambda = 2$ nm and $\lambda = 4$ nm, one joule of energy corresponds to a photon number of 1.5×10^{16} and 2.0×10^{16} photons [2].

1.2 Applications of EUV and SXR Radiation

Because EUV and SXR photons have relatively short wavelengths and high energies, which often correspond to inner-shell resonances in atoms, many applications in imaging and materials science use these spectral regions. In this section, the background of the most popular applications for EUV and SXR sources, which are extreme ultraviolet lithography (EUVL) and the SXR microscope, are described.

1.2.1 Extreme Ultraviolet Lithography: EUVL

Progress in the manufacture of semiconductor integrated circuits has provided significant changes to our lives. For example, initially, the use of a high-performance computer was limited to a very small number of people. But now, everyone can use such computers at home due to the price decrease that has occurred over decades. It is still fresh in the author's mind that the American army made a supercomputer using TV game machines. Also the spread of the internet all over the world allowed us to work from almost anywhere in there world. These development are as a result of progress in the manufacture of semiconductor integrated circuits and these technologies are considered as an important basic ingredient in modern life. Nowadays, the manufacturing of semiconductor integrated circuit technology is facing a significant challenge as the size of features created in silicon continues to shrink.

First of all, the word lithography is derived from the word lithograph which means a picture printed using a stone or metal block on which an image has been drawn with a thick substance that attracts ink. In the author's view, lithography

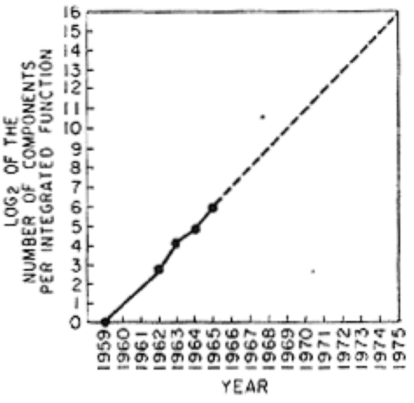

Figure 1.3 Moore's law

should be called photo lithography. As can be seen from the word, it is also important to develop an exposure source for the manufacture of semiconductors.

One of co-founders of the semiconductor integrated circuit manufacturer Intel, Gordon Moore, predicted in 1965 that the number of transistors on an integrated circuit chip would double every two years. Figure 1.3 shows Moore's law [3], and up to the present date, progress in the semiconductor integrated circuit is following the law. This progress is supported by development of lithography technology, especially photolithography. It is a technology in which a geometric pattern from a photomask is drawn on a light-sensitive chemical "photoresist", or simply "resist," deposited on the substrate, by radiation from a light source.

The achievable minimum line width R and depth of focus in a photolithography system are determined by the following equations based on Rayleigh's equation.

$$R = k_1 \frac{\lambda}{\mathrm{NA}} \tag{1.5}$$

$$\mathrm{DOF} = k_2 \frac{\lambda}{\mathrm{NA}^2} \tag{1.6}$$

where, k_1 and k_2 are constants which depend on the system (called process factors), λ is the wavelength of the source and NA is numerical aperture seen at the wafer. According to equation (1.5), there are three possibilities to improve the R, i.e. decrease the line width, (i) improve the process factor k_1, (ii) use shorter wavelength sources, (iii) use a large NA system. In photolithography, the half pitch (HP) size, which is the distance between identical features in an array, is often used instead of minimum line width R. Thus, in this thesis, HP sizes are used.

The first source used in photolithography technology was the g-line ($\lambda = 436\,\mathrm{nm}$) of the mercury (Hg) arc lamp. At that time the HP size was 2 µm and 1.3 µm. As the HP sizes were significantly larger than the wavelength of the light source, a small NA, $\mathrm{NA} = 0.28$, was used for manufacturing. With decreasing HP sizes required, the NA also improved. However, because the surface of the substrate was rough a deeper DOF was required. At the same time shorter wavelength sources were also required.

Therefore attention was focused on the krypton fluoride (KrF) laser operating at 248 nm in the deep ultraviolet (DUV) spectral region. However, the resists were not ready for KrF laser radiation at that time, so the i-line ($\lambda = 365\,\mathrm{nm}$) of mercury (Hg) arc lamp was used to make 0.8 and 0.5 µm chips and the further integration of semiconductor circuits continued. After the development of a suitable resist the KrF laser was used to manufacture chips at 0.25 µm. However, the wavelength of the KrF laser, which is 248 nm, is almost same as the size of the HP

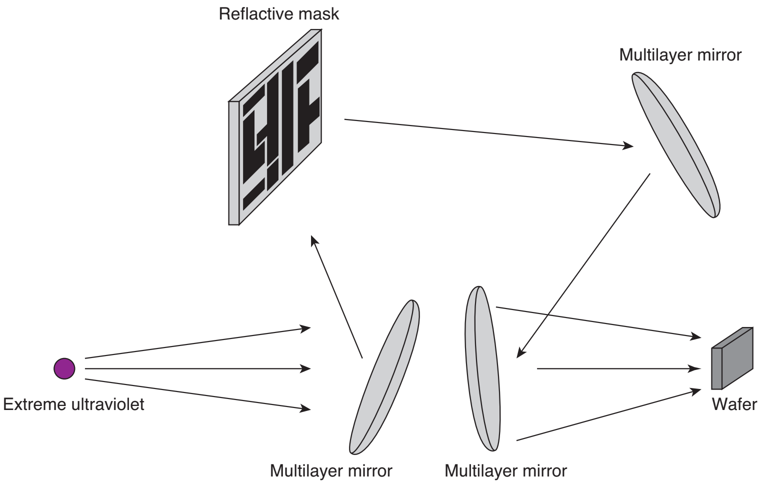

Figure 1.4 The basic concept of extreme ultraviolet lithography.

required at that time, so further techniques were investigated to achieve improved resolution.

As a result of such investigations, some new techniques were developed, such as a new design for the mask and control over the shape to be the source. In addition, k_1 was increased beyond 0.5 to 0.8. Theoretical k_1 is known about 0.25, thus improvement of the resolution was limited again. On the other hand, by improving the roughness of the wafer the limitations set by the wavelength and NA were mitigated. Recently, an argon fluoride (ArF) laser operating at 193 nm is in use for manufacturing. However, the required HP size is now under 30 nm which, being significantly smaller than the wavelength of the source, places massive technical challenges on the lithographers. The fluorine (F_2) laser was also investigated, for operation at 157 nm, but there are problems with the optics and resist materials.

These challenges were met by new technology such as phase shift, off axis illumination, water immersion optical lithography, source mask optimisation (SMO) and double patterning, to achieve improved minimum HP size. However, there are still limitations with regard to complex patterns, and the cost due to increased process times. To move to more feasible ways of creating sub 30-nm structures extreme ultraviolet lithography (EUVL) was investigated, particularly at 13.5 nm.

The first demonstration of extreme ultraviolet lithography was made by Kinoshita in 1986. It was a big jump and provided a potential solution for improved process time and resolution. However, to develop the manufacturing system there are many problems as new techniques and technologies are required to achieve extreme ultraviolet lithography, including source, optics and resist. Figure 1.4

shows the basic concept of extreme ultraviolet lithography. Only reflective optics are available for this spectral region thus even the mask must be made on a multilayer mirror. Problems include how to achieve a high-power extreme ultraviolet source and optical system design using multilayer mirrors [2, 4, 5].

In the development of EUVL sources, emission from lithium (Li), xenon (Xe) and tin (Sn) plasmas was investigated [6–10]. There two principal ways to produce plasmas, namely laser-produced plasma (LPP) [11–18] and discharge-produced plasma (DPP) [19–24].

At the early stage of EUV source development, a Xe-plasma based LPP source was considered to be the most appropriate source for EUVL. Because the conversion efficiency depends partially on the density of Xe, both jet and ice targets were investigated. However, the maximum conversion efficiency was approximately 1% [25–27]. At the EUVL symposium in Dallas in 2002, Sn plasma based EUV source were proposed by O'Sullivan and shown by JMar. Inc. After this workshop, source suppliers switched their forus to Sn from Xe and they soon achieved higher conversion efficiencies than from Xe sources. Nowadays, a CO_2 laser produced Sn plasma is employed as the optimum EUV source. Conversion efficiencies over 2% were reported using pre-pulse irradiation [25–27].

In the discharge produced plasma case, Xe gas was investigated as a fuel, and finally DPP was also converted to tin plasma. The conversion efficiency was improved by using tin plasma [25–27]. However, the maximum repetition rate was limited by heat conduction problems with the electrodes. This problem was partially solved by using a rotatable target supplier [23]. Recently, laser produced plasmas are also used in the discharge produced plasma source as a trigger, called LA-DPP (Laser assisted-DPP) [23, 24].

The requirement for the power of the EUVL source at intermediate focus (IF) is increasing and it is 250 W for the NXE 3300B and 350 for the NXE 3300C which are the EUVL systems being made by ASML. However, only about 150 W was achieved by a simple droplet scheme and not at a 100% duty cycle. Moreover some reports say that over 500 W will be required in the future. Thus, the present research goal is just to increase the power of the source [25–27].

Much of the academic research is almost complete for tin-based EUV sources. It is expected that the required HP size will continue to shrink in the future, so the next research direction should be the next generation source for the future EUVL. ASML have already made a road map for next generation EUVL sources, called beyond EUV (BEUV). The road map says the wavelength of the EUVL source will be around 6.x nm.

According to previous reports, it is known that gadolinium (Gd) and terbium (Tb) have the capability to emit at around 6.x nm [28]. Figure 1.5 shows time integrated emission spectra of gadolinium and terbium plasmas. Other elements, such as zirconium (Zr) and krypton (Kr) were also reported as eligible BEUV

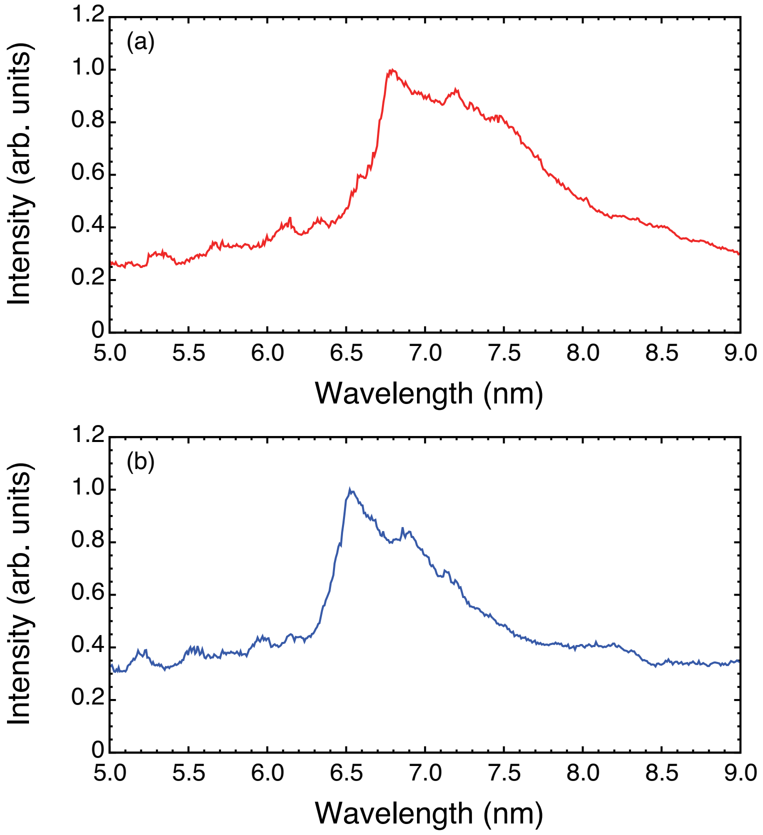

Figure 1.5 Time-integrated emission spectra from (a) gadolinium and (b) terbium plasmas.

sources [38, 39]. There are different multilayer mirrors proposed for 6.x nm based on the B_4C. However, the peak reflectivity is slightly off for the peaks of the emission from Gd and Tb plasmas. This is the big problem for BEUV lithography; how to solve the mismatch between the source and the mirrors.

In source research, it is important that we learn how to achieve a high power and high efficiency source. It is well known that emission spectra from high-Z plasmas have unresolved transition arrays (UTA) which can be attributed to hundreds of thousands of near-degenerate resonance lines, in a narrow band of the spectrum. Thus, intense emission can be obtained from high-Z plasmas at a particular spectral range. This is one of the reason why tin plasma based EUV source are employed in EUVL. Characteristics of UTA will be considered in the following chapter.

Emission spectra from Gd,Tb and Zr plasmas have already been investigated [29–39]. However, following from the research on tin-bsed plasma sources, it is also important to study the characteristics of plasma absorption, the photoabsorption cross-section and so on. In this thesis, experimental results for the absorption spectroscopy of Gd ions and numerical calculations are discussed.

1.2.2 The Water Window Microscope

One of the key applications of soft X-ray sources is biological imaging, in particular soft x-ray tomography (SXRT). The spectral range between the K-absorption edges of carbon (4.36 nm, 284 eV) and oxygen (2.28 nm, 543 eV), which is called the water window, is attractive for this purpose. As its name suggests, it is a spectral range where water has a transmissive window, but where carbon absorbs. Figure 1.6 shows the absorption length of water and a typical protein in the water window. It shows that protein has a shorter absorption length than water leading to the ability to image with good contast. The major constituents of biological cells and their absorption edges are shown in table 1.1. From the table, it can be seen that hydrogen, oxygen, carbon and nitrogen are the major constituents of biological cells, and that the others account for a small percentage. Therefore, a biological image can be taken by using sources at a wavelength in the water window under vacuum conditions without removal of water from the biological specimen [2].

The technique of biological imaging using water window light sources has been developed at radiation facilities, and biological images have been taken. There are two basic microscope types and each type has different strong and weak points.

Figure 1.7(a) shows one soft X-ray microscopy technique. Usually, a soft X-ray microscope consists of a condenser zone plate with a central stop and sample plane order sorting aperture (OSA) or stop, to illuminate the sample with first order radiation, and a micro zone plate with high numerical aperture which collects the transmitted and diffracted radiation, forming a high resolution, high magnifi-

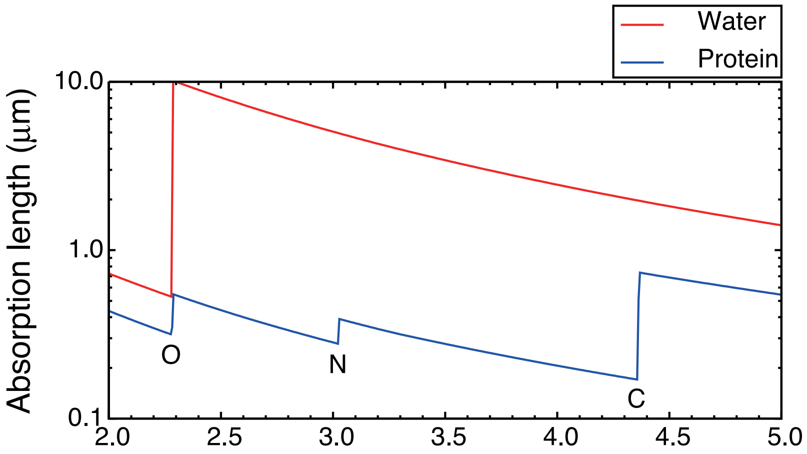

Figure 1.6 The absorption length for soft X-rays in water and protein

Table 1.1 The major constituents of biological cells and their absorption edges.

Element	Atomic number	% by weight	$\lambda_{K_{abs}}$ (nm)	$\lambda_{L_{abs}}$ (nm)
Hydrogen (H)	1	9.5	(91.1)	
Carbon (C)	6	18.5	4.36	
Nitrogen (N)	7	3.3	3.02	(33.5)
Oxygen (O)	8	65.0	2.28	(29.5)
Sodium (Na)	11	0.2	1.15	(40.0)
Magnesium (Mg)	12	0.1	0.95	(25.3)
Phosphorus (P)	15	0.2	0.57	(9.10)
Sulfur (S)	16	0.3	0.50	7.60
Chlorine (Cl)	17	0.2	0.43	6.2
Potassium (K)	19	0.4	0.34	4.20
Calcium (Ca)	20	1.5	0.30	3.58
Iron (Fe)	26	<0.01	0.17	1.75
Copper (Cu)	29	<0.01	0.13	1.32
Zinc (Zn)	30	<0.01	0.12	1.21
Iodine (I)	53	<0.01	0.03	0.27

cation (M $\sim$ 400 to 1000) image at the SXR CCD camera. The back focal plane of the micro zone plate is available for use as an annular phase plate. The advantages of the soft X-ray microscopy technique are its simplicity and ability to achieve high spatial resolution images. It does not require very spatially coherent radiation, generally forming images with bending-magnet radiation involving exposure times of a few seconds. On the other hand, the soft X-ray microscopy technique delivers a higher radiation dose to achieve a biological image [2].

Figure 1.7(b) shows a scanning soft X-ray microscope. Usually, the scanning scanning soft X-ray microscope consist a central zone plate stop and an order sorting aperture (OSA) to block all but the first order from reaching the specimen. The scanning soft X-ray microscope requires specially coherent light. The specially coherent light illuminates a zone plate lens, which forms a first order focal spot at the specimen plane. if perfectly illuminated and mounted, the zone plate provides an Airy pattern focal spot intensity distribution. The zeroth and other orders are stopped from reaching the specimen by a combination of a zone plate central stop and an order sorting aperture. Therefore the radiation dose to the specimen is minimized. The radiation transmitted through the specimen is then detected by a fast soft X-ray detector as the specimen is raster- scanned past the focal spot. The scanning soft X-ray microscope has flexibility and can be used a several modes.

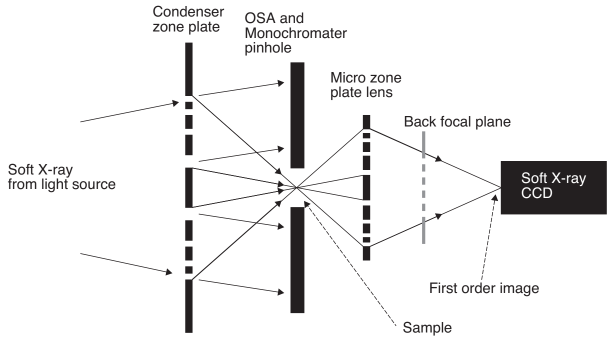

(a) The soft X-ray microscope

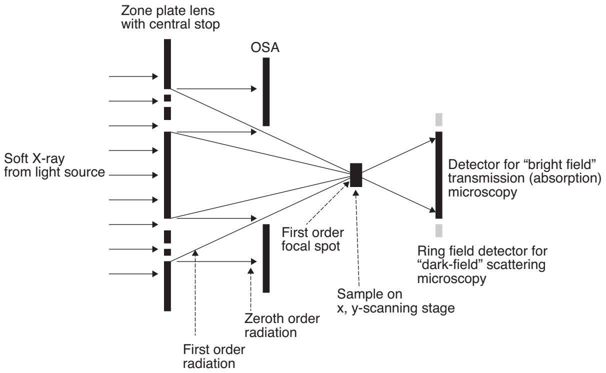

(b) Scanning soft X-ray microscope

Figure 1.7 The soft X-ray microscope (a) and the scanning soft X-ray microscope (b).

It can be used in the transmission mode, it can record specimen absorption versus position, repeated at various wavelengths for element and chemical analysis at a spectral resolution set by an upstream monochromator. It can also be used in a fluorescence or luminescence mode in which incident radiation excites or indirectly causes the emission of radiation that reveals the chemical nature of the specimen, or the presence of special molecular tags, again as a function of scanned position. A third mode of operation is that of detecting photoelectron emission as a function of position. The combination of the latter and photoelectron spectroscopy, at each scanned position, provides a powerful tool for the study of surface composition and chemistry. However, the scanning soft X-ray microscope has disadvantages, such as it needs coherent radiation and takes relatively long exposure time because of the significant loss of flux incurred through spatial flitering [2].

As can be seen from the above example, soft X-ray microscopy techniques are well developed. Soft X-ray sources, such as synchrotrons, are well developed technology, but cannot be used in a small laboratory. Thus, high power and high brightness compact soft X-ray sources are still under development for laboratory-

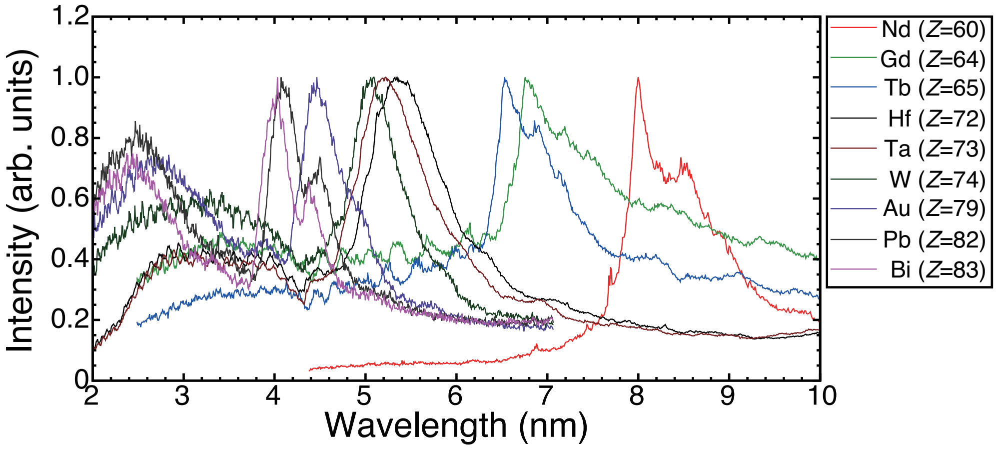

Figure 1.8 Time integrated EUV and SXR emission spectra from different target materials.

scale microscopy. There are some choices in laboratory-scale sources, e.g. X-ray lasers, high order harmonic generation (HHG) and plasma based sources. Sources in the water window region have been achieved with X-ray lasers and HHG, but they are not that compact or of high power. Also these sources are complicated because they are based on high power femto second laser systems. On the other hand, laser plasma-based soft X-ray sources are rather simple and smaller than the sources mentioned above.

H. M. Hertz and his colleague have demonstrated a soft X-ray microscope using a plasma-based soft X-ray source. They demonstrated compact full-field soft X-ray transmission microscopy with sub 60-nm resolution at $\lambda = 2.478$ nm in 2007. They used nitrogen Ly$_\alpha$ line emission at $\lambda = 2.478$ nm as the exposure source. Recently, they achieved a higher-high power, high-brightness nitrogen plasma based source and took an image of a biological cell in 2012. However, the shortest time for single exposure was 20 seconds. It was shown that a higher-power source is needed to take an image with single shot exposure [40, 41].

Compared to the nitrogen source, there is the possibility that intense soft X-ray emission can be obtained from a high-Z material-based soft X-ray source. Soft X-ray emission from high-Z materials has UTA structure, attributed to hundreds of thousands of near-degenerate resonance lines in $n = 4 - n = 4$ transitions. This may be of great interest if a high power source can be achieved using UTA emission for single shot biological imaging.

According to previous work, the UTA peak wavelength depends on the atomic number of the element forming the plasma(Z). Time integrated EUV and SXR spectra of neodymium (Nd: $Z = 74$), gadolinium (Gd: $Z = 64$), terbium (Tb:

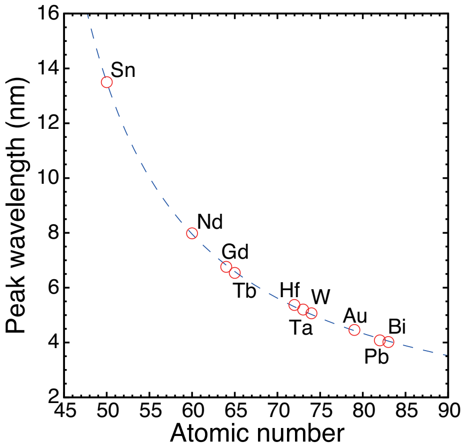

Figure 1.9 $n = 4 - n = 4$ UTA peak wavelength as a function of atomic number.

$Z = 65$), hafnium (Hf: $Z = 72$), tantalum (Ta: $Z = 73$), tungsten (W: $Z = 74$), gold (Au: $Z = 79$), lead (Pb: $Z = 82$) and bismuth (Bi: $Z = 83$) are shown in figure 1.8 below. As can be seen from figure 1.8, UTA peaks extend down towards the water window region. The position of the UTA peaks as a function of atomic number is shown in figure 1.9. From figure 1.9, the UTA peak of bismuth is located in the water window spectral region [42, 43].

Because the UTA contains a large number of resonance lines, it is expected that a high-power water window source can be achieved using a bismuth plasma. Note that, not only high power but also the spectral bandwidth is important for use with optics such as zone plates in the soft X-ray microscope. Thus, to achieve single shot biological imaging using UTA based soft X-ray sources, other optical components for construction of the soft X-ray microscope must be considered. However, only the characteristics of bismuth-based soft X-ray sources are discussed in this thesis.

1.3 Summary and Outline

The basic characteristics of EUV and SXR radiation are described in this chapter. As discussed, there is a wide variety of applications for these light sources at EUV and SXR wavelenghts. To achieve practical light sources, much research will be needed as in the case of tin plasma based 13.5-nm sources.

The emission spectra of Gd, Tb and Zr have already been investigated. However, as for tin plasma sources, it is also important that to study the characteristics of plasma absorption and ionic cross-sections, for example.

Shorter wavelength sources can not only be used for EUVL, but also material science and biological imaging near the water window. According to a previous work, it was shown that the UTA peak wavelength depends on atomic number and will therefore extend down towards the water window region. This may be of great interest if a high power source can be achieved using UTA emission. In this research, both emission and absorption spectroscopy were carried out on bismuth plasmas.

This thesis consists of 8 chapters. In chapter 2, plasma physics, atomic physics and some models are briefly described to allow for discussion of this research. The experimental apparatus employed in this research is described in chapter 3. Four different Nd:YAG lasers which deliver 7 to 10-ns and 150 to 170-ps pulses were employed to generate the plasmas. The details of different experimental setups are described in individual chapters. The experimental result are contained in chapters 4 to 7. In chapter 4, photabsorption spectra of Gd ions are shown with emission spectra and the results of numerical calculations. This experiment is a supplement to previous work of the Spectroscopy Group on the angular dependence of emission spectra [35]. Emission spectra from Bi plasmas and the dependence on laser power densities are shown in chapter 5. The results of dual-pulse irradiation experiments are described in chapter 6, while in chapter 7, photabsorption spectra of Bi ions are shown along with emission spectra and some numerical calculation results. The photabsorption spectroscopy of Gd and Bi ions was carried out by the author at University College Dublin.

Finally, main results from this thesis are summarised and an outlook towards future experiments is described in chapter 8.

Reference

[1] T. H. Maiman, ”Stimulated Optical Radiation in Ruby”, Nature, **187**, 493 (1960).

[2] D. Attwood, ”Soft X-Rays and Extreme Ultraviolet Radiation”, (Cambrige University press, 1999).

[3] G. E. Moore, ”Cramming more components onto integrated circuites”, Electronics, **38**, 114 (1965)

[4] V. Bakshi, ”EUV Sources for Lithography”, (SPIE Press Book, 2006).

[5] V. Bakshi, ”EUV Lithography”, (SPIE Press Book, 2008).

[6] A. Shimomura, T. Mochizuki, S. Miyamoto, S. Amano, and T. Uyama, ”Soft x-ray emission from laser plasma of cryogenic mixture targets”, Appl. Phys. Lett. **75**, 2026 (1999).

[7] S. Churilov, Y. N. Joshi, and J. Reader, ”High-resolution spectrum of xenon ions at 13.4 nm”, Opt. Lett. **28**, 1478 (2003).

[8] A. Sasaki, K. Nishihara, F. Koike, T. Kagawa, T. Nishikawa, K. Fujima, T. Kawamura, and H. Furukawa, ”Simulation of the EUV spectrum of Xe and Sn Plasmas”, IEEE J. Sel. Top. Quantum Electron. **10**, 1307 (2004).

[9] C. Rajyaguru, T. Higashiguchi, M. Koga, K. Kawasaki, M. Hamada, N. Dojyo, W. Sasaki, S. Kubodera, ”Parametric optimization of a narrow-band 13.5-nm emission from a Li-based liquid-jet target using dual nano-second laser pulses”, Appl. Phys. B, **80**, 409 (2005).

[10] T. Higashiguchi, K. Kawasaki, W. Sasaki, and S. Kubodera, ”Enhancement of extreme ultraviolet emission from a lithium plasma by use of dual laser pulses”, Appl. Phys. Lett. **88**, 161502 (2006).

[11] P. A. C. Jansson, B. A. M. Hansson, O. Hemberg, M. Otendal, A. Holmberg, J. Groot, and H. M. Hertz, ”Liquid-tin-jet laser-plasma extreme ultraviolet generation”, Appl. Phys. Lett. **84**, 2256 (2004).

[12] H. Tanaka, A. Matsumoto, K. Akinaga, A. Takahashi, and T. Okada, ”Comparative study on emission characteristics of extreme ultraviolet radiation from CO_2 and Nd:YAG laser-produced tin plasmas”, Appl. Phys. Lett. **87**, 041503 (2005).

[13] S. Fujioka, H. Nishimura, K. Nishihara, M. Murakamai, Y. Kang, Q. Gu, K. Nagai, T. Norimatsu, N. Miyanaga, Y. Izawa, and K. Mima, ”Properties of ion debris emitted from laser-produced mass-limited tin plasma for extreme ultraviolet source applications”, Appl. Phys. Lett. **87**, 241503 (2005).

[14] J. White, P. Hayden, P. Dunne, A. Cummings, N. Murphy, P. Sheridan, and G. O’Sullivan, ”Simplified modeling of 13.5 nm unresolved transition array emission of Sn plasma and comparison with experiment”, J. Appl. Phys. **98**, 113301 (2005).

[15] T. Okuno, S. Fujioka, H. Nishimura, Y. Tao, K. Nagai, Q. Gu, N. Ueda, T. Ando, K. Nishihara, T. Norimatsu, N. Miyanaga, Y. Izawa, and K. Mima, ”Low-density tin targets for efficient extreme ultraviolet light emission from laser-produced plasma”, Appl. Phys. Lett. **88**, 161501 (2006).

[16] J. White, P. Dunne, P. Hayden, F. O’Reilly, and G. O’Sullivan, ”Optimizing 13.5 nm laser-produced tin plasma emission as a function of laser wavelength”, Appl. Phys. Lett. **90**, 181502 (2007).

[17] J. White, G. O’Sullivan, S. Zakharov, P. Choi, V. Zakharov, H. Nishimura, S. Fujioka, and K. Nishihara, ”Tin laser-produced plasma source modeling at 13.5 nm for extreme ultraviolet lithography”, Appl. Phys. Lett. **92**, 151501 (2008).

[18] K. Nishihara, A. Sunahara, A. Sasaki, M. Nunami, H. Tanuma, S. Fujioka, Y. Shimada, K. Fujima, H. Furukawa, T. Kato, F. Koike, R. More, M. Murakami, T. Nishikawa, V. Zhakhovskii, K. Gamata, A. Takata, H. Ueda, H. Nishimura, Y. Izawa, N. Miyanaga, and K. Mima, ”Plasma physics and radiation hydrodynamics in developing an extreme ultraviolet light source for lithography”, Phys. Plasmas, **15**, 056708 (2008).

[19] M. Masnavi, M. Nakajima, A. Sasaki, E. Hotta and K. Horioka, ”Potential of discharge-based lithium plasma as an extreme ultraviolet source”, Appl. Phys. Lett. **89**, 031503 (2006).

[20] S. R. Mohanty, T. Sakamoto, Y. Kobayashi, N. Izuka, N. Kishi, I. Song, M. Watanabe, T. Kawamura, A. Okino, K. Horioka, and E. Hotta, ”Influence of electrode separation and gas curtain on extreme ultraviolet emission of a gas jet z-pinch douce”, Appl. Phys. Lett. **89**, 041502 (2006).

[21] T. Hosokai, T. Yokoyama, A. Zhidkov, H. Sato, K. Horioka, and E. Hotta, ”High brightness extreme ultraviolet (at 13.5 nm) emission from time-of-flight controlled discharges with coaxial fuel injection”, J. Appl. Phys. **104**, 053305 (2008).

[22] T. Hosokai, T. Yokoyama, A. Zhidkov, H. Sato, E. Hotta, and K. Horioka, ”Elongation of extreme ultraviolet (at 13.5 nm) emission with time-of-flight controlled discharges and lateral fuel injection”, J. Appl. Phys. **104**, 053306 (2008).

[23] K. Gielissen, Y. Sidelnikov, D. Glushkov, W. A. Soer, V. Banine, and J. J. A. M. v. d. Mullen, ”Characterization of ion emission of an extreme ultraviolet generating discharge produced Sn plasma”, J. Appl. Phys. **107**, 013301 (2010).

[24] I. Tobin, L. Juschkin, Y. Sidelnikov, F. O’Reilly, P. Sheriden, E. Sokell, and J. G. Lunney, ”Laser triggered Z-pinch broadband extreme ultraviolet source for metrology”, Appl. Phys. Lett. **102**, 203504 (2013).

[25] V. Y. Banine, K. N. Koshelev, and G. H. P. M. Swinkels, ”Physical processes in EUV sources for microlithography”, J. Phys. D: Appl. Phys. **44**, 253001 (2011).

[26] G. O’Sullivan, D. Kilbane and R. D’Arcy, ”Recent progress in source development for extreme UV lithography”, J. Mod. Opt. **59**, 855 (2012).

[27] T. Tomie, ”Tin laser-produced plasma as the light source for extreme ultraviolet lithography high-volume manufacturing: history, ideal plasma, present status, and prospects”, J. Micro/Nanolith. MEMS MOEMS, **11**, 021109 (2012).

[28] S. S. Churilov, R. R. Kildiyaraova, A. N. Ryabtsev, and S. V. Sadovsky, ”EUV spectra of Gd and Tb ions excited in laser-produced and vacuum spark plasmas”, Phys. Scr. **80**, 045303 (2009).

[29] T. Otsuka, D. Kilbane, J. White, T. Higashiguchi, N. Yugami, T. Yatagai, W. Jiang, A. Endo, P. Dunne, and G. O’Sullivan, ”Rare-earth plasma extreme ultraviolet sources at 6.5-6.7 nm”, Appl. Phys. Lett. **97**, 111503 (2010).

[30] A. Sasaki, K. Nishihara, A. Sunahara, H. Furukawa, T. Nishikawa, and F. Koike, ”Theoretical investigation of the spectrum and conversion efficiency of short wavelength extreme-ultraviolet light sources based on terbium plasma”, Appl. Phys. Lett. **97**, 231501 (2010).

[31] T. Otsuka, D. Kilbane, T. Higashiguchi, N. Yugami, T. Yatagai, W. Jiang, A. Endo, P. Dunne, and G. O’Sullivan, ”Systematic investigation of self-absorption and conversion efficiency of 6.7 nm extreme ultraviolet sources”, Appl. Phys. Lett. **97**, 231503 (2010).

[32] T. Higashiguchi, T. Otsuka, N. Yugami, W. Jiang, A. Endo, B. Li, D. Kilbane, P. Dunne, and G. O’Sullivan, ”Extreme ultraviolet sources at 6.7 nm based on a low-density plasma”, Appl. Phys. Lett. **99**, 191502 (2011).

[33] B. Li, P. Dunne, T. Higashiguchi, T. Otsuka, N. Yugami, W. Jiang, A. Endo, and G. O’Sullivan, ”Gd plasma source modeling at 6.7 nm for future lithography”, Appl. Phys. Lett. **99**, 231502 (2011).

[34] T. Cummins, T. Otsuka N. Yugami, W. Jiang, A. Endo, B. Li, C. O’Gorman, P. Dunne, E. Sokell, G. O’Sullivan, and T. Higahsiguchi, ”Optimizing conversion efficiency and reducing ion energy in a laser-produced Gd plasma”, Appl. Phys. Lett. **100**, 061118 (2012).

[35] C. O’Gorman, T. Otsuka, N. Yugami, W. Jiang, A. Endo, B. Li, T. Cummins, P. Dunne, E. Sokell, G. O’Sullivan, and T. Higashiguchi, ”The effect of viewing angle on the spectral behavior of a Gd plasma source near 6.7 nm”, Appl. Phys. Lett. **100**, 141108 (2012).

[36] B. Li, T. Otsuka, T. Higashiguchi, N. Yugami, W. Jiang, A. Endo, P. Dunne and G. O’Sullivan, ”Investigation of Gd and Tb plasmas for beyond extreme ultraviolet lithography based on multilayer mirror performance”, Appl. Phys. Lett. **101**, 013112 (2012).

[37] C. Suzuki, F. Koike, I. Murakami, N. Tamura, and S. Sudo, ”Observation of EUV spectra from gadolinium and neodymium ions in the Large helical Device”, J. Phys. B: At. Mol. Opt. Phys. **45**, 135002 (2012).

[38] B. Li, T. Higashiguchi, T. Otsuka, W. Jiang, A. Endo, P. Dunne, and G. O’Sullivan, ”XUV spectra of laser-produced zirconium plasmas”, J. Phys. B: At. Mol. Opt. Phys. **45**, 245004 (2012).

[39] M. Masnavi, J. Szilagyi, H. Parchamy, and M. C. Richardson, ”Laser-plasma source parameters for Kr, Gd, and Tb. ions at 6.6 nm”, Appl. Phys. Lett. **102**, 164102(2013).

[40] P. A. C. Takman, H. Stollberg, G. A. Johansson, A. Holmberg, M. Lindblom and H. M. Hertz, ”High-resolution compact X-ray microscopy”, J. Microsc. **226**, 175 (2007).

[41] H. Legall, G. Blobel, H. Stiel, W. Sandner, C. Semi, P. Takman, D. H. Martz, M. Selin, U. Vogt, H. M. Hertz, D. Esser, H. Sipma, J. Luttmann, M. Höfer, H. D. Hoffmann, S. Yulin, T. Feigl, S. Rehbein, P. Guttmann, G. Schneider, U. Wiesemann, M. Wirtz, and W. Diete, ”Compact x-ray microscope for the water window based on a high brightness laser plasma source”, Opt. Express, **20**, 18362 (2012).

[42] G. O’Sullivan and P. K. Carroll, ”$4d - 4f$ emission resonances in laser-produced plasmas”, J. Opt. Soc. Am. **71**, 227 (1981).

[43] D. Kilbane, ”Transition wavelengths and unresolved transition array statistics of ions with Z = 72-89”, J. Phys. B: At. Mol. Opt. Phys. **44**, 165006 (2011).

Chapter 2

Theory of Laser-produced Plasmas

In order to develop high power plasma based extreme ultraviolet (EUV) and soft X-ray (SXR) sources, it is necessary to investigate the peak emission wavelength and spectral intensity of a range of elements. The most important thing is understanding the complex physical mechanisms in high density and high temperature plasmas. In such a plasma, a large number of electrically-charged particles are contained which interact with each other. A plasma can be treated as a electromagnetic fluid.

The plasma electron temperature which is discussed in this thesis is of the order of 100 eV to several keV. Thus, the plasma expands rapidly after its creation. For an electron temperature of 1 keV, a plasma of electrons and silicon ions that is electrically neutral overall will expand at a velocity of order of 0.3 µm/ps. Thus the size of the plasma can be assumed to be on the order of 100 µm, after an expansion time of 300 ps. Due to such rapid expansion, the properties of the plasma, such as the gradients of electron density and temperature are changing significantly with time and cool down rapidly. Therefore, understanding the plasma physics is important in order to know how a high temperature can be achieved with a selected laser and element and what the consequent source size would be.

The two major ways to generate such high temperature plasmas, i.e. laser-produced plasma (LPP) and discharge-produced plasma (DPP) were investigated in the recent research into tin-plasma based 13.5 nm EUV sources. However, it is difficult to create a small plasma using a DPP. In contrast, the size of a LPP is of the order of 10 µm to several hundred µm. Recently, high power table top laser systems have been developed which allow one to generate high temperature - over hundred eV - plasmas in the laboratory, so laser produced plasmas were the basis of the research presented here.

In this chapter, some basic definitions of plasmas and physics of LPPs are described at first. After that atomic processes in plasmas are described. Previous PhD. theses are referred to in this chapter [1–4].

2.1 Plasma physics

2.1.1 Basic definitions of Plasma

In this subsection basic definitions of plasma are described. We don't encounter plasmas in normal everyday human activity, but it has often been said 99% of the matter in the universe is in the plasma state, i.e. rather, earth is an unusual environment. Plasma is called the fourth state of matter. It is assumed to be an electrified gas with the atoms dissociated into positive ions and negative electrons. It is reasonable view, however, this does not give the entire picture. A useful definition is "A plasma is a quasineutral gas of charged and neutral particles which exhibits collective behaviour.".

There are some important parameters required in order to understand plasmas. These are electron temperature T_e, electron density n_e, plasma frequency ω_p and the Debye length λ_D. Measuring and analysing these parameter is an important part of the process to understand plasmas generated.

Since T_e and the average kinetic energy E_av are so closely related, temperature is usually given in units of energy eV instead of K in plasma physics. The conversion factor is,

$$1\,[\mathrm{eV}] = 11600\,[\mathrm{K}]. \tag{2.1}$$

The electron density n_e relates to plasma frequency ω_p,

$$\omega_\mathrm{p} = \left(\frac{e^2 n_\mathrm{e}}{\varepsilon_0 m_\mathrm{e}}\right)^{1/2} \tag{2.2}$$

where e and m_e are the electronic charge and mass, respectively, and ε_0 is the permittivity of free space. This frequency is a characteristic frequency which is attributed to a processes where electrons are displaced, then overshoot and oscillate around their equilibrium positions in a plasma which has a uniform background of ions. It is important to consider the incidence of an electromagnetic wave, such as a laser pulse, into a plasma in terms of the plasma frequency. The electromagnetic wave can propagate in a plasma only if its frequency ω_laser is less than ω_p. Further characteristics are described in next subsection.

The Debye length λ_D is also an important property of the plasma. The electron temperature T_e and density n_e determine the Debye length

$$\lambda_\mathrm{D} = \left(\frac{\varepsilon_0 T_\mathrm{e}}{e^2 n_\mathrm{e}}\right)^{1/2}. \tag{2.3}$$

This definition gives a distance beyond which individual charge tend to be screened by the presence of other nearby, mobile charges [5, 6].

2.1.2 Laser-produced plasma

First, let us consider propagation of the electromagnetic wave in a plasma density of n_e without collision between electrons and ions. The electromagnetic wave which is propagating in the z direction can be described by

$$\boldsymbol{E} = \boldsymbol{E}_0 \exp[i(\boldsymbol{k} \cdot \boldsymbol{z} - \omega_0 t)]. \tag{2.4}$$

Where $\boldsymbol{k}$ is wave number, ω_0 is frequency of the electromagnetic wave. The electrons will accelerated by the electric field $\boldsymbol{E}$ of the electromagnetic wave, thus, the force equation of the velocity of the motion is

$$\frac{d\boldsymbol{v}_\mathrm{e}}{dt} = -\frac{e}{m_\mathrm{e}}\boldsymbol{E}. \tag{2.5}$$

Where $\boldsymbol{v}_\mathrm{e}$ is the velocity of the electron. The electric field $\boldsymbol{E}$ is changing as $\exp(-i\omega_0 t)$, thus, $d/dt = -i\omega_0$. Hence the velocity of the electron is described by

$$\boldsymbol{v}_\mathrm{e} = \frac{e\boldsymbol{E}}{i m_\mathrm{e}\omega_0} = -i\frac{e\boldsymbol{E}}{m_\mathrm{e}\omega_0}. \tag{2.6}$$

This velocity can be assumed as a current. From the definition of current density, $\boldsymbol{J}$, and equation (2.6), the following relation can be obtained.

$$\boldsymbol{J} = i\frac{n_\mathrm{e}e^2}{m_\mathrm{e}\omega_0}\boldsymbol{E} \tag{2.7}$$

Here, Maxwell's equations of electromagnetism are

$$\begin{aligned} \nabla \times \boldsymbol{B} &= \mu_0\boldsymbol{J} + \mu_0\varepsilon_0\frac{\partial \boldsymbol{E}}{\partial t} && (2.8) \\ \nabla \times \boldsymbol{E} &= -\frac{\partial \boldsymbol{B}}{\partial t}. && (2.9) \end{aligned}$$

Combining equations (2.7) and (2.8), and taking the curl,

$$\begin{aligned} \nabla \times \boldsymbol{B} &= i\mu_0\frac{n_\mathrm{e}e^2}{m_\mathrm{e}\omega_0}\boldsymbol{E} + \mu_0\varepsilon_0\frac{\partial \boldsymbol{E}}{\partial t} \\ \nabla \times (\nabla \times \boldsymbol{B}) &= i\mu_0\frac{n_\mathrm{e}e^2}{m_\mathrm{e}\omega_0}\nabla \times \boldsymbol{E} + \mu_0\varepsilon_0\frac{\partial \nabla \times \boldsymbol{E}}{\partial t} \\ &= -i\mu_0\frac{n_\mathrm{e}e^2}{m_\mathrm{e}\omega_0}\frac{\partial \boldsymbol{B}}{\partial t} - \mu_0\varepsilon_0\frac{\partial^2 \boldsymbol{B}}{\partial t^2} && (2.10) \end{aligned}$$

By using the vector relation $\nabla \times \nabla \times \boldsymbol{B} = \nabla(\nabla \cdot \boldsymbol{B}) - \nabla^2 \boldsymbol{B}$, and since $\nabla \cdot \boldsymbol{B} = 0$,

$$\nabla^2 \boldsymbol{B} = i\mu_0 \frac{n_{\mathrm{e}} e^2}{m_{\mathrm{e}} \omega_0} \frac{\partial \boldsymbol{B}}{\partial t} + \mu_0 \varepsilon_0 \frac{\partial^2 \boldsymbol{B}}{\partial t^2}. \tag{2.11}$$

Because $\nabla = -i\boldsymbol{k}$ and $\partial/\partial t = -i\omega_0$, the equation becomes

$$-k^2 \boldsymbol{B} = \mu_0 \frac{n_{\mathrm{e}} e^2}{m_{\mathrm{e}}} \boldsymbol{B} - \omega_0^2 \mu_0 \varepsilon_0 \boldsymbol{B}. \tag{2.12}$$

Recognising the speed of light, $c^2 = 1/\mu_0\varepsilon_0$, equation (2.12) becomes

$$\omega_0^2 = \omega_{\mathrm{p}}^2 + c^2 k^2. \tag{2.13}$$

This is the dispersion relation for a plasma.

Adapting in the same way equation (2.9), so that,

$$\begin{aligned}
\nabla \times \nabla \times \boldsymbol{E} &= -\frac{\partial(\nabla \times \boldsymbol{B})}{\partial t} \\
\nabla(\nabla \cdot \boldsymbol{E}) - \nabla^2 \boldsymbol{E} &= -i\mu_0 \frac{n_{\mathrm{e}} e^2}{m_{\mathrm{e}} \omega_0} \frac{\partial \boldsymbol{E}}{\partial t} - \mu_0 \varepsilon_0 \frac{\partial^2 \boldsymbol{E}}{\partial t^2} \\
\nabla^2 \boldsymbol{E} - \nabla(\nabla \cdot \boldsymbol{E}) - \frac{\omega_0^2}{c^2}\left(1 + \frac{\omega_{\mathrm{p}}^2}{\omega_0^2}\right)\boldsymbol{E} &= 0 \\
\nabla^2 \boldsymbol{E} + \frac{\omega_0^2}{c^2}\left(1 - \frac{\omega_{\mathrm{p}}^2}{\omega_0^2}\right)\boldsymbol{E} &= 0 \qquad (2.14)
\end{aligned}$$

Here,

$$\varepsilon = 1 - \frac{\omega_p^2}{\omega_0^2} \tag{2.15}$$

is the dielectric constant for the plasma.

The refractive index of the plasma n_{p} can be written as

$$n_{\mathrm{p}} = \frac{c}{v_{\mathrm{ph}}} = \frac{ck}{\omega_0} \tag{2.16}$$

Where v_{ph} is phase velocity. Combining with (2.13),

$$\frac{c^2 k^2}{\omega_0^2} = 1 - \frac{\omega_{\mathrm{p}}^2}{\omega_0^2} \tag{2.17}$$

can be obtained. Thus, the relationship between refractive index n_p and dielectric constant ε for the plasma is

$$n_\mathrm{p}^2 = \frac{c^2k^2}{\omega_0^2} = 1 - \frac{\omega_\mathrm{p}^2}{\omega_0^2} = \varepsilon. \tag{2.18}$$

Hence,

$$n_\mathrm{p} = \sqrt{1 - \frac{\omega_\mathrm{p}^2}{\omega_0^2}} \tag{2.19}$$

According to equation (2.19), it can be seen that there is a cutoff frequency in the plasma at $\omega_0 = \omega_\mathrm{p}$. Under the condition $\omega_0 < \omega_\mathrm{p}$, the refractive index becomes small, resulting in reflection of the electromagnetic wave. This can be understood by rewriting (2.17) as follows:

$$k = \frac{1}{c}\sqrt{\omega_0^2 + \omega_\mathrm{p}^2} = i\frac{1}{c}\sqrt{|\omega_0^2 + \omega_\mathrm{p}^2|} \tag{2.20}$$

In the highly overdense plasma, it can be assumed that as $\omega_0^2 \ll \omega_\mathrm{p}^2$, thus,

$$k = i\frac{\omega_\mathrm{p}}{c}. \tag{2.21}$$

the solution for k is imaginary, indicating that the electromagnetic wave cannot propagate in such an overdense plasma.

Under these conditions, the electric field can be described as

$$E \propto \exp(ikz) = \exp\left(-\frac{1}{c}\sqrt{|\omega_0^2 - \omega_\mathrm{p}^2|} \cdot z\right). \tag{2.22}$$

It depends spatially on z, and decreases in an exponential fashion. This length

$$\delta = \frac{c}{\sqrt{\omega_\mathrm{p}^2 - \omega_0^2}} \tag{2.23}$$

is called the penetration depth or skin depth. Recognising that $\omega_0^2 \ll \omega_\mathrm{p}^2$, the penetration depth in the overdense plasma is now given by

$$\delta = \frac{c}{\omega_\mathrm{p}}. \tag{2.24}$$

This relationship means that the electromagnetic wave can only penetrate to a depth of order δ and have an effect under the condition where $\omega_0^2 \ll \omega_\mathrm{p}^2$.

Table 2.1 Critical densities for some popular laser wavelength.

Laser	Wavelength (λ_0)	n_c(cm^{-3})
CO$_2$ laser	10.6 µm	1.0×10^{19}
Nd laser	1.06 µm	1.0×10^{21}
2ω of Nd laser	532 nm	4.0×10^{21}
3ω of Nd laser	355 nm	9.0×10^{21}
4ω of Nd laser	266 nm	1.6×10^{22}

The frequency at which $\omega_0 = \omega_\mathrm{p}$ is called the critical frequency, and the associated electron density is defined as the critical density, n_c. By using the plasma frequency, $\omega_\mathrm{p} = (e^2 n_\mathrm{e}/\varepsilon_0 m_\mathrm{e})^{1/2}$, the critical density is given by

$$\begin{aligned} n_\mathrm{c} &= \frac{\varepsilon_0 m_\mathrm{e} \omega_0^2}{e^2} \\ &= \frac{4\pi^2 c^2 \varepsilon_0 m_\mathrm{e}}{e^2 \lambda_0^2} \end{aligned} \tag{2.25}$$

In terms of the wavelength, equation (2.25) can be rewritten as

$$n_\mathrm{c} = \frac{1.12 \times 10^{21}}{\lambda_0^2}\ [\mathrm{cm}^{-3}]. \tag{2.26}$$

Where λ_0 is the wavelength of the electromagnetic wave in units of µm. Table 2.1 shows critical densities for some common laser wavelengths. As can be seen from the table, the critical densities of plasmas formed by the CO$_2$ laser and the Nd laser vary by a factor of one hundred.

Now, let us consider propagation of the electromagnetic wave where collisions occur between the electrons and ions. The electron which is accelerated by the electric field collides with ions in plasma. At this time, the equation of motion of the electron looks like

$$m_\mathrm{e} \frac{d\boldsymbol{v}_\mathrm{e}}{dt} = -e\boldsymbol{E} - m_\mathrm{e} \nu_\mathrm{ei} \boldsymbol{v}_\mathrm{e}. \tag{2.27}$$

Where, ν_ei is electron-ion collision frequency. The electron velocity can now be written as

$$\boldsymbol{v}_\mathrm{e} = -\frac{ie}{m(\omega + i\nu_\mathrm{ei})}\boldsymbol{E}. \tag{2.28}$$

And the current density, $\boldsymbol{J}$, can be written as,

$$\begin{aligned}\boldsymbol{J} &= -n_{\mathrm{e}} e \boldsymbol{v}_{\mathrm{e}} \\ &= \frac{i n_{\mathrm{e}} e^2}{m(\omega_0 + i\nu_{\mathrm{ei}})}\boldsymbol{E} \\ &= \frac{i\varepsilon_0 \omega_2^2}{\omega_0 + i\nu_{\mathrm{ei}}}\boldsymbol{E}. \end{aligned} \tag{2.29}$$

Recognising that $\boldsymbol{J} = \sigma\boldsymbol{E}$,

$$\sigma = \frac{i\varepsilon_0 \omega_2^2}{\omega_0 + i\nu_{\mathrm{ei}}} \tag{2.30}$$

can be obtained. Where σ is electric conductivity for the plasma. Here Maxwell's equations of electromagnetism can be rewritten as,

$$\begin{aligned}\nabla \times \boldsymbol{B} &= \mu_0 \boldsymbol{J} + \mu_0 \varepsilon_0 \frac{\partial \boldsymbol{E}}{\partial t} \\ &= \mu_0 \sigma \boldsymbol{E} + \mu_0 \varepsilon_0 \frac{\partial \boldsymbol{E}}{\partial t} \end{aligned} \tag{2.31}$$

$$\nabla \times \boldsymbol{E} = -\frac{\partial \boldsymbol{B}}{\partial t} \tag{2.32}$$

Proceeding in the same way as in the case of no electron ion-collisions, using Maxwell's equations,

$$\begin{aligned}\nabla \times \nabla \times \boldsymbol{B} &= -\mu_0 \sigma \frac{\partial \boldsymbol{B}}{\partial t} - \mu_0 \varepsilon_0 \frac{\partial^2 \boldsymbol{B}}{\partial t^2} \\ \nabla^2 \boldsymbol{B} &= \mu_0 \sigma \frac{\partial \boldsymbol{B}}{\partial t} + \mu_0 \varepsilon_0 \frac{\partial^2 \boldsymbol{B}}{\partial t^2} \\ -k^2 \boldsymbol{B} &= -i\mu_0 \sigma \boldsymbol{B} - \omega_0^2 \mu_0 \varepsilon_0 \boldsymbol{B} \end{aligned} \tag{2.33}$$

And recognising the speed of light, $c = 1/\mu_0\varepsilon_0$, again, the dispersion relationship for this case becomes,

$$\omega_0^2 = \omega_{\mathrm{p}}^2 \frac{\omega_0(\omega_0 - i\nu_{\mathrm{ei}})}{\omega_0^2 + \nu_{\mathrm{ei}}^2} + c^2 k^2. \tag{2.34}$$

Thus, for the case of $\nu_{\mathrm{e}} i \ll \omega_0$, the dispersion relationship can be modified as,

$$\omega_0^2 = \omega_{\mathrm{p}}^2 \left(1 - i\frac{\nu_{\mathrm{ei}}}{\omega_0}\right) + k^2 c^2. \tag{2.35}$$

By taking the curl of equation (2.32), the modified dielectric constant, ε_{p}, for the plasma can be obtained,

$$\begin{aligned}
\nabla \times \nabla \times \boldsymbol{E} &= -\frac{\partial \nabla \boldsymbol{B}}{\partial t} \\
\nabla(\nabla \cdot \boldsymbol{E}) - \nabla^2 &= -\mu_0 \sigma \frac{\partial \boldsymbol{E}}{\partial t} - \mu_0 \varepsilon_0 \frac{\partial^2 \boldsymbol{E}}{\partial t^2} \\
\nabla(\nabla \cdot \boldsymbol{E}) - \nabla^2 \boldsymbol{E} &= -\mu_0 \sigma(-i\omega_0)\boldsymbol{E} - \mu_0 \varepsilon_0 (-\omega_0^2)\boldsymbol{E} \\
\nabla^2 \boldsymbol{E} - \frac{\omega_0^2}{c^2}\left(1 - \frac{\omega_p^2}{\omega_0(\omega_0 + i\nu_{\mathrm{ei}})}\right)\boldsymbol{E} &= 0 \qquad (2.36)
\end{aligned}$$

$$\begin{aligned}
\varepsilon_{\mathrm{p}} &= 1 - \frac{\omega_{\mathrm{p}}^2}{\omega_0(\omega_0 + i\nu_{\mathrm{ei}})} \\
&= 1 - \frac{\omega_{\mathrm{p}}^2}{\omega_0^2 + \nu_{\mathrm{ei}}^2} - i\frac{\omega_{\mathrm{p}}^2 \nu_{\mathrm{ei}}}{\omega_0(\omega_0^2 + \nu_{\mathrm{ei}}^2)} \qquad (2.37)
\end{aligned}$$

A complex dielectric constant implies absorption occurs for the electromagnetic wave, due to the introduction of the electron-ion collision term.

This can be also understood using the dispersion relationship. Expressing $\omega_0 = \omega_{\mathrm{r}} + i\omega_{\mathrm{i}}/2$, and considering the condition where $\nu_{\mathrm{ei}} \ll \omega_0$, ω_{r} and ω_{i} are now given by

$$\begin{aligned}
\omega_{\mathrm{r}}^2 &= \omega_{\mathrm{p}}^2 + k^2 c^2 \qquad (2.38) \\
\omega_{\mathrm{i}} &\simeq -\frac{\omega_{\mathrm{p}}^2}{\omega_0^2}\nu_{\mathrm{ei}} \\
&= -\frac{n_{\mathrm{e}}}{n_{\mathrm{c}}}\nu_{\mathrm{ei}} \qquad (2.39)
\end{aligned}$$

ω_{r} corresponds to equation (2.13). The imaginary part ω_{i}, on the other hand, which has a negative sign, indicates damping. Thus, $(n_{\mathrm{e}}/n_{\mathrm{c}})\nu_{\mathrm{ei}}$ can be called the energy damping rate, and the electromagnetic wave will be damped by this rate in plasma. Physically, when the electromagnetic wave propagates through the plasma, its electric field induces an oscillation in the velocity of all electrons, superposed on their otherwise random motion. As the electrons experience collision with ions, their energy of oscillation is converted to random energy. This process leads to heating of the electrons to higher temperatures. Therefore, the intensity of the electromagnetic wave is decreasing while the thermal energy of the plasma increases. Expressing $k = k_{\mathrm{r}} + ik_{\mathrm{i}}/2$, let us consider the spatial profile also by using the dispersion relationship. k_r and k_i are given by,

$$k_\mathrm{r} = \frac{\sqrt{\omega_0^2 - \omega_\mathrm{p}^2}}{c} \tag{2.40}$$

$$\begin{aligned} k_\mathrm{i} &= \frac{\nu_\mathrm{ei}\omega_\mathrm{p}^2}{2c\omega_0\sqrt{\omega_0^2 - \omega_\mathrm{p}^2}} \\ &= \frac{\omega_\mathrm{p}^2}{2\omega_0^2}\frac{\nu_\mathrm{ei}}{v_\mathrm{g}} \end{aligned} \tag{2.41}$$

Where v_g is group velocity of the electromagnetic wave. The attenuation length for an intensity decay of $1/e$ is given by $2k^{-1}$, thus,

$$\begin{aligned} l_\mathrm{abs} = \frac{1}{2k_\mathrm{i}} &= \frac{\omega_0^2}{\omega_p^2}\frac{v_g}{\nu_{ei}} \\ &= \frac{n_\mathrm{c}}{n_\mathrm{e}}\frac{v_g}{\nu_\mathrm{ei}} \end{aligned} \tag{2.42}$$

This linear damping process is very important for the creation and heating of laser-produced plasmas. It is called collisional damping or inverse bremsstrahlung [6–8]. Johnston and Dawson performed a more accurate calculation of this absorption process by adopting an effective collision frequency describing the damping of the electromagnetic wave in the plasma [9, 10]. They showed the following absorption coefficient

$$\alpha_{\lambda_0} = \frac{13.5}{\lambda_0^2}Z\left(\frac{n_\mathrm{e}}{n_\mathrm{c}}\right)^2\frac{\ln\Lambda}{\sqrt{1-n_\mathrm{e}/n_\mathrm{c}}}\frac{1}{T_\mathrm{e}^{3/2}}\,[m^{-1}] \tag{2.43}$$

Where the wavelength λ in m, Z is the average plasma ion charge, Λ is the Coulomb logarithm. This absorption coefficient predicts that shorter wavelengths are more efficient for heating plasmas. However, the radiation emitted from the plasma may be absorbed by the plasma itself as the plasma density increases. Thus, the plasma must be considered from not only a fluid perspective but also from an atomic physics point of view.

2.2 Atomic processes in plasmas

It is well known that photons are emitted and absorbed during transitions from one energy state to another in an atomic system. To emit a photon the atom must be excited, after that the atom loses its excitation energy, transferring it to the emitted photon. In the high density and high temperature plasma, such as the ones discussed in this thesis, not only photo excitation but also collisional excitation and other processes must be considered.

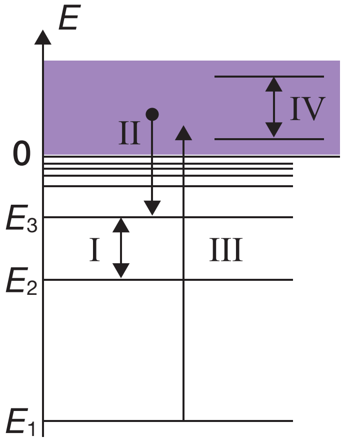

Figure 2.1 Energry level diagram for proton-electron system.

2.2.1 Mechanisms of emission and absorption

An energy level diagram of the most elementary atomic system is shown in figure 2.1. The zero energy level separates the free and bound states, as usual. In the bound states, it can be assumed that the electron can take only certain discrete energy values. In the case of a proton-electron system, the energy of the ground state is $E_1 = -13.6\text{eV}$, and its absolute value equals the ionisation potential of the hydrogen atom. In the free state, because the energy spectrum is continuous, it can be assumed that the electron can take any positive energy value. The energy spectrum of a complex atomic system not differ qualitatively from the spectrum of an elementary system. Transitions can be divided into three different groups, bound-bound, bound-free and free-free, determined by the initial and final state.

A bound-bound transition is defined as a transition from one discrete level to another. As each bound state has a different discrete energy level, these transitions result in the emission or absorption of line spectra. This transition type corresponds to I in figure 2.1.

In the case of a bound-free transition, the electron absorbs a photon and acquires an energy amount exceeding its binding energy leading to photoionisation. The excess energy above its binding energy is transformed into kinetic energy of the free electron. The inverse process, the capture of free electrons by ions results in the emission of photons. Since it can be assumed that a free electron can take any positive energy value, the bound-free transitions result in continuous and emission and absorption spectra. These transitions correspond to II and III in figure 2.1. Note that, not any arbitrary photon can cause photoionisation in an atom, i.e. the photon must have higher energy than the binding energy of the electron in its initial state. Even a photon with a very low energy, however, can remove the electron from a sufficiently excited atom, because the binding energy becomes less when excitation increases.

Free-free transitions occur when a free electron passes through the electric field of an ion, experiencing acceleration. At that time a free electron can emit a photon without losing all of its kinetic energy and remain a free electron. These free-free transitions are generally called bremsstrahlung, and are shown in figure 2.1 as IV. Because it is a transition from a continuum state to a continuum state, the emission and absorption result in continuous emission and absorption spectra. This type of transition also occurs when a free electron passes through the field of the neutral atom. However, the field of neutral atom decreases rapidly with distance, thus, the electron must pass very close to the atom to emit or absorb a photon. Therefore, this type of bremsstrahlung is less likely than bremsstrahlung resulting from an interaction between an electron and an ion.

Where absorption effects can be neglected, the total radiation coefficient η_ν can be written as,

$$\eta_\nu = \eta_\nu^{\mathrm{bf}} + \eta_\nu^{\mathrm{bb}} + \eta_\nu^{\mathrm{ff}} \tag{2.44}$$

where, η_ν^{bf}, η_ν^{bb}, η_ν^{ff} are the radiation coefficients of bound-free, bound-bound and free-free transitions, respectively. Note that, to compute actual emission from the plasma, the absorption coefficient, $\kappa_{\nu\mathrm{a}}$, and the scattering coefficient, $\kappa_{\nu\mathrm{s}}$, must be considered [11].

2.2.2 Fundamentals of atomic physics

The objective of this research is to characterise the emission and absorption spectra of high-Z plasmas. However, the configuration structure of multi-electron systems is complicated and it is not possible to obtain an exact solution. Instead an approximate solution must be found.

On the other hand, emission wavelengths of a one-electron system such as a hydrogen-like system are described by the following equation.

$$\frac{1}{\lambda} = Z^2 R \left(\left(\frac{1}{n_\mathrm{f}} \right)^2 - \left(\frac{1}{n_\mathrm{i}} \right)^2 \right) \tag{2.45}$$

Where Z is the charge of the nucleus, R is the Rydberg constant. n_f and n_i are the principal quantum numbers of the initial state and the excited states, respectively. This has explained the observed spectra of hydrogen, including the Lyman, Balmer and Paschen series.

Bohr proposed a quantum condition

$$\oint p_\theta d\theta = nh \, (n = 1, 2, 3, ...) \tag{2.46}$$

for an electron in the hydrogen atom. The kinetic state determined by this quantum condition is called a steady state. Bohr also proposed that the emission and absorption frequencies resulting from transitions between two different steady states are given by

$$h\nu = E_{\mathrm{i}} - E_{\mathrm{f}}. \tag{2.47}$$

Where h is Planck's constant, and E_{f} and E_{i} are energies of initial and final-state determined by

$$E_n = -\frac{m_{\mathrm{e}} Z^2 e^4}{32\pi^2 \varepsilon_0^2 \hbar^2} \frac{1}{n^2} \simeq \frac{13.606 Z^2}{n^2} \text{ [eV]}. \tag{2.48}$$

Where $\hbar$ is the Dirac constant, and n is the principal quantum number.

These equations could describe quantum mechanics well for a hydrogen-like systems. However, one must consider the orbital quantum number and magnetic quantum number in order to describe complex atomic structure in a more accurate way. The orbital quantum number l gives an orbital angular momentum L

$$L^2 = l(l+1)l\hbar^2. \tag{2.49}$$

l is quantised as below.

$$l = 0, 1, 2, 3, ..., n-1 \tag{2.50}$$

The magnetic quantum number m_l is a projection of an angular momentum vector, usually on the z axis.

$$M = m_l \hbar \tag{2.51}$$

m_l is also quantised by l, like below.

$$-l, -l+1, -l+2, ..., 0, ..., l-2, l-1, l \tag{2.52}$$

Thus, m has $2l+1$ projections.

It had been expected that these quantum numbers could fully describe quantum mechanics, but this was was not the case. Uhlenbeck and Goudsmit had proposed the concept that the spin angular momentum of the electron is also quantised. This spin angular momentum s can take eigenvalues of $\pm\hbar/2$. This proposal described why sodium's D line has two dominant spectral lines lying very close together.

These quantum numbers and Pauli's exclusion principle determine the rules for an electron orbit. Pauli's exclusion principle states that one cannot have the same set of quantum numbers for two fermions. Electrons are fermions, thus, there are $2 \times (2l+1)$ electrons in a full orbital. It can be seen from this subsection, for multi-electron systems, that it is not easy to even get an approximate solution [12].

2.2.3 Theory of atomic structure

In this subsection, the atomic structure of one electron and multi-electron atom are described.

If the electron can be described by a wave function, ψ, the time dependant Schröedinger equation is given by the following.

$$H\psi = i\hbar\frac{d\psi}{dt} \tag{2.53}$$

Where H is the Hamiltonian operator and is given by

$$H = -\frac{\hbar^2}{2m_\mathrm{e}}\nabla^2 + V \tag{2.54}$$

Because H depends on time, the wave function may be separated into its time independent and its time dependent parts. Assuming the wave is monochromatic with frequency ω_0,

$$\psi = \varphi(\boldsymbol{r})e^{-i\omega_0 t}. \tag{2.55}$$

From the combination of equation (2.53) and (2.55), the following equations can be obtained.

$$H\psi = H\varphi(\boldsymbol{r})e^{-i\omega_0 t} = \{H\varphi(\boldsymbol{r})\}e^{-i\omega_0 t} \tag{2.56}$$

$$i\hbar\frac{\partial\psi}{\partial t} = \varphi(\boldsymbol{r})i\hbar\frac{\partial e^{-i\omega_0 t}}{\partial t} = \hbar\omega_0\varphi(\boldsymbol{r})e^{-i\omega_0 t} \tag{2.57}$$

Assuming $E = \hbar\omega_0$, equation (2.53) can be rewritten as,

$$H\varphi(\boldsymbol{r}) = E\varphi(\boldsymbol{r}). \tag{2.58}$$

This is the Schrödingier's equation for the steady state. For a hydrogen-like system, the potential is given by,

$$V(r) = \frac{1}{4\pi\varepsilon_0}\frac{Ze^2}{r}. \tag{2.59}$$

Thus, the hamiltonian for hydrogen-like system is,

$$H = -\frac{\hbar^2}{2m_\mathrm{e}}\nabla^2 - \frac{Ze^2}{4\pi\varepsilon_0 r}. \tag{2.60}$$

We should use the reduced mass, which is described by $m_\mathrm{e}M/(m_\mathrm{e} + M)$, where M is the mass of the nucleus. But, if M is sufficiently heavier than m_e, $m_\mathrm{e} \ll M$, thus it can be assumed that the reduced mass is equal to m_{e}. The eigenfunctions of a hydrogen-like system are described using radial wave functions $R_{nl}(r)$ and spherical harmonics $Y_l^{m_l}(\theta,\phi)$,

$$\phi_{n,l,m_l}(r,\theta,\phi) = R_{n,l}(r)Y_l^{m_l}(\theta,\phi) = \frac{1}{r}P_{nl}(r)Y_l^{m_l}(\theta,\phi). \tag{2.61}$$

It can be seen from equation (2.61), that the wave function of a hydrogen-like system is quantised by n, l and m_l. It is well known that the exact solution can be obtained for only a hydrogen-like system.

For a multi-electron system the Hamiltonian must contain terms describing the interaction between electrons as well as the interaction of each electron with the nucleus. Thus, the Hamiltonian looks like,

$$H = \sum_i \left[-\frac{\hbar^2}{2m_{\mathrm{e}}}\nabla_i^2 - \frac{1}{4\pi\epsilon_0}\frac{Ze^2}{r_i} \right] + \sum_{i<j}\frac{1}{4\pi\epsilon_0}\frac{e^2}{r_{ij}}. \tag{2.62}$$

Where r_i is the distance from the nucleus to the ith electron, and r_{ij} is the distance from the ith electron to the jth electron, $r_{ij} \equiv |\boldsymbol{r}_i - \boldsymbol{r}_j|$. This is a multi-body problem and can not be solved to give an exact solution as in the case of a hydrogen-like system [12].

2.2.4 Approximation methods and coupling schemes

To solve a multi-body problem, some approximation methods have been developed. One of these is the central field approximation, which was developed by Hartree. Since the electron interaction contains a large spherically symmetric component arising from core electrons, the closed shell has a spherically symmetric charge distribution, as follows

$$\sum_{m=-l}^{l} = |Y_l^{m_l}(\theta,\phi)|^2 = \text{const.} \tag{2.63}$$

Thus, the approximation assumes the final term of equation (2.62) as $U_{\mathrm{i}}(r_{\mathrm{i}})$, which is a spherical function which represents a central radially symmetric field due to interaction between the electron and all other electrons. The basic idea of Hatree's method is that the wave function is not antisymmetric with respect to interchange of two coordinate sets i and j thus disobeying the Pauli principle. Fock addressed this problem by incorporating the spin into new one-electron functions and replacing the simple product function with an antisymmetrised product. This method is known as the Hatree-Fock method. These assumptions are less certain for atoms where there is an open subshell.

To deal with this question, we must consider spin-orbit and residual Coulomb interactions between outer electrons. Thus, the Hamiltonian for multi-electron system can be written as,

$$\begin{aligned} H &= H_0 + H_1 + H_2 && (2.64) \\ H_0 &= \sum_i \left[-\frac{\hbar^2}{2m_\mathrm{e}} \nabla_i^2 - \frac{1}{4\pi\epsilon_0} \frac{Ze^2}{r_i} + U_i(r) \right] && (2.65) \\ H_1 &= \sum_{i<j} \frac{1}{4\pi\epsilon_0} \frac{e^2}{r_{ij}} - \sum_i U_i(r) && (2.66) \\ H_2 &= \sum_i \xi_i(r_i) \boldsymbol{L}_i \cdot \boldsymbol{S}_i && (2.67) \end{aligned}$$

where H_0 includes central field terms, H_1 is residual Coulomb interaction, and H_2 is the spin-orbit interaction. ξ_i is given by

$$\xi(r_i) = \frac{1}{2m_\mathrm{e}^2 c^2} \frac{1}{r_i} \frac{dV(r_i)}{dr_i}. \tag{2.68}$$

For light atoms, $H_1 \gg H_2$, H_2 can be assumed as a perturbation on $H_0 + H_1$. It is known as the LS or Russell-Saunders coupling regime. For heavy atoms or ionised light atoms, $H_2 \gg H_1$, electrons become relativistic and the spin-orbit interaction dominates. It is known as the jj coupling regime. These approximations allow us to solve the multi-body problem *via* a perturbation technique [12].

2.2.5 Oscillator strength

An important parameter of spectroscopy is the oscillator strength. Usually the weighted oscillator strength gf is used, where g is a statistical weight and f is the oscillator strength. Using the dipole approximation the oscillator strength for a transition between states i and j is given by,

$$f_{ij} = \frac{2}{3} \frac{m_\mathrm{e}}{\hbar^2} (E_j - E_i) |\langle \psi_i | \boldsymbol{r} | \psi_j \rangle|^2 \tag{2.69}$$

where $E_\mathrm{j} - E_\mathrm{i}$ is the transition energy. A more general expression of the oscillator strength is

$$f_{i \to j} = \frac{gf}{2J_i + 1} \tag{2.70}$$

where J_i is the total angular momentum of the initial state i. Then, the gf-value for a transition from some lower level i to a level j is given by,

$$gf = \frac{1}{3}(E_j - E_i)S \tag{2.71}$$

where $E_j - E_i$ in Rydbergs. The quantity S is called the line strength [12]. This is an important parameter to predict and it lets us know how strongly absorption or emission occurs in an experiment.

2.2.6 Wave function collapse and unresolved transition array

Wave function collapse is an important phenomenon to discuss in order to understand the emission and absorption spectra of high-Z materials. The process of wave function collapse is where an eigenstate of the outer well of the function suddenly becomes an eigenstate of the inner one with increasing ionisation along an isonuclear or isoelectronic sequence and not just with increasing Z.

The effective potential of the outer electron and radial wave function are described by,

$$V_{\mathrm{eff}} = V_{\mathrm{Coulomb}} + \frac{l(l+1)\hbar^2}{2m_{\mathrm{e}}r^2} \tag{2.72}$$

$$\frac{d^2P_{nl}(r)}{dr^2} = [V_{\mathrm{eff}}(r) - E]P_{nl}(r) \tag{2.73}$$

where l is the orbital angular momentum of the electron and r is the distance from the nucleus. This effective potential consist of a Coulombic term dependent on the nuclear charge and a centrifugal term which for large r, signifies that the electron experiences an essentially hydrogen like potential due to the shielding from the nucleus by the other electrons $(Z - 1)$. Thus, the shape of V_{eff} strongly depends on Z, and as Z increases, there is the formation of an inner well. As Z increases still further, the inner well gets wider and deeper and is separated from the outer well by a centrifugal barrier. Thus the wave function comes closer to the core with increasing Z [12, 13].

This wave function collapse can lead to degeneracy of the energy levels. For the case of $4f$ wave function collapse, it leads to degeneracy of the $4f$, $5p$ and $5s$ energy levels, resulting in the generation of complex atomic configurations. Emission lines due to transitions between the complex atomic configurations are so close in wavelength as to be impossible to separate. Thus, emission spectra becomes an array containing hundreds of thousands of lines [14]. Note that this dense array is not only due to instrument limitation but also the physical atomic processes. These spectral arrays are called unresolved transition arrays (UTA).

A statical method of parameterizing the UTA had already been developed by previous researchers [15–17]. This method allowed the UTA to be modelled with only a few parameters and without a line by line calculation. The UTA statistics can be described by using centred moments μ_{n},

$$\mu_n = \frac{\sum\limits_{i=1}^{N} (\lambda_i)^n g f_i}{\sum\limits_{i=1}^{N} g f_i}. \tag{2.74}$$

The mean position of the array is μ_1 and its root-mean-square deviation, the square root of its variance which determines the full width half maximum (FWHM) is

$$v = \mu_2 - (\mu_1)^2. \tag{2.75}$$

2.2.7 Atomic code

To compute such complex atomic structure, some computer programs have been developed, such as Cowan's atomic structure code, Flexible Atomic Code (FAC) and so on. In the work described in this thesis Cowan's atomic structure code was employed.

The Cowan code was developed by Robert D. Cowan at Los Alamos in 1968 to solve the multi-electron, Schrödinger wave equation. It consist of four FORTRAN programs (RCN36, RCN2, RCG and RCE). RCN is the first stage of the code which calculates the wave functions for each configuration. RCN2 calculates multi-configuration radial integrals and quantities required to calculate energy levels and spectra, which are then calculated in RCG. Finally, RCE calculates a least-squares fit using scaling of Slater-Condon parameters to match theoretical results to experiment. The Cowan code uses a self-consistent Hartree-Fock method, which starts with an approximate solution for the wave-function and iterates until the change is less than a given tolerance. Further information is given in [18].

2.2.8 The time dependent local density approximation: TDLDA

In order to calculate a numerical solution for the shape resonances, various methods were established. Altick and Glassgold applied the random phase approximation (RPA) to atomic physics [19]. It had first been used to describe many-body problems where there were an infinite number of particles, such as in an electron gas. After that, it was established that the random phase approximation with exchange (RPAE), which is an extended version of the RPA by accounting for interchannel interactions and time dependent local density approximation (TDLDA) which is used for analysis in this thesis.

The local density approximation (LDA) is one of the practical approaches aiming to obtain an approximate solution of the familiar many-electron Schrd̈inger equation which was reported by Kohn and Sham [20]. It replaces the correct many electron Hamiltonian with an approximate total energy functional, which is then varied leading to a set of one-electron Schrödinger equations that can then be solved numerically with little or no further approximation.

The time dependent local density approximation (TDLDA) is simply an extension of the LDA towards time dependant processes. The TDLDA code solves the LDA one-electron equations for an atom or ion in a stationary state and by an iterative process determines the self-consistent charge density and the potential function. One solves the TDLDA equations for the absorption of light using a relaxation procedure. The photoabsorption cross section $\sigma(\omega)$ is then obtained from the frequency dependent atomic polarisability $\alpha\omega$ using $\sigma(\omega) = 4\pi(\omega/c)\text{Im}[\alpha(\omega)]$. The effective number of electrons taking part in the photoabsorption process is allowed to be non-integral, a consequence of one of the approximations made in the TDLDA formalism being the setting of fractional values for the occupation of states in atoms with open shells. This use of fractional occupation numbers is to enable the modelling of both open and closed shell atoms as spherically symmetric. A closed shell atom or ion naturally has a spherically symmetric charge density and potential function. Thus a fractional occupation number for open shells allows spherical symmetry to be maintained in open shell atoms or ions.

There are two main TDLDA codes in use. Code for non-relativistic conditions developed by Zangwill and Soven, and for relativistic conditions by Parpia and Johnson [21, 22]. It has been successfully used to account for $4d \rightarrow \varepsilon f$ shape resonances in tin and tellurium [23, 24]. Further information about these codes is available in references [21, 22].

2.3 Equilibrium in plasmas

There are a large number of atomic processes in plasmas, including collisional and radiative ionisation, recombination, excitation and de-excitation. To understand emission from plasmas it is important to simulate these processes. In this section, atomic processes in plasmas and three widely-used models to calculate these processes are described.

2.3.1 Ionisation, excitation and the inverse processes in plasmas

The emission from high density and high temperature plasmas is rather more complicated than the simple mechanism described in the preceding subsection. It is

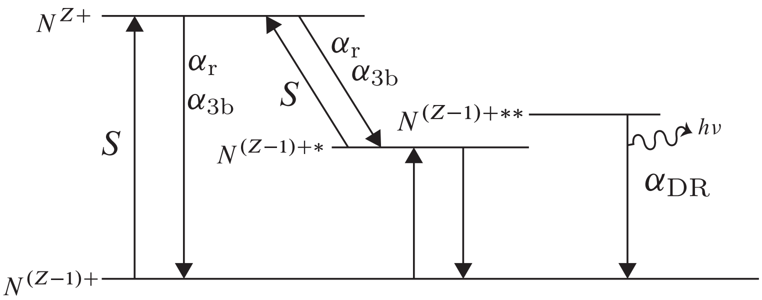

Figure 2.2 Simple diagram of main atomic processes in laser-produced plasma.

Table 2.2 Excitation and ionisation processes in plasmas.

Process	Reaction
Photoionisation (S)	$N^{(Z-1)+} + h\nu \rightarrow N^{Z+} + e$
Collisional ionisation (S)	$N^{(Z-1)+} + e \rightarrow N^{Z+} + e + e$
Autoionisation	$N^{(Z-1)+} + h\nu \rightarrow N^{(Z-1)+**} \rightarrow N^{Z+} + e$
Collisional excitation (X)	$N^{(Z-1)+} + e \rightarrow N^{(Z-1)+*} + e^{*}$
Photoexcitation (X)	$N^{(Z-1)+} + h\nu \rightarrow N^{(Z-1)+*}$

determined by a large number of atomic processes, collisional and radiative ionisation, recombination, excitation and de-excitation.

Table 2.3 De-excitation and recombination processes in plasmas.

Process	Reactin
Radiative recombination (α_{r})	$N^{Z+} + e \rightarrow N^{(Z-1)+} + h\nu$
Three body recombination ($\alpha_{3\mathrm{b}}$)	$N^{Z+} + e + e \rightarrow N^{(Z-1)+} + e$
Dielectronic recombination (α_{DR})	$N^{Z+} + e \rightarrow N^{(Z-1)+**} \rightarrow N^{(Z-1)+} + h\nu$
Collisional de-excitation (Y)	$N^{(Z-1)+*} + e^{*} \rightarrow N^{(Z-1)+} + e$
Photo de-excitation (Y)	$N^{(Z-1)+*} \rightarrow N^{(Z-1)+} + h\nu$

Figure 2.2 shows a simple diagram of the main atomic processes in a laser-produced plasma. Reaction formulae are shown in tables 2.2 and 2.3. Each process has its inverse, for example photoionisation and radiative recombination, and so on [8].

To compute the emission from a plasma, all processes should be calculated over many energy levels and several ionisation stages. It is complicated to simulate the emission by including all processes, however, there are some appropriate models for particular situations, which are discussed in following subsections.

2.3.2 Local thermodynamic equilibrium (LTE) model

The local thermodynamic equilibrium (LTE) model is one of the standard models which uses plasma thermodynamics. The LTE model assumes that the rates of collisional ionisation, electron impact excitation and de-excitation, electron impact ionisation, and its inverse, three body recombination are equal. On the other hand, equilibrium of the rates of photo-excitation, photo de-excitation, photo-ionisation, and radiative recombination is not assumed. Thus, the LTE model is an appropriate equilibrium model for plasmas in which the electron density is sufficiently high for collisional processes to dominate [8].

2.3.3 Coronal equilibrium (CE) model

The coronal equilibrium (CE) model may be applied to a very low density plasma, like the solar corona. In very low density plasmas the collisional rate is very low and excited states will generally decay through radiative processes. Assuming that the plasma is optically thin, photoionisation and photo-excitation are unlikely to occur, thus, detailed balance does not apply. Equilibrium will be determined between collisional excitation and spontaneous radiative decay. Under such a conditions it can be assumed that nearly all of the ions are in their ground state, and that the collisional excitation from the ground state is balanced by radiative decay from the upper energy level to all the lower levels. Also, there is no three-body recombination. Therefore, the CE model is an appropriate equilibrium model for plasmas in which the electron density is sufficiently low for the rate of collisional transition from an excited state to be far lower than the rate of radiative decay from that state [8].

2.3.4 Collisional radiative equilibrium (CRE) model

The collisional radiative equilibrium (CRE) model is intermediate between the previous two models, i.e. the LTE and CE models are approximations of the CRE model for the case when collisions dominate the radiative terms (LTE) and when the radiative rate dominates the collisional de-excitation (CE) interactions. The CRE model is the most appropriate model for a typical high-power laser generated plasma which has high density and temperature, such as the ones discussed in this thesis [8]. A steady state CRE plasma model was developed by Colombant and Tonon, in which the following three principal conditions must hold for the steady state collisional model to hold [25].

a). The first condition is very general and is characteristic of all plasma radiation models: The velocity distribution of the electrons must be Maxwellian.

b). The second condition is that the population density of ions of charge (Z + 1) must not change significantly during the period when the quasisteady-state population distribution is being established among the ions of charge Z.

c). The plasma must be optically thin to its radiation.

For condition (a) to hold, the elecron-electron relaxation time must be smaller than the electron heating time. In LPPs, such as the ones discussed in this thesis, electron densities are very high, up to 10^{21}cm^{-3} in the case of an Nd:YAG laser plasma. Their relaxation time is much smaller than any other characteristic time, therefore, condition (a) holds for plasmas discussed in this thesis.

For comparison, the criteria for the applicability of different models to laser-produced plasmas are shown in figure 2.3. For the plasmas discussed in this thesis, electron densities are up to 10^{21}cm^{-3} and electron temperatures are up to greater than 100 eV. Condition (b) appears as the line on the left-hand side of the figure 2.3 showing, that the CRE model is the appropriate model for this research.

In figure 2.3, opacity conditions are also shown for a typical laser plasma. In this thesis, the electron density is higher with n_e over 10^{21}cm^{-3}, and electron temperature are below 1 keV and above 100 eV. Thus, plasmas discussed in this thesis can be assumed to be optically thin by figure 2.3.

However, it has been shown that tin plasmas generated by Nd:YAG lasers are optically thick to the UTA radiation, hence plasma opacity must be considered. To simulate optically thick plasmas, which absorb emission rapidly, a CRE model which includes an additional factor, called the Escape factor, has been proposed. In this thesis, however, the basic CRE model was shown to be sufficient to understand the ion fractions in the plasma.

In a simple form of the collisional radiative model, the rate equation for the number density n_{Z+1} of the ions in the charge state $Z + 1$ reads,

$$\begin{aligned}\frac{dn_{Z+1}}{dt} = n_\text{e}[n_Z S(Z, T_\text{e}) - n_{Z+1} S(Z+1, T_\text{e}) \\ - n_{Z+1}\alpha_\text{R}(Z+1, T_\text{e}) + n_{Z+2}\alpha_\text{R}(Z+2, T_\text{e})],\end{aligned} \quad (2.76)$$

where, $S(Z, T_\text{e})$ is the collisional ionisation coefficient, $\alpha_\text{R}(Z, T_\text{e})$ is recombination rate consists of the radiative-recombination rate $\alpha_\text{r}(Z, T_\text{e})$, and the three-body recombination rate $\alpha_\text{3b}(Z, T_\text{e})$:

$$\alpha_\text{R}(Z, T_\text{e}) = \alpha_\text{r}(Z, T_\text{e}) + n_\text{e}\alpha_\text{3b}(Z, T_\text{e}). \quad (2.77)$$

These quantities are given by,

$$S(Z,T_\mathrm{e}) = 9\times10^{-6}\frac{\xi_Z (T_\mathrm{e}/\chi_Z)^{1/2}}{\chi_Z^{3/2}(4.88+T_\mathrm{e}/\chi_Z)}\exp\left(-\frac{\chi_Z}{T_\mathrm{e}}\right)\,[\mathrm{cm}^{-3}\mathrm{s}^{-1}] \tag{2.78}$$

$$\alpha_\mathrm{r}(Z,T_\mathrm{e}) = 5.2\times10^{-14}\sqrt{\frac{\chi_Z}{T_\mathrm{e}}}Z \times\left[0.429+\frac{1}{2}\log\left(\frac{\chi_Z}{T_\mathrm{e}}\right)+0.469\sqrt{\frac{T_\mathrm{e}}{\chi_Z}}\right][\mathrm{cm}^3\mathrm{s}^{-1}] \tag{2.79}$$

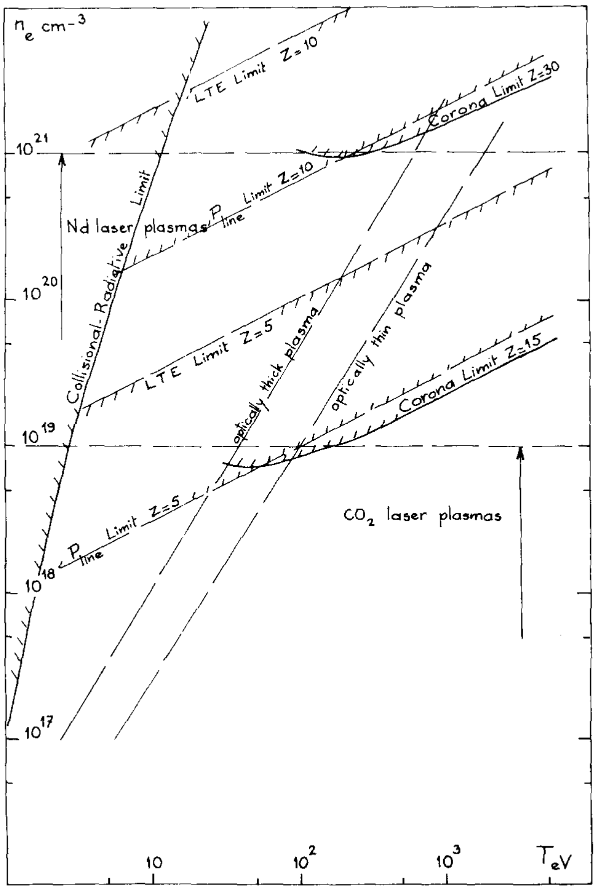

Figure 2.3 Criteria for applicability of different ionisation models for laser-produced plasmas [25].

$$\alpha_{3\mathrm{b}}(Z, T_\mathrm{e}) = \frac{2.97 \times 10^{-27}\xi_z}{T_\mathrm{e}\chi_z^2\left(4.88 + \frac{T_\mathrm{e}}{\chi_z}\right)} \,[\mathrm{cm}^6\mathrm{s}^{-1}] \tag{2.80}$$

where, ξ is the number of electrons in the outmost subshell corresponding to the state of charge Z and χ is the ionisation potential.

This is rather complicated, however, Colombant and Tonon have shown that this equation leads to the following relationship between two successive stages in the plasma in the stationary state:

$$\frac{n_{Z+1}}{n_Z} = \frac{S(Z, T_\mathrm{e})}{\alpha_\mathrm{r}(Z+1, T_\mathrm{e}) + n_\mathrm{e}\alpha_{3\mathrm{b}}(Z+1, T_\mathrm{e})} \tag{2.81}$$

This allows the computation of the ion fraction $n(Z)/n_\mathrm{T}$ of charge Z, where n_T is the number density of the total ionic population in the plasma.

The ion fraction as a function of electron temperature of gadolinium ions in a Nd:YAG plasma was calculated by using CRE model. In the calculation, calculated ionisation potentials from the Cowan code were used. Figure 2.4 shows ionisation potential as function of ion stage. The calculated ion fraction of gadolinium is shown in figure 2.5 along with the average charge state, as a function of temperature. The electron density was set to the critical density of Nd:YAG laser, i.e. $10^{21}\mathrm{cm}^{-3}$.

Colombant and Tonon also showed the following approximation for the electron temperature and average charge state,

$$T_\mathrm{e}[\mathrm{eV}] \approx 5.2 \times 10^{-6} A^{1/5}(\lambda^2\phi\,[\mathrm{W/cm}^2])^{3/5} \tag{2.82}$$

$$Z \approx \frac{2}{3}(AT_\mathrm{e})^{1/3} \tag{2.83}$$

where A is the atomic weight of the element under consideration, λ and ϕ are the wavelength and power density of incident laser pulse in μm and W/cm^2, respectively [25]. The calculated average charge state by using equation 2.83 is also shown in figure 2.5. In this approximation, the relationship between the three-body recombination term and radiative recombination assumed that $n_\mathrm{e}\alpha_{3\mathrm{b}} \ll \alpha_\mathrm{r}$. Thus, large differences between the two calculated results for average charge state are found at the lower end of the electron temperature range.

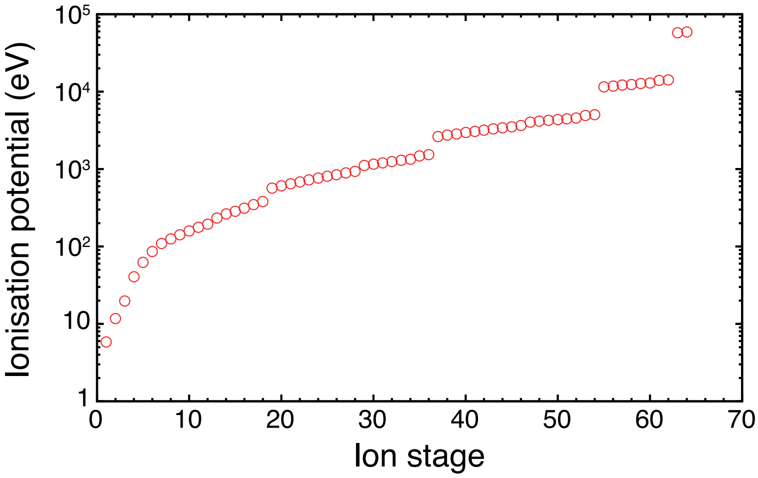

Figure 2.4 Ionisation potential of Gd as a function of ion stage calculated using the Cowan code.

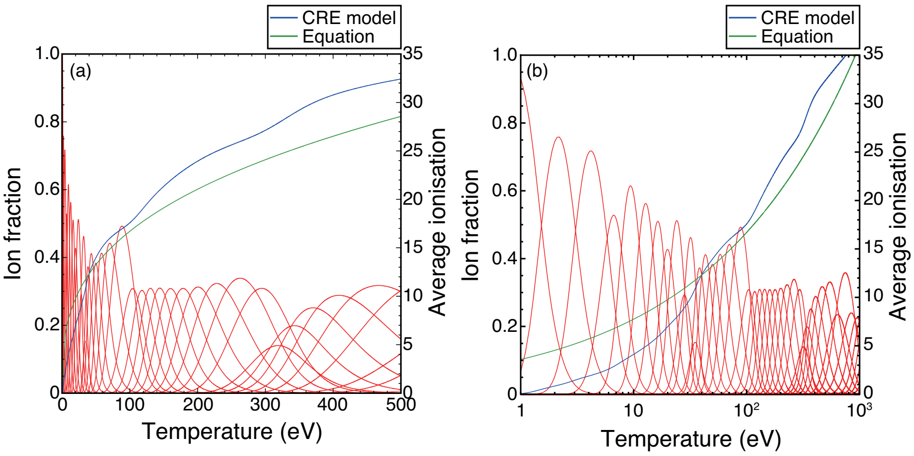

Figure 2.5 Ion Fraction of each charge state and average charge state of Gd as a function of electron temperature, (a) Linear X-scale, (b) Log X-scale. The calculation was done at electron density $1.0 \times 10^{21}\mathrm{cm}^{-3}$.

Reference

[1] C. McGuiness, “The XUV Photoabsorption and Photoionisation Spectra of Selected Ions: Techniques, Results and Theory”, (PhD. thesis, School of Physics, University College Dublin, 1996).

[2] L. Gaynor, “Inner shell $4d$ photo absorption spectroscopy of gas phase tellurium and cerium”, (PhD. thesis, School of Physics, University College Dublin, 2006).

[3] P. Hayden, “Extreme Ultraviolet Source Development Using Laser Plasmas Containing Tin”, (PhD. thesis, School of Physics, University College Dublin, 2007).

[4] C. O’Gorman, “Development of Extreme Ultraviolet Sources for Lithography at and below 13.5 nm”, (PhD. thesis, School of Physics, University College Dublin, 2006).

[5] F. F. Chen, “PLASMA PHYSICS AND CONTROLLED FUSION Volume 1: Plasma Physics”, (KLUWER ACADEMIC / PLENUM PUBLISHERS, 1984).

[6] D. Attwood, “SOFT X-RAYS AND EXTREME ULTRAVIOLET RADIATION Principles and Applications”, (CAMBRIDGE UNIVERSITY PRESS, 1999).

[7] W. L. Kruer, “THE PHYSICS OF LASER PLASMA INTERACTIONS”, (Westview Press, 2003).

[8] I. C. E. Turcu and J. B. Dance, “X-RAYS FROM LASER PLASMA: Generation and Applications”, (JOHN WILEY & SONS, 1998).

[9] J. Dawson and C. Oberman, “High-Frequency Conductivity and the Emission and Absorption Coefficients of a Fully Ionized Plasma”, Phys. Fluids. **7**, 981 (1964).

[10] T. W. Johnston and J. M. Dawson, “Correct Values for High Frequency Power Absorption by Inverse Bremsstrahlung in Plasmas”, Phys. Fluids. **16**, 722 (1973).

[11] Ya. B. Zel’dovich and Yu. P. Raizer, “Physics of Shock Waves And High-Temperature Hydrodynamic Phenomena”, (ACADEMIC PRESS New York and London, 1966).

[12] B. H. Bransden and C. J. Joachain, “Physics of atoms and molecules”, (Longman Scientific & Technical, 1983).

[13] J. P. Connerade, J. M. Esteva and R. C. Karnatak, “Giant Resonances in Atomes, Molecules and Solids”, (Plenum Press New York and London, 1987).

[14] G. O’Sullivan and P. K. Carroll, “$4d$ - $4f$ emission resonances in laser-produced plasmas”, J. Opt. Soc. Am. **71**, 227 (1981).

[15] C. Bauche-Arnoult, J. Bauche, and M. Klapisch, “Asymmetry of l^{N+1}-$l^{N}l'$ transition-array patterns in ionic spectra”, Phys. Rev. **30**, 3026 (1984).

[16] J. Bauche and C. Bauche-Arnoult, “Unresolved Transition Arrays”, Phys. Scr. **37**, 659 (1988).

[17] C. Bauche-Arnoult, J. Bauche, “Statistical Approach to the Spectra of Plasmas”, Phys. Rev. **T40**, 58 (1992).

[18] R. D. Cowan, “THE THEORY OF ATOMIC STRUCTURE AND SPECTRA”, (UNIVERSITY OF CALIFORNIA PRESS, 1981).

[19] P. L. Altick and A. E. Glassgold, “Correlation Effects in Atomic Structure Using the Random-Phase Approximation”, Phys. Rev. **133**, A632 (1964).

[20] W. Kohn and L. J. Sham, “Self-Consistent Equations Including Exchange and Correlation Effects”, Phys. Rev. **140**, A1133 (1965).

[21] A. Zangwill and D. A. Liberman, “A NONRELATIVISTIC PROGRAM FOR OPTICAL RESPONSE IN ATOMS USING A TIME- DEPENDENT LOCAL DENSITY APPROXIMATION”, Comput. Phys. Commun. **32**, 63 (1984).

[22] D. A. Liberman and A. Zangwill, “A RELATIVISTIC PROGRAM FOR OPTICAL RESPONSE IN ATOMS USING A TIME-DEPENDENT LOCAL DENSITY APPROXIMATION”, Comput. Phys. Commun. **32**, 75 (1984).

[23] M. Lysaght, D. Kilbane, N. Murphy, A. Cummings, P. Dunne, and G. O'Sullivan, "Opacity of neutral and low ion stages of Sn at the wavelength 13.5 nm used in extreme-ultraviolet lithography", Phys. Rev. A, **72**, 014502 (2005).

[24] L. Gaynor, N. Murphy, P. Dunne and G. O'Sullivan, "Extreme ultraviolet photoabsorption spectra of the Ce VI-Ce X isonuclear sequence", J. Phys. B: At. Mol. Opt. Phys. **41**, 245002 (2008).

[25] D. Colombant and G. F. Tonon, "X-ray emisiion in laser-produced plasmas", J. Appl. Phys. **44**, 3524 (1973).

Chapter 3

Experimental Apparatus

While in chapter 1 only two applications were introduced, there are a large variety of applications for extreme ultraviolet and soft X-ray sources. Therefore the source development in this spectral region is a very interesting topic for fundamental and applied research. As can been seen from research into tin-based plasma sources, the development of EUV and SXR sources is not easy and needs much investigation under different conditions. In this thesis, gadolinium and bismuth plasma sources are characterised under different experimental conditions. In this chapter experimental apparatus common to all of the studies are described, but further details about the experimental setups are described in each chapter.

3.1 The Lasers

Four different neodymium-doped yttrium aluminum garnet (Nd:YAG) lasers were employed for creating the plasmas studied in this thesis. The Nd:YAG laser is a solid-state laser which uses a YAG ($Y_3Al_5O_{15}$) rod crystal doped with the rare earth metal ion Nd^{3+}, as the lasing medium. The Nd^{3+} doped YAG rod offers a group of laser lines in the near-infrared (NIR) spectral region. Figure 3.1 shows the four-level Nd:YAG system yielding emission at 1064 nm. A krypton (Kr) or xenon (Xe) flash lamp pumps the electrons in the Nd ion to an excited state. From this excited state the electron decays to the ground state through a metastable state as shown in figure 3.1. In this process, decay between the upper level ($^4F_{3/2}$) and the lower level ($^4I_{11/2}$) produces radiation at a wavelength of 1064 nm [1].

In this section, the specifications of each laser, such as the maximum output and pulse width, are shown.

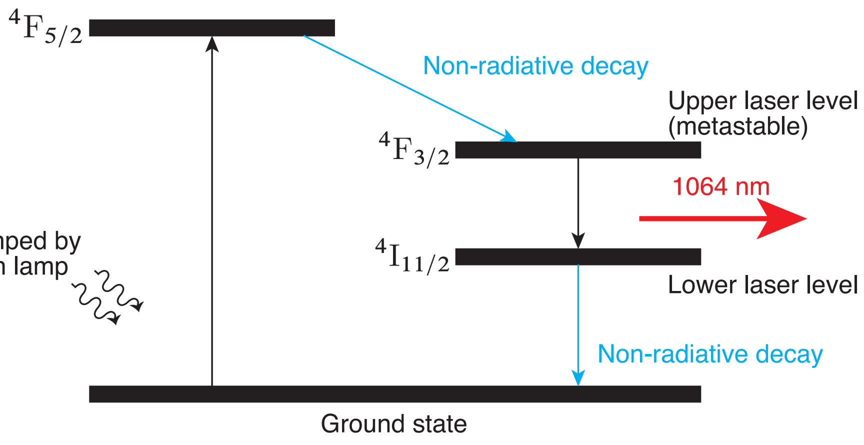

Figure 3.1 Four level laser system diagram of Nd:YAG laser

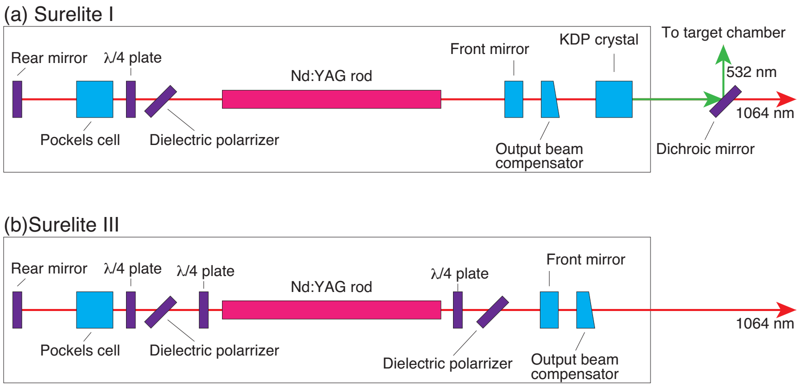

Figure 3.2 Optical layout of Surelite I and optional separation.

3.1.1 Surelite I and Surelite III

Two different Nd:YAG lasers made by Continum were used in this research. Figure 3.2 shows optical layout of the Surelite I and optional harmonic separation, and Surelite III. The Oscillator of the Surelite series consists of a Nd^{3+} doped YAG rod, a flash lamp, a thin film multilayer dielectric polarizer, Pockel's cell and $\lambda/4$ wave plate. This is a very typical solid-state Q-switched laser system. The linear flash lamp is employed as an excitation source to pump the Nd:YAG rod which is 115 mm in length when measured along the optic axis, with hard dielectric anti-reflective (AR) coating on each end. The Pockels cell is made from a longitudinal KDP crystal with a 15 mm clear aperture. The polarizer allows horizontally polarized light to transmit ($> 95\%$), but reflects vertically polarized

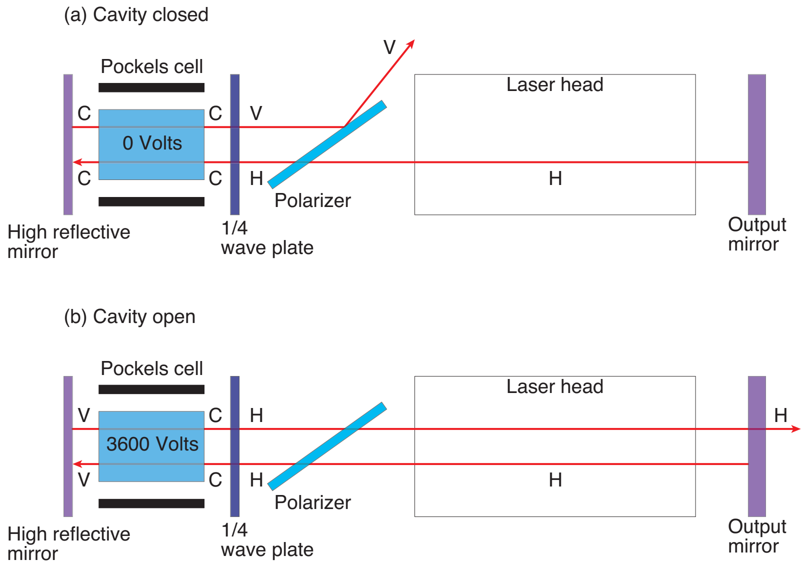

Figure 3.3 Schematic diagram of the Surelite cavity. (a) Cavity close, (b) Cavity open. H refers to horizontally polarised light, V and C refer to vertically polarised light and circularly polarised light, respectively.

light (> 99%).

Figure 3.3(a) shows a schematic of the cavity in closed configuration. When zero volts applied to the Pockel's cell, it applies no phase retardation to the light while the wave plate applies $\pi/2$ retardation to the light with each pass, applying a total rotation of 90 degrees. Thus the light becomes vertically polarised and is reflected by the polariser leading to no oscillation. In other words, this Q-switch blocks lasing in the resonator until the laser gain can reach its optimum.

Figure 3.3(b) shows a schematic of the cavity in open configuration. When 3.6 kV volts is applied on the Pockel's cell the Pockel's cell and the wave plate each apply a $\pi/2$ retardation individually to the light with each pass, applying a total rotation 180 degrees. Thus horizontally polarised light is essentially rotated 4 times, and finally back to horizontally polarised light again, resulting in the transmission through the polariser leading to oscillation. In other words, it opens the cavity, resulting in the emergence of high peak power laser pulse.

The fundamental wavelength of the Surelite I was frequency doubled by using a KDP crystal inside the laser system, and the output is separated into 1064-nm and 532-nm beams using a dichroic mirror at the outside of the laser system. The Surelite I was mainly used for producing a pre-plasma in the dual-pulse irradiation experiment which is described in chapter V. The laser pulse at the fundamental wavelength emitted by the Surelite III was mainly used for producing the absorb-

Table 3.1 Specification of Surelite series.

Model	Surelite I	Surelite III
Wavelength	532 nm	1064 nm
Maximum output laser pulse energy	200 mJ	400 mJ
Pulse width (FWHM)	5-7 ns	7 ns
Repetition rate	10 Hz	10 Hz

ing plasma in the photoabsorption spectroscopy experiment described in chapter VI. The maximum laser energy and other parameters of each laser are shown in table 3.1.1. Further details on the operation the laser are available in the manual [2].

3.1.2 EKSPLA SL312 and SL312P

Two different Nd:YAG lasers made by EKSPLA were used in this research. Figure 3.4(a) and 3.4(b) show the optical layout of the SL312 and SL312P, respectively. As can be seen from figure 3.4, both lasers consist of four blocks of system components.

The first stage is the master oscillator cavity. The xenon flash lamp discharge starts synchronously with the application of a high voltage to the electro optic Pockels cell crystal. This induces the population inversion in the Nd:YAG rod to reach the optimum. The gain due to population invention is allowed to reach a high value without laser oscillations occurring, as a high loss cavity is formed by the Pockels cell. This high loss prevents lasing while the active medium is being excited by the flash lamp. Once the maximum population inversion is achieved which the Q-switch cannot completely hold, light starts to escape from the cavity (free running) and lasing begins. A negative feed back system, consisting of a polariser and a PIN photodetector, measures reflected light from the polariser, and depending on the intensity of this light applies a voltage to the Pockel's cell which changes the polarisation of light in the Pockel's cell. As a result the master oscillator keeps lasing at a low level for a prolonged period of time, during which a single longitudinal mode is established due to the selective properties of the Fabry-Perot etalon which is in the laser cavity. A YAG:Cr crystal also improves single longitudinal mode selection. This single mode is established typically within 15-20 μs after light starts to escape from the oscillator cavity. At this point the high voltage applied to the Pockels cell is grounded, forming a low loss cavity, resulting in the emergence of a single mode Q-switched pulse containing all the available energy. This quicky depopulates the upper lasing level to such an extent that the lasing stops. The master oscillator output pulse is typically ~ 2 ns in duration with an energy of 4-5 mJ.

The second system is a stimulated Brillouin scattering (SBS) pulse compressor. Pulse compressor consists of two lenses (L1 and L2, The SL312 contains only L1), quarter wave retardation plate (QWP1), SBS (stimulated Brillouin scattering) cell with CCL_4 liquid, and polariser (P1).

A linearly polarised seed pulse from the master oscillator passes through the quarter wave plate (QWP1) changing into circular polarisation and is focused into the double-pass SBS-cell by lenses (L1 and L2). The seed pulse is compressed *via* a backward SBS process. The backscattered Stokes pulse, as its phase is reversed, repeats the same path of seed pulse in the opposite direction and with a reversed divergence. The compressed pulse passes the retardation plate (QWP1) again that transforms the polarisation of the compressed pulse into linear polarised light, perpendicular to the original polarisation of the master oscillator radiation. Polariser (P1) reflects the compressed pulse having vertical polarisation and mirrors (M3 and M4) guide the compressed pulse into the amplification stage.

(a) SL312

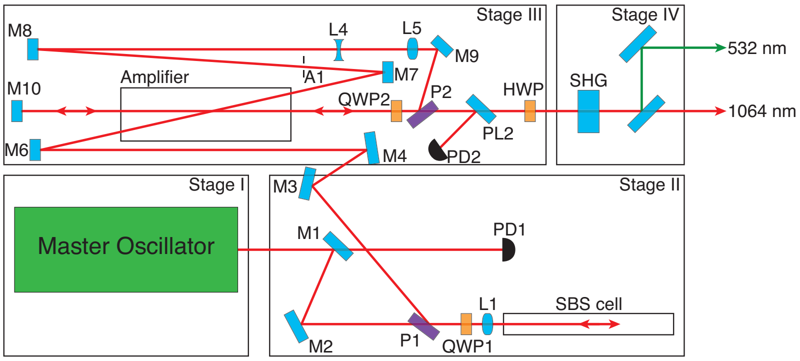

(b) SL312P

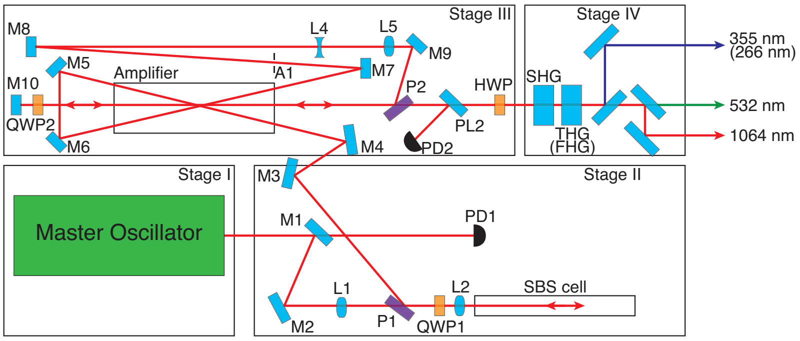

Figure 3.4 SL312

Table 3.2 Specifications of the SL series laser system.

Model	SL312	SL 312P
Wavelength	1064 nm	1064 nm
Maximum output laser pulse energy	250 mJ	500 mJ
Pulse width (FWHM)	150 ps	170 ps
Repetition rate	10 Hz	5 Hz

The third stage is a multi-pass optical pulse amplification system. The multi-pass optical pulse amplifier contains a Nd:YAG rod pumped by a flash lamp and includes optical components to arrange multiple passes. Mirrors M4-M7 arrange the first pass through the Nd:YAG rod. Then a telescope formed by two lenses (L4 and L5) expands the beam. Mirror (M9), polariser (P2) and mirror (M10) ensure that the next two passes traverse the rod. The pulse passes two times through the quarter wave retardation plate (QWP2) changing polarization by 90 degrees and leaves the multi pass optical pulse amplification system passing through the polarizer (P2). The aperture (A1) serves to ensure that depolarized radiation is not returned to the amplification system. The major difference between the SL312 and Sl312P is the number of amplifying times in the amplification system. The pulse goes through the amplifier rod only 3 times in the SL 312, compared to 4 times in the SL312P.

The fourth functional block is the harmonic generators. The Nd:YAG laser fundamental wavelength can be frequency doubled, tripled and quadrupled by interjecting nonlinear crystals, which generate the corresponding harmonics (second harmonics:SHG, third harmonics:THG, fourth harmonics: FHG). However, only the fundamental wavelength was used in this research. The specifications of each laser systems are shown in table 3.2. Further details on the operation the lasers are available in the manuals [3, 4].

3.2 Spectrometer

Two different flat field grazing incidence spectrometers were employed in this research. Figure 3.5 shows schematic diagrams of the spectrometers. Figure 3.5(a) shows a spectrometer made by Shinkukougaku Co.Ltd., and (b) and (c) show side and top views of the spectrometer which was designed and built in University College Dublin. In this thesis, this homemade spectrometer will be called the UCD spectrometer. The basic components are almost same in each.

Light from the source enters the vacuum chamber *via* an entrance slit. The

(a) Shinkukougaku XUV-235-II (Top view)

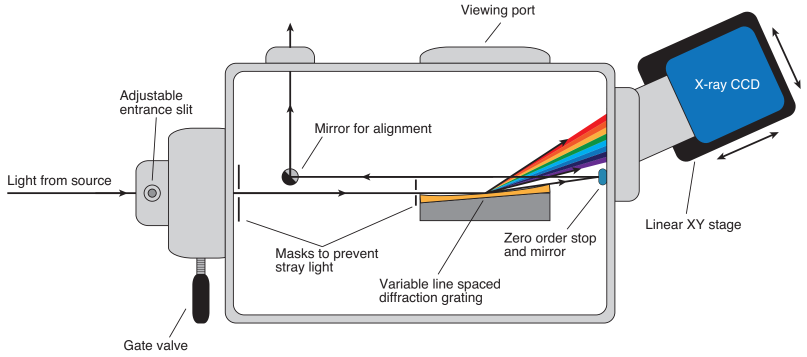

(b) Double grating flat field grazing incidence spectrometer (Side view)

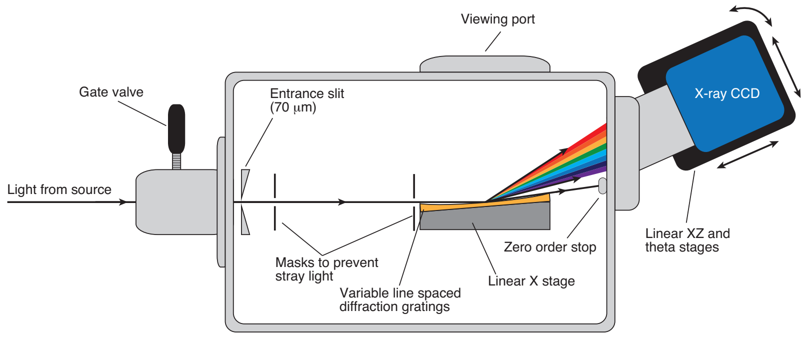

(c) Double grating flat field grazing incidence spectrometer (Top view)

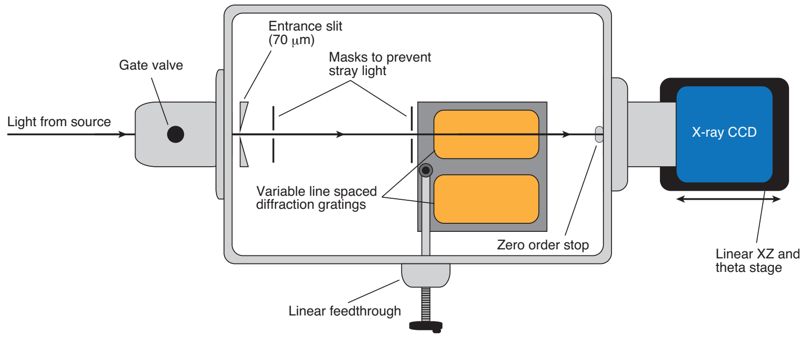

Figure 3.5 Schematic diagram of the spectrometers. (a) Shinkukougaku XUV-235-II, (b) Side view of double grating flat field grazing incidence spectrometer. (c) Top view of double grating flat field grazing incidence spectrometer.

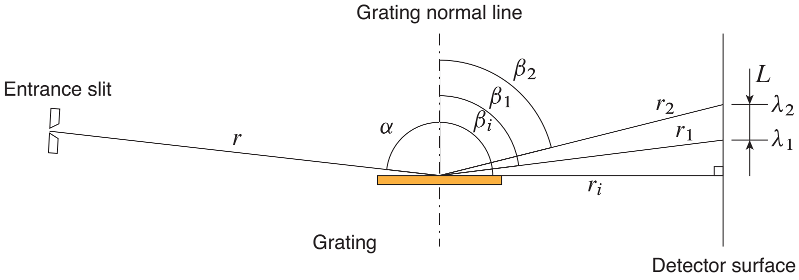

Figure 3.6 Schematic of grating.

UCD spectrometer has a fixed slit (70 µm), while the XUV-235-II has a variable entrance slit. The variable slit was set at 100 µm in this research. In each spectrometer the light is dispersed by a flat field grating which is mounted in the chamber. The dispersed light reaches a charge coupled device (CCD) camera, forming a time-integrated image of the spectrum on the CCD. There is a zero order stop fitted to prevent zero order diffracted light travelling between the grating and CCD. The zero order stop in the XUV-235-II consists of a metal mirror which allows to align the spectrometer on the optical axis. There are some masks mounted in appropriate places in the chamber to prevent stray and scattered light.

These spectrometers house variable line spacing gratings which are flat field gratings [5–7]. They provide a vertical plane image unlike the curved plane provided by equal spacing gratings in the Rowland circle mounting. All flat field gratings used in this research are made by SHIMADZU. The XUV-235-II houses only one grating (2400 grooves/mm), while the UCD spectrometer houses two gratings (1200 grooves/mm and 2400 grooves/mm). These two gratings are mounted on a linear stage that allows them to be changed by the a linear feedthrough without opening the vacuum chamber. Thus, the UCD spectrometer allows one to observe different spectral ranges almost at the same time. Figure 3.6 shows schematics of the grating. The mounting parameters are shown in table 3.3

The CCDs used in this research are made by Andor. DO420-BN and DX436-BN models were attached to the XUV-235-II and the UCD spectrometer, respectively. The active pixels, pixel size and image area are shown in 3.3.

Table 3.3 also shows other detail of the spectrometers. The resolving power which is $\lambda/\Delta\lambda$ was calculated using observations of the emission line of nitrogen (N VI: $1s^2 - 1s2p$). Figure 3.2 shows observed emission spectra from reaction-bonded silicon nitride plasmas recorded on each spectrometer. Further details of the spectrometers, gratings and CCDs are available on the website [8–10].

Table 3.3 Specification of spectrometers.

	XUV-235-II	UCD spectrometer	
Grating (Model)	30-001	30-002	30-003
Grating [grooves/mm]	2400	1200	2400
Wavelength range [nm]	1-6	5-20	1-7
Distance (r) [mm]	237.0	237.0	236.7
Incident angle (α) [degree]	88.65	87.0	88.6
Distance (r_i) [mm]	235.0	235.0	235.0
Angle (β_i) [degree]	90.0	90.0	90.5
Distance (r_1) [mm]	235.6	236.7	235.8
Angle (β_1) [degree]	85.81	83.0	85.8
Distance (r_2) [mm]	238.5	241.1	239.5
Angle (β_2) [degree]	80.17	77.1	79.4
Resolving power ($\lambda/\Delta\lambda$)	502	195	503
CCD (Model)	DO420-BN	DX436-BN	
Active pixels	1024 × 255	2048 × 2048	
Pixel size [µm]	26 × 26	13.5 × 13.5	
Image area [mm]	26.6 × 6.7	27.6 × 27.6	

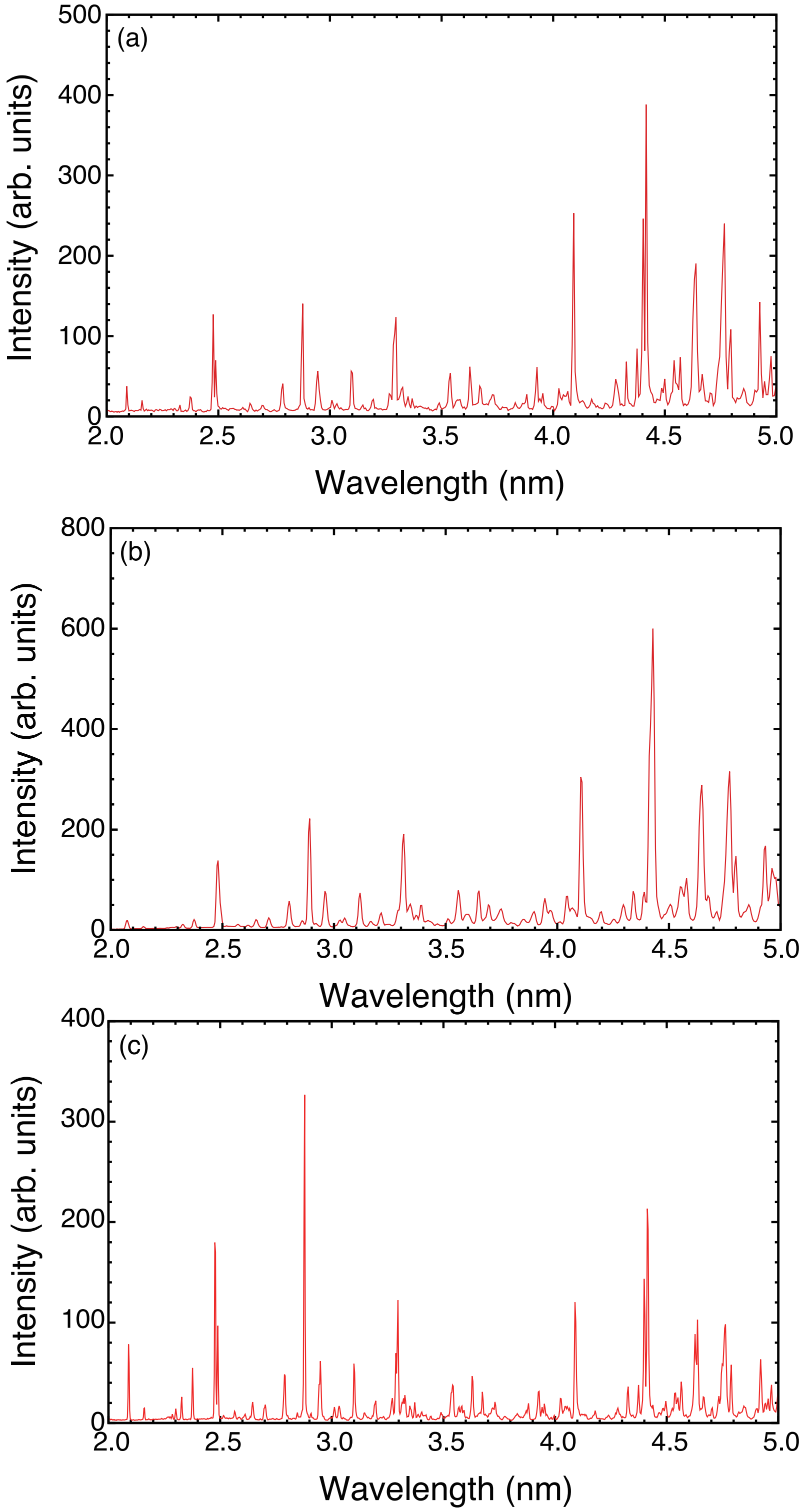

Figure 3.7 Emission spectra from silicon nitride plasmas recorded on the different spectrometers & gratings. (a) Sinkukougaku, (b) The UCD spectrometer (1200 grooves/mm), (c) The UCD spectrometer (2400 grooves/mm).

3.3 Summary

Each of the main pieces of experimental apparatus were described in this chapter. Four different Nd:YAG lasers and two different spectrometers were employed in this work. The EKSPLA 312P and Surelite III lasers were used to create the plasmas, and the UCD spectrometer was used to observe absorption in gadolinium and bismuth plasmas, the results of which are described in Chapters 4 and 7. The EKSPLA 312 and Surelite I were used to create highly ionised bismuth plasmas, and the XUV-235-II made by Shinkukougaku was used to observe emission spectra from highly ionised bismuth plasma, which are described in Chapter 5 and 6. Details of each experimental setup are described in each of the relevant chapters.

Reference

[1] J. E. Geusic, H. M. Marcos, and L. G. Van Uitert, “Laser oscillations in Nd-doped yttrium aluminum, yttrium gallium and gadolinium garnets”, Appl. Phys. Lett. **4**, 182 (1964).

[2] Continuum. “Operation and Maintenance Manual Surelite Laser”.

[3] Ekspla. “Laser SL312P: Technical Description and Users Manual”, 2003.

[4] Ekspla. “Laser SL312: Technical Description and Users Manual”, 2004.

[5] T. Harada and T. Kita, “Mechanically ruled aberration-corrected concave gratings”, Appl. Opt. **19**, 3987 (1980).

[6] T. Kita, T. Harada, and H. Kuroda “Mechanically ruled aberration-corrected concave gratings for a flat-field grazing-incidence spectrograph”, Appl. Opt. **22**, 512 (1983).

[7] N. Nakano, H. Kuroda, T. Kita and T. Harada, “Development of a flat-field grazing-incidence XUV spectrometer and its application in picosecond XUV spectroscopy”, Appl. Opt. **23**, 2386 (1984).

[8] Shinkukougaku Co.Ltd., “http://www.shinku-kogaku.co.jp/english/product/?id=1247820444-516012”.

[9] SHIMADZU, “http://www.shimadzu.com/products/opt/dif/oh80jt0000001nqa.html”.

[10] ANDOR, “http://www.andor.com/pdfs/specifications/Andor_Classic_SX_DW_Specifications.pdf”.

Chapter 4

Observation of the absorption spectra of gadolinium ions

As described in chapter 1, an EUV source at a wavelength of 6.x nm is considered as a potential lithography source for next generation lithography beyoned EUV. The emission spectra, conversion efficiency and numerical simulation of gadolinium and terbium laser produced plasmas, which are capable of emitting radiation in that spectral range, have been already investigated [1–12]. Emission from gadolinium and terbium plasmas is also attributed to $4d - 4f$ and $4p - 4d$ transitions in a number of ion stages, resulting in overlapping unresolved transition arrays. The peaks of the UTA of gadolinium and terbium are at 6.7 nm and 6.5 nm, respectively [1, 6].

In previous work, the effect of the viewing angle on emission spectra of gadolinium has been studied [8]. Figure 4.1 shows the effect of viewing angle on the emission spectra for 10 ns and 150 ps laser pulse durations. In both sets of spectra, emission from Ag- and Pd-like Gd^{17+} and Gd^{18+} near 6.7 and 7.1 nm were observed. However, the spectrum produced by the 10 ns laser pulse is optically thick. As a result, it was found that spectra viewed at 45° (solid lines) and 90° (dashed lines) were significantly different, and it was summarised that this is due to absorption by low gadolinium ion stages and to anisotropic ion distributions in laser-produced plasmas [8].

The photoabsorption profile of neutral to 3 times ionised gadolinium plasma has already been shown to consist of giant resonances using charge-separated photoion-yield spectroscopy with the photons provided by monochromatized synchrotron radiation [13–15]. However, there is no observation of photoabsorption spectra using laser-produced plasmas to date.

In this chapter, the physical mechanism of $4d \to \varepsilon f$ shape giant resonances is described in order to understand the absorption spectra of gadolinium. After that, photoabsorption spectra of gadolinium ions recorded by using the dual laser

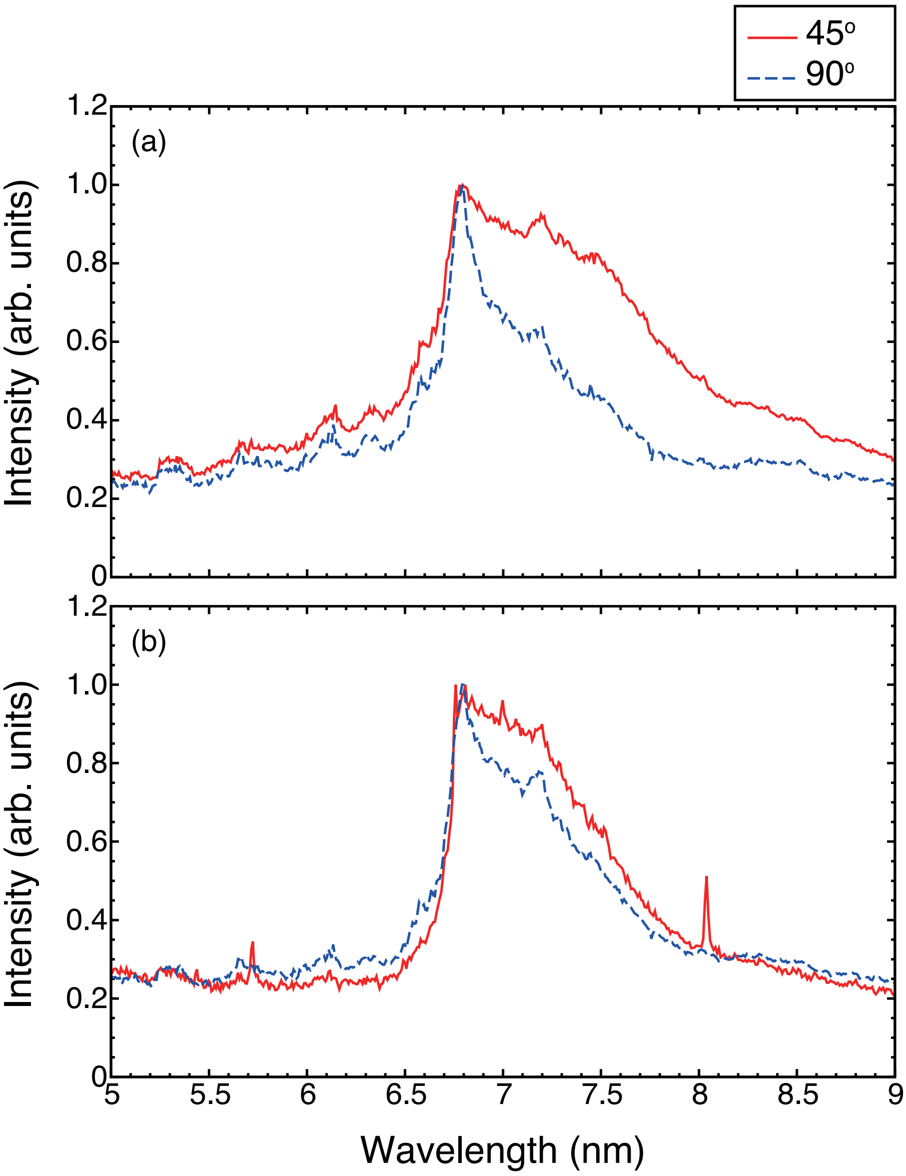

Figure 4.1 Emission spectra from the (a) 10 ns and the (b) 150 ps LPPs for the four different viewing angles. Solid and dashed lines correspond to the spectrum viewed at 45 and 90 degrees, respectively.

plasma (DLP) technique are shown. Numerical calculation results using time dependent local density approximation (TDLDA) calculation are also described to discuss the experimental results.

4.1 $4d \rightarrow \varepsilon f$ shape resonances

One interesting feature of the rare-earth atoms, such as gadolinium, is due to the character of the partly filed $4f$ shell. Because the $4f$ wavefunction behaviour in such atoms is complicated, strong overlap of the εf and $4d$ orbitals has made the $4d \rightarrow \varepsilon f$ shape resonance which is known as a giant resonance. The physics is well summarised in the book "Giant Resonances in Atoms, Molecules, and Solids" [13]. In this section, a brief explanation is described to provide some understanding of the giant resonance.

First of all, we should describe the autoionisation process. Autoionisation is a non-radiative two-step process, which leads to an increase in charge of the atom/ion involved. It involves the excitation of an atom/ion into a state above its ionisation limit followed by de-excitation to an ion of lower energy and the ejection of an electron whose energy is equal to the difference between the energy of the excited atom and that of the final ionic state. Note that the initial excitation of the atom/ion may be due to a photoabsorption process. Figure 4.2 shows an example of the autoionisation process in potassium for the case of autoionisation from an excited configuration of a neutral atom to a singly ionised ion. Inner shell excitations decay primarily by autoionisation because the energy required to excite an inner shell electron is usually greater than the ionisation potential of the ion in question. For neutral atoms in general, excitation from an inner shell will lead to a discrete state which lies well above the ionisation limit of the atom and

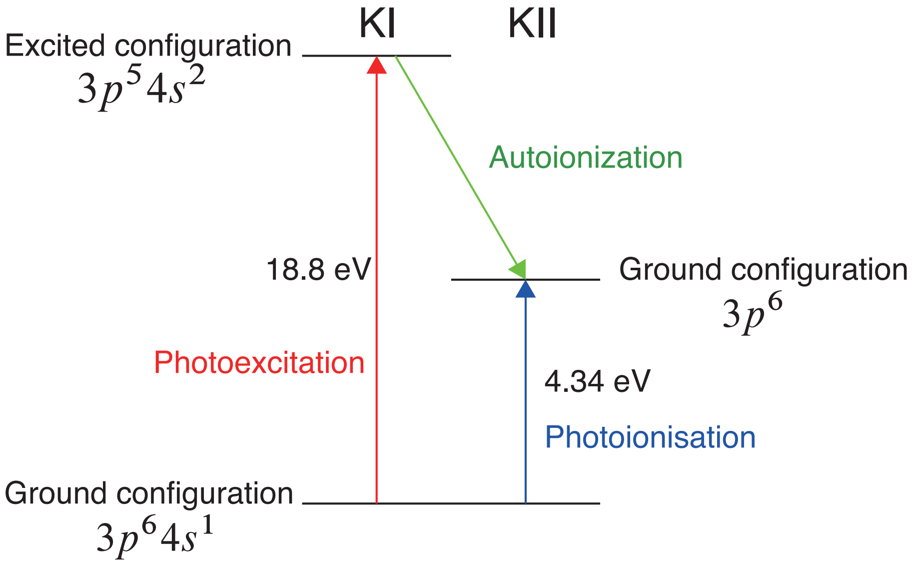

Figure 4.2 Auto ionisation process for potassium.

the width of an absorption line from an inner subshell will be broadened by the process of autoionisation. In most cases radiationless transitions vastly dominate over photon emission. However excited states lying below the first ionisation limit decay radiatively. This is the case for valence shell excitations. In both cases, the linewidth of the transition is inversely proportional to the lifetime of the discrete state [17].

Photoabsorption into excited bound states of an atom produces a series of lines whose energies converge to the threshold for photoionisation. Beyond this limit there exists a continuous absorption spectrum, resulting from photoionisation of one electron into a state εl; this electron is ejected from the atom with kinetic energy ε. The properties of the absorption continuum are a direct extension of the properties of the series of absorption lines.

Above the $4d$ threshold of Cs and the elements immediately preceding it in the periodic table, the photoabsorption spectrum is dominated by a broad $4d \rightarrow \varepsilon f$ shape resonance. This resonance rises slowly past the photoionisation threshold to peak some 20-30 eV above it, known as a delayed onset. Below this threshold, discrete features arising from $4d \rightarrow np$ excitations are present, whereas features arising from $4d \rightarrow nf$ excitations are absent. Transitions of the type $4d \rightarrow nf$ are absent because of the large centrifugal repulsion present in the $l = 3$ channel, which excludes the nf wavefunctions from the core region. In these elements the radial potential has a double-well character and the nf wavefunctions are essentially eigenstates of the outer well.

The explanation for the observed delayed onset of the continuum is that an electron excited above the $4d$ threshold into the εf channel will have to tunnel through the centrifugal barrier before it can escape from the atom. Hence the $4d$ photoionisation cross section rises slowly with increasing energy until the outgoing photoelectron almost completely surmounts the barrier. The photoionisation process thereafter behaves like that of normal atoms and decreases almost monotonically since additional nodes of the εf function overlap with the $4d$ function with any further increase in photon energy.

Beyond barium the inner well of the radial potential is sufficiently deep to allow a single quasi-bound level to be supported. The (autoionising) decay of this inner well state gives rise once more to a giant resonance qualitatively similar to those encountered in the lighter elements [13, 17].

4.2 The dual laser plasma technique

The dual laser plasma (DLP) technique involves the generation of both an absorbing column and a synchronised bright backlighting continuum using separate laser produced plasmas. Elements with atomic numbers over 62 emit pure continuum in the extreme ultraviolet region over a large range of plasma conditions and, as such, can be used as the backlighting plasma in this technique.

To observe optimum photoabsorption spectra from low ion stages the absorbing column should be generated by laser pulse focused as a line, along the optical axis, and the backlighting plasma should be as bright as possible. Because an absorbing line plasma is optically thick at certain wavelength regions of the continuum radiation, high absorption of the continuum radiation in the line plasma can be induced. A brighter backlighting continuum plasma results in a higher contrast spectrum, making the absorption features more pronounced.

The dual laser plasma technique is a practical, unique and effective diagnostic tool for photoabsorption spectroscopy. It has been successfully used for the investigation of low and intermediate ion stages up to six times ionised. [18–32]. Ion stage distribution in the absorbing column is controllable and isolation of particular absorbing ions is achieved by varying the following parameters:

- Laser power density
- Time delay between generation of the plasmas
- Position of the absorbing plasma with respect to the optical axis

The ion fraction in a plasma is primarily determined by the laser power density. The lasers employed in this research were Nd:YAG lasers and were operated at wavelength of 1064 nm. Thus, only the power density ϕ was varied. This variation was achieved by either changing the output energy of the laser or by varying the focused spot size, as given by,

$$I_{\mathrm{Laser}} = \frac{E_{\mathrm{Laser}}}{\tau_{\mathrm{Pulse}} \times S_{\mathrm{Spot}}}. \tag{4.1}$$

where, E_{Laser} is the pulse energy, τ_{Laser} (FWHM) is the temporal pulse width and S is the area of incident laser pulse on target.

Controlling the injection time of the continuum radiation into the absorbing plasma will also allow absorption to be observed from different ion stages. At short time delays after formation the absorbing plasma, relatively high ion stages will dominate in absorber, determined by the power density of the incident beam (and hence the plasma electron temperature). At longer time delays, the plasma will be cooler and consequently will be dominated by lower ion stages, due to recombination of the highly charged species.

The region of the absorbing plasma injected will also affect the observed dominant ion stage. Generally, injecting at the centre of the absorber gives spectra of high ion stages, while injecting the cooler edges of the plasma gives absorption

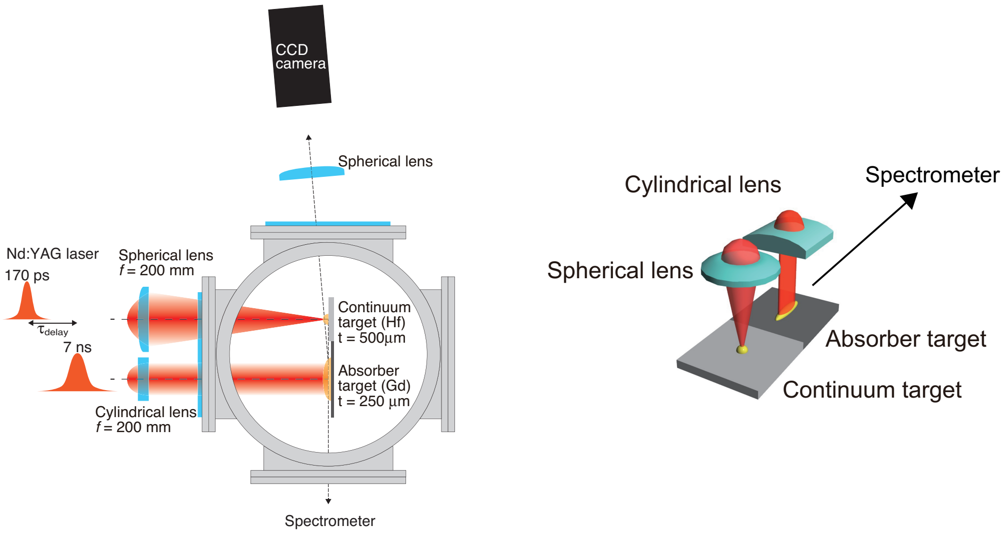

Figure 4.3 Schematic of the experimental setup for the dual laser plasma (DLP) technique.

from lower ion stages. As the plasma expands, ions move outwards and recombine, resulting in a cooler outer frame where lowly charged ions are the dominant species. Filevich *et al.*, have reported soft x-ray laser interferograms of laser produced plasmas generated using 1.06 µm 13 ns laser pulses at power densities in the range $1\times 10^{11} - 7\times 10^{12}\,\mathrm{W/cm^2}$ [33]. They revealed the formation of an inverted density profile with a density minimum on axis and a distinct plasma outer frame. Coupled with the predictions of the steady state collisional radiative model, which is described chapter 2, where the principle ion stage present in a plasma is determined by the plasma electron temperature, the large number of lowly charged ions in the outer regions of the plasma is easily explained.

4.3 Experimental setup

Figure 4.3 shows a schematic of the experimental setup. The Surelite III and EKSPLA SL312P lasers were employed. As described in chapter 3, these lasers supply 7-nanosecond and 150-picosecond laser pulses, respectively. The picosecond laser pulse was focused by a plano-convex lens ($f = 200$ mm) onto a planar hafnium target placed in the target chamber, generating the backlighting source. The absorber was generated by the nanosecond laser pulse, which was focused by a plano-convex cylindrical lens ($f = 200$ mm) onto a planar gadolinium target placed in the target chamber. Each target dimension was significantly

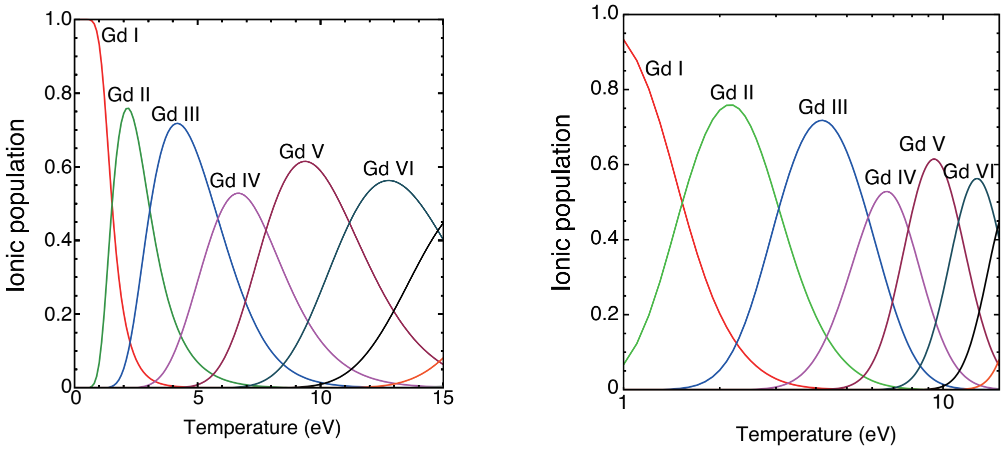

Figure 4.4 Ion fraction of each charge state as a function of electron temperature. (a) Linear X-scale, (b) Log X-scale. The calculation was performed for an electron density of $1.0 \times 10^{21}\text{cm}^{-3}$

larger than the beam diameter at the focal points. The targets were mounted on an automatic motion stage and controlled by an actuator from outside the chamber. The beam diameter on target was approximately 400 μm (full width at half maximum: FWHM) for the picosecond laser pulse, while the dimensions of the nanosecond pulse were 250 μ× 1 cm. The maximum laser power densities were 2.3×10^8 W/cm^2 for the nanosecond laser pulse and 1.6×10^{11} W/cm^2 for the picosecond laser pulse, respectively.

Emission spectra from the plasmas were observed by the UCD grazing incidence spectrometer, which was placed at 90 degrees with respect to the incident laser axis. Time-integrated spectra were measured by a thermoelectrically cooled back-illuminated X-ray charge coupled device (X-ray CCD) camera (Andor, DX436-BN). The lasers and the X-ray CCD camera were synchronised by delay generators (Stanford Research System, DG645 and DG535). The exposure time of the X-ray CCD camera was set at 1 second. The observed spectra were calibrated using nitrogen and silicon lines from a plasma formed on a silicon nitride target.

As described in chapter 2, the steady-state collisional-radiative ionisation model gives an ion fraction which depends on the electron temperature. Figure 4.4 shows the ion fraction as a function of electron temperature. Under the conditions of the laser power density employed to form the absorbing plasma, the maximum electron temperature was calculated as 1.4 eV. Thus, the continuum radiation should reveal absorption by Gd I to Gd II ions. Note that the laser power density was estimated using photographic burn paper to give the maximum spot sizes. Thus, this power density represents the minimum laser power density.

4.4 Result and discussion

Figure 4.5 shows the absorption spectra of gadolinium ions. Since the density of ions in the absorber has not been determined, only relative absorbances have been obtained.

As can be seen from figure 4.5, broad absorption spectra were observed at all delay times with peak absorption at a wavelength of 8.3 nm. From the CR-model, this absorption is expected to be attributed to Gd I and Gd II ions. This is the $4d \rightarrow \varepsilon f$ giant resonance of Gd which comes from strong coupling between the $4d^{10}4f^7 \rightarrow 4d^94f^8$ and the $4d^{10}4f^6\varepsilon l$ continuum. The spectra observed at the delay times of 50-200 ns were broader than those observed at the delay times of 300-800 ns. The character of the Gd giant resonance at delay times between 300 and 500 ns was similar to that previously reported [13–15]. As described already, the resonance shape strongly depends on the $4f$ wavefunction, it can be assumed that spectral behaviour is dominated $4f$ wave function contraction effects. In previous work ion yield measurement show that photoionisation in the giant resonance is mainly due to singly or doubly charged Gd ions [13–15].

In order to evaluate the photoabsorption cross section, RTDLDA calculation were employed [34, 35]. Figure 4.5 shows comparison of the theoretical cross section and the observed spectrum at a delay time of 500 ns. The experimental spectrum agrees well with the theoretical cross section Gd I. The theoretical cross section has been shifted and normalised, resulting in a theoretical cross section very close to the experimental spectrum. The maximum value of the cross section is 65.9 Mb at 8.3 nm. In the photoabsorption spectrum shown in figure 4.5(b) at the delay time of 75 ns, small humps were observed in the broad structure at 7.7 nm. However, the theoretical cross section for higher ion stages occurring at shorter delay times has yet to be calculated. The plasma at the shorter delay times can be assumed to contain doubly or triply charged Gd ions. G. Kutluk *et al* showed photoabsorption spectra of Gd I, Gd II and Gd III, however, the features were not broad and the small structure at 7.8 nm was not shown [15].

To prove our previous report, comparison between emission spectra from a Gd LPP and the absorption spectra are shown in figure 4.7. The spectra were normalised by peak values. From comparison of spectra observed at 45 and 90 degrees, it can be found that broad absorption from 6.8 - 8.0 nm is presented in the emission spectra, however, the cross section was maximised at 8.3 nm in the photoabsorption spectra. For an expanding hot dense plasma, the highest ion stages are generally found close to the centre of the plume, while lower stages dominate close to the edge. Therefore singly or doubly ionised ions might contribute to absorption. However, as the emission spectra observed experimentally are time and space integrated, and a plasma contains a large variety of ion stages, it is difficult to isolate the contribution due to absorption by only low ion stages. The cross section of mid or highly ionised Gd plasmas should be measured in future work.

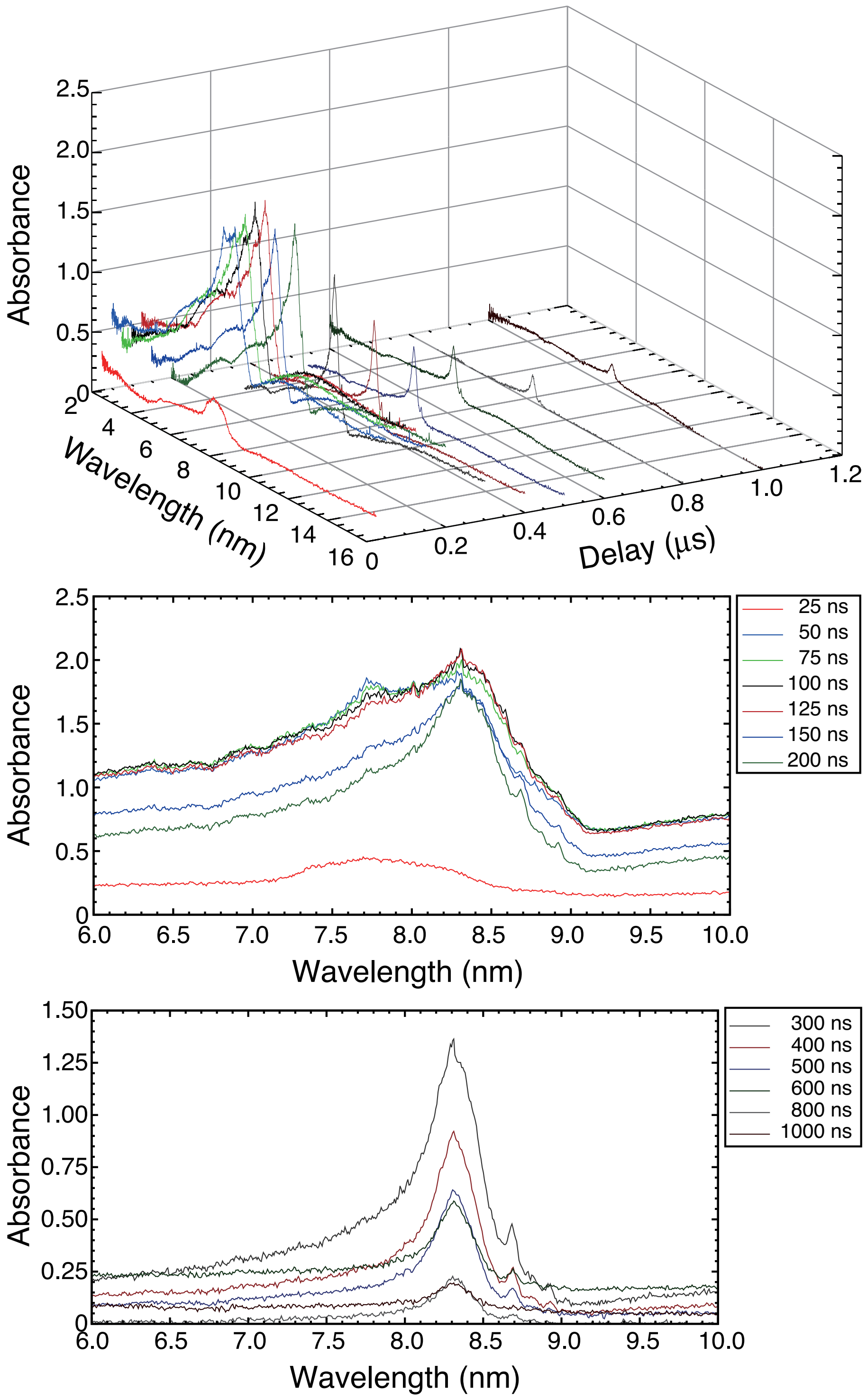

Figure 4.5 Photabsorption spectra of gadolinium plasmas at different delay times.

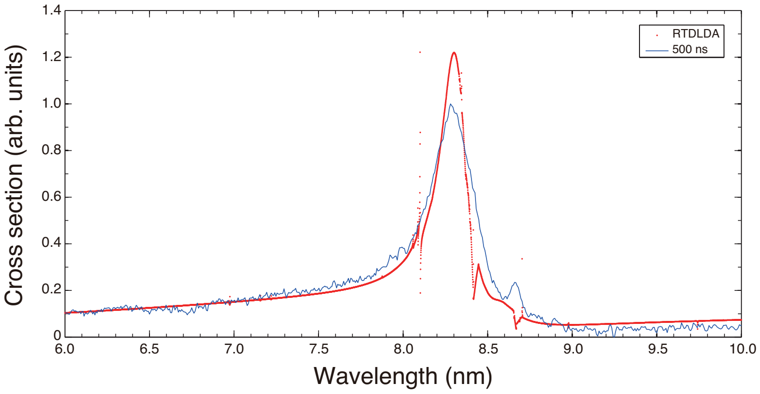

Figure 4.6 Comparison of the theoretical cross section and observed spectra at the delay time of 500 ns.

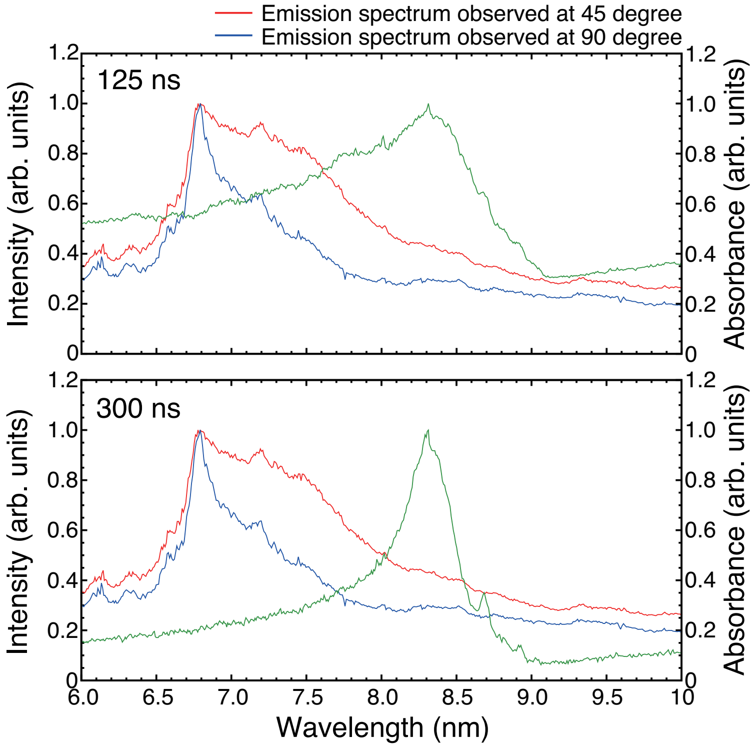

Figure 4.7 Comparison between emission spectra and absorption spectra. The red solid line corresponds to the spectrum observed at 45 degree, and the blue solid line corresponds to the spectrum observed at 90 degree, respectively Green solid lines shows experimentally observed photoabsorption spectra at the delay time of (a) 125 ns and (b) 300 ns, respectively.

4.5 Conclusion

In order to prove our previous conjecture, photoapsrotpion spectra of gadolinium ions have been observed.

The structure of the photoabsorption spectra were similar to previous work, and agreed well with RTDLDA calculation results. The maximum calculated value of cross section for Gd I was 65.9 Mb at 8.3 nm.

The emission spectra and the photoabsorption spectra were compered. Broad absorption from 6.8 - 8.0 nm has been observed in emission spectra, however, the cross section was maximised at 8.3 nm in the photoabsorption spectra. As the emission spectra observed experimentally are time and space integrated, and a plasma contains a large variety of ion stages, thus, it is difficult to conclude that due to absorption by low ion stages only.

For accurate evaluation of light sources, the cross sections of highly ionised Gd plasmas should be measured in future work.

Reference

[1] S. S. Churilov, R. R. Kildiyaraova, A. N. Ryabtsev, and S. V. Sadovsky, "EUV spectra of Gd and Tb ions excited in laser-produced and vacuum spark plasmas", Phys. Scr. **80**, 045303 (2009).

[2] T. Otsuka, D. Kilbane, J. White, T. Higashiguchi, N. Yugami, T. Yatagai, W. Jiang, A. Endo, P. Dunne, and G. O'Sullivan, "Rare-earth plasma extreme ultraviolet sources at 6.5-6.7 nm", Appl. Phys. Lett. **97**, 111503 (2010).

[3] A. Sasaki, K. Nishihara, A. Sunahara, H. Furukawa, T. Nishikawa, and F. Koike, "Theoretical investigation of the spectrum and conversion efficiency of short wavelength extreme-ultraviolet light sources based on terbium plasma", Appl. Phys. Lett. **97**, 231501 (2010).

[4] T. Otsuka, D. Kilbane, T. Higashiguchi, N. Yugami, T. Yatagai, W. Jiang, A. Endo, P. Dunne, and G. O'Sullivan, "Systematic investigation of self-absorption and conversion efficiency of 6.7 nm extreme ultraviolet sources", Appl. Phys. Lett. **97**, 231503 (2010).

[5] T. Higashiguchi, T. Otsuka, N. Yugami, W. Jiang, A. Endo, B. Li, D. Kilbane, P. Dunne, and G. O'Sullivan, "Extreme ultraviolet sources at 6.7 nm based on a low-density plasma", Appl. Phys. Lett. **99**, 191502 (2011).

[6] B. Li, P. Dunne, T. Higashiguchi, T. Otsuka, N. Yugami, W. Jiang, A. Endo, and G. O'Sullivan, "Gd plasma source modeling at 6.7 nm for future lithography", Appl. Phys. Lett. **99**, 231502 (2011).

[7] T. Cummins, T. Otsuka N. Yugami, W. Jiang, A. Endo, B. Li, C. O'Gorman, P. Dunne, E. Sokell, G. O'Sullivan, and T. Higahsiguchi, "Optimizing conversion efficiency and reducing ion energy in a laser-produced Gd plasma", Appl. Phys. Lett. **100**, 061118 (2012).

[8] C. O'Gorman, T. Otsuka, N. Yugami, W. Jiang, A. Endo, B. Li, T. Cummins, P. Dunne, E. Sokell, G. O'Sullivan, and T. Higashiguchi, "The effect

of viewing angle on the spectral behavior of a Gd plasma source near 6.7 nm", Appl. Phys. Lett. **100**, 141108 (2012).

[9] B. Li, T. Otsuka, T. Higashiguchi, N. Yugami, W. Jiang, A. Endo, P. Dunne and G. O'Sullivan, "Investigation of Gd and Tb plasmas for beyond extreme ultraviolet lithography based on multilayer mirror performance", Appl. Phys. Lett. **101**, 013112 (2012).

[10] C. Suzuki, F. Koike, I. Murakami, N. Tamura, and S. Sudo, "Observation of EUV spectra from gadolinium and neodymium ions in the Large helical Device", J. Phys. B: At. Mol. Opt. Phys. **45**, 135002 (2012).

[11] B. Li, T. Higashiguchi, T. Otsuka, W. Jiang, A. Endo, P. Dunne, and G. O'Sullivan, "XUV spectra of laser-produced zirconium plasmas", J. Phys. B: At. Mol. Opt. Phys. **45**, 245004 (2012).

[12] M. Masnavi, J. Szilagyi, H. Parchamy, and M. C. Richardson, "Laser-plasma source parameters for Kr, Gd, and Tb. ions at 6.6 nm", Appl. Phys. Lett. **102**, 164102(2013).

[13] J. P. Connerade and M. Pantelouris, "On the profiles of the 'giant resonances' in Gd and GdF_3", J. Phys. B: At. Mol. Phys. **17**, L173 (1984).

[14] M. Richter, M. Meyer, M. Pahler, T. Prescher, E. v. Raven, B. Sonntag, and H. -E. Wetzel, "Experimental study of atomic $4d$ giant resonances by photoabsorption and photoelectron spectroscopy: Sm, Eu, and Gd", Phys. Rev. A, **40**, 7007 (1989).

[15] G. Kutluk, H. Ishijima, M. Kanno, T. Nagata, and A. T. Domondon, "A systematic study of photoionization of free lanthanide atoms in the $4d$ giant resonance region", J. Elec. Spec. Relat. Phenom. **169**, 67 (2009).

[16] J. P. Connerade, J. M. Esteva and R. C. Karnatak, "Giant Resonances in Atomes, Moleccules, and Solids", (Plenum Press, NATO ASI Series, Series B: Physics, **151**, 1987).

[17] L. Gaynor, "Inner shell $4d$ photo absorption spectroscopy of gas phase tellurium and cerium", (PhD. thesis, School of Physics, University College Dublin, 2006).

[18] J. T. Costello, J. -P. Mosnier, E. T. Kennedy, P. K. Carroll and G. O'Sullivan, "X-UV Absorption Spectroscopy with Laser-Produced Plasmas: A Review", Phys. Scr. **T34**, 77 (1991).

[19] P. Dunne, G. OSullivan, and V. K. Ivanov, "Extreme-ultraviolet absorption spectrum of Ga^{+}", Phys. Rev. A **48**, 4358 (1993).

[20] T. McCormack and G. O'Sullivan, "Core-excited transitions in Au I-like Th XII and U XIV", J. Phys. B: At. Mol. Opt. Phys. **26**, L327 (1993).

[21] C. McGuinness, G. O'Sullivan, P. K. Carroll, D. Audley, and M. W. D. Mansfield, "$3d$ absorption spectra of Sr I through Sr IV", Phys. Rev. A **51**, 2053 (1995).

[22] G. O'Sullivan, C. McGuinness, J. T. Costello, E. T. Kennedy, and B. Weinmann, "Trends in $4d$-subshell photoabsorption along the iodine isonuclear sequence: I, I^{+}, and I^{2+}", Phys. Rev. A **53**, 3211 (1996).

[23] R. D'Arcy, J. T. Costello, C. McGuinness and G. O'Sullivan, "Discrete structure in the $4d$ photoabsorption spectrum of antimony and its ions", J. Phys. B: At. Mol. Opt. Phys. **32**, 4859 (1999).

[24] N. Murphy, J. T. Costello, E. T. Kennedy, C. McGuinness, J. P. Mosnier, B. Weinmann and G. O'Sullivan, "Discrete structure in the $4d$ photoabsorption spectrum of tellurium and its ions", J. Phys. B: At. Mol. Opt. Phys. **32**, 3905 (1999).

[25] A. Cummings and G. O'Sullivan, "Discrete structure in the $4d$ photoabsorption spectra of Cs III, Cs IV and Cs V", J. Phys. B: At. Mol. Opt. Phys. **34**, 199 (2001).

[26] G. Duffy, P. v. Kampen, and P. Dunne, "$4d \rightarrow 5p$ transitions in the extreme ultraviolet photoabsorption spectra of Sn II and Sn III", J. Phys. B: At. Mol. Opt. Phys. **34**, 3171 (2001).

[27] G. Duffy and P. Dunne, "The photoabsorption spectrum of an indium laser produced plasma", J. Phys. B: At. Mol. Opt. Phys. **34**, L173 (2001).

[28] N. Murphy, P. Niga, A. Cummings, P. Dunne and G. O'Sullivan, "$4d \rightarrow 5p$ transitions in the EUV photoabsorption spectrum of Ba IV, Ba V and Ba VI", J. Phys. B: At. Mol. Opt. Phys. **39**, 365 (2006).

[29] N. Murphy, A. Cummings, G. O'Sullivan and P. Dunne, "$4d \rightarrow 5p$ transitions in the EUV photoabsorption spectrum of La V, La VI and La VII", J. Phys. B: At. Mol. Opt. Phys. **39**, 3087 (2006).

[30] M. Lysaght, D. Kilbane, N. Murphy, A. Cummings, P. Dunne, and G. O'Sullivan, "Opacity of neutral and low ion stages of Sn at the wavelength

13.5 nm used in extreme-ultraviolet lithography", Phys. Rev. A **72**, 014502 (2005).

[31] L. Gaynor, N. Murphy, P. Dunne, and G. O'Sullivan, "Extreme ultraviolet photoabsorption spectra of the Ce VI-Ce X isonuclear sequence", J. Phys. B: At. Mol. Opt. Phys. **41**, 245002 (2008).

[32] C. Banahan, C. McGuinness, J. T. Costello, D. Kilbane, J-P Mosnier, E. T. Kennedy, G. O'Sullivan, and P. v. Kampen, "The 5d photoabsorption spectra of Pb III and Bi IV", J. Phys. B: At. Mol. Opt. Phys. **41**, 205001 (2008).

[33] J. Filevich, J. Rocca, E. Jankowska, E. Hammarsten, K. Kanizay, M. Marconi, S. Moon, and V. Shlyaptsev, "Two-dimensional effects in laser-created plasmas measured with soft-x-ray laser interferometry", Phys. Rev. E **67**, 056409 (2003).

[34] A. Zangwill and D. A. Liberman, "A NONRELATIVISTIC PROGRAM FOR OPTICAL RESPONSE IN ATOMS USING A TIME- DEPENDENT LOCAL DENSITY APPROXIMATION", Comput. Phys. Commun. **32**, 63 (1984).

[35] D. A. Liberman and A. Zangwill, "A RELATIVISTIC PROGRAM FOR OPTICAL RESPONSE IN ATOMS USING A TIME-DEPENDENT LOCAL DENSITY APPROXIMATION", Comput. Phys. Commun. **32**, 75 (1984).

Chapter 5

Bismuth-Spectra Dependence on Laser Power Density

As mentioned in the previous chapter, emission spectra from laser produced highly ionised bismuth plasmas were investigated in this research. Because the dominant ion stage depends on the electron temperature of a plasma, investigation of optimum electron temperature is a necessary and elemental study for the evaluation of emission wavelengths of plasma based light sources. It has been already shown that the electron temperature of laser-produced plasmas are proportional to a product of laser power density, ϕ, and the wavelength of the laser pulse, λ, and given by, $T_\mathrm{e}[\mathrm{eV}] \approx 5.2 \times 10^{-6} A^{1/5} (\lambda^2 \phi\ [\mathrm{W/cm^2}])^{3/5}$ [1]. Thus, it is important to observation of emission spectra from plasmas by changing laser power densities, i.e. by changing the dominant ion stages present.

In this chapter, time integrated emission spectra at different laser power densities and their dependence on ϕ are shown and discussed.

5.1 Experimental setup

Figure 6.1 shows the schematic of experimental setup. The Surelite I and EKSPLA SL312 were employed. As described in chapter 3, these lasers supply nanosecond and picosecond laser pulses, respectively. The laser pulse was focused by a plano-convex lens ($f = 120$ mm) onto a planar bismuth targets placed in the target chamber. The target dimension was as follows: W 1 cm × H 1 cm × T 1 mm. The targets were mounted on a automatic stage and controlled by a computer to avoid cavity effect [2], i.e. to allow use fresh surface for every shot. The spot diameter was approximately 30-40 μm (full width at half maximum: FWHM). The maximum laser power densities were 5.3×10^{12} W/cm^2 for the nanosecond laser pulse and 9.5×10^{13} W/cm^2 for the picosecond laser pulse,

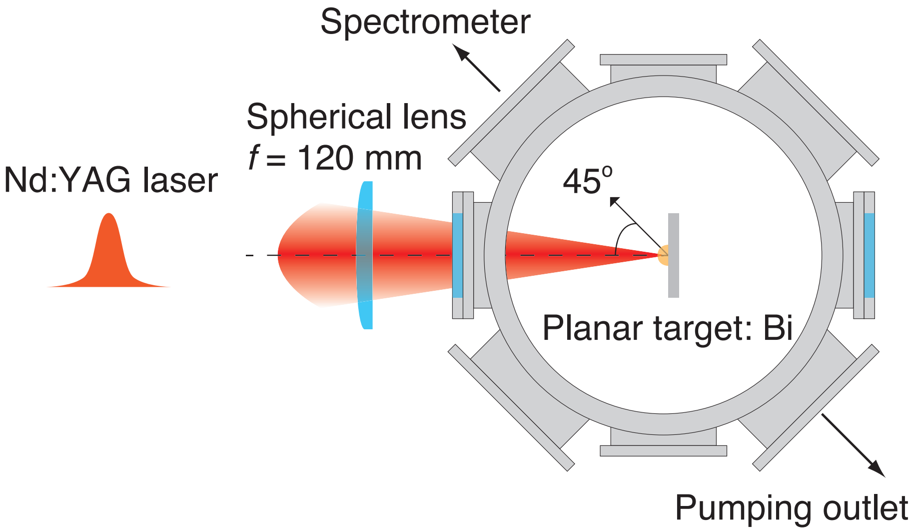

Figure 5.1 Schematic of experimental setup for single pulse irradiation.

respectively. The laser power density, ϕ_{Laser}, is given by

$$I_{\text{Laser}} = \frac{E_{\text{Laser}}}{\tau_{\text{Pulse}} \times \pi r_{\text{Spot}}^2}. \tag{5.1}$$

where, E_{Laser} is pulse energy, τ_{Laser} (FWHM) is pulse width and r_{Spot} is spot diameter of incident laser pulse at the target surface.

Emission spectra from the plasmas were observed by the grazing incident spectrometer, XUV-235-II, which was placed at 45 degrees with respect to the incident laser axis. Time-integrated spectra were measured by a thermoelectrically cooled back-illuminated X-ray charge coupled device (X-ray CCD) camera (Andor, DO420-BN). The lasers and the X-ray CCD camera were synchronised by a delay generator (Stanford Research System, DG645). The exposure time of the X-ray CCD camera was set at 100 ms. The observed spectra were calibrated by using carbon, nitrogen and silicon lines from C and Si_3N_4 targets.

5.2 Result and discussion

Figure 5.2 shows emission spectra from highly ionised bismuth plasmas created by nanosecond laser pulses. At the minimum laser power density, 2.2×10^{12} W/cm^2, the emission spectrum was almost purely a continuum spectrum. With increasing laser power density, strong emission was observed near 4.0 nm, which is mainly due to $n = 4 - n = 4$ transition. According to previous reports, this unresolved transition array (UTA) is attributable to mainly $4d-4f$ transition in Bi^{36+} - Bi^{45+} ions with an open $4d$ sub-shell [3, 4]. Intense emission was also observed in the spectral range of 2-3 nm, which is expected to arise from $n=4-n=5$ transitions, according to previous work on tungsten [5].

Figure 5.3 shows emission spectra from highly ionised bismuth plasmas created by picosecond laser pulses. For the case of mimimum laser power density, 4.8×10^{12} W/cm^2, the emission spectrum was essentially a continuum spectrum, and with increasing laser power density, the UTA were also observed as in the case of the nanosecond laser. The intensity of the UTA increased with increasing laser power density. As can be seen from figure 5.3(b), however, it was reached a maximum and saturated at 8.2 to 9.5×10^{13} W/cm^2. Intense emission in the spectral range of 2-3 nm was also observed for the picosecond laser case, however, the peak moves toward shorter wavelength with increasing laser power density. As can be seen from figure 5.3(c), significant change was observed especially between 3.7×10^{13} W/cm^2 and 4.3×10^{13} W/cm^2.

To aid in further analysis of the observed spectra, the in-band SXR energy, E_{Inband}, broadband energy, $E_{\text{Broadband}}$, spectral purity and conversion efficiency, C. E., are calculated.

$$E_{\text{Inband}} = \int_{\Delta\lambda=\pm0.01\,\text{nm}} I_{\text{Emission}}(\lambda)d\lambda \tag{5.2}$$

$$E_{\text{Broadband}} = \int_{2\,\text{nm}}^{5\,\text{nm}} I_{\text{Emission}}(\lambda)d\lambda \tag{5.3}$$

$$\text{C.E.} = \frac{E_{\text{Inband}}}{E_{\text{Laser}}} \tag{5.4}$$

$$\text{Spectral Purity} = \frac{E_{\text{Inband}}}{E_{\text{Broadband}}} \tag{5.5}$$

In-band energy is determined by the bandwidth, 0.02 nm (FWHM), of Cr/Sc multilayer mirrors [6–8]. The calculated value is not absolute value due to the spectrometer was not calibrated for energy. Thus, only relative behaviour as a function of laser power density can be discussed from these results. It is enough, however, to discuss from a physical point of view.

Figure 5.4 shows the calculated in-band SXR energy as a function of laser power density. The in-band SXR energy gives the optimum laser power density for getting the strongest emission. As can be seen from Figure 5.4(a), for the case of the nanosecond laser, in-band SXR energy increased with increasing laser power density, and it seems that it will increase further using more high laser power densities. Thus, for the nanosecond laser case, the electron temperature was not sufficient and further investigations are required.

On the other hand, for the picosecond laser case, as can be seen from Figure 5.4(b), the in-band energy saturated at 8×10^{14} W/cm^2 for all wavelength. And it

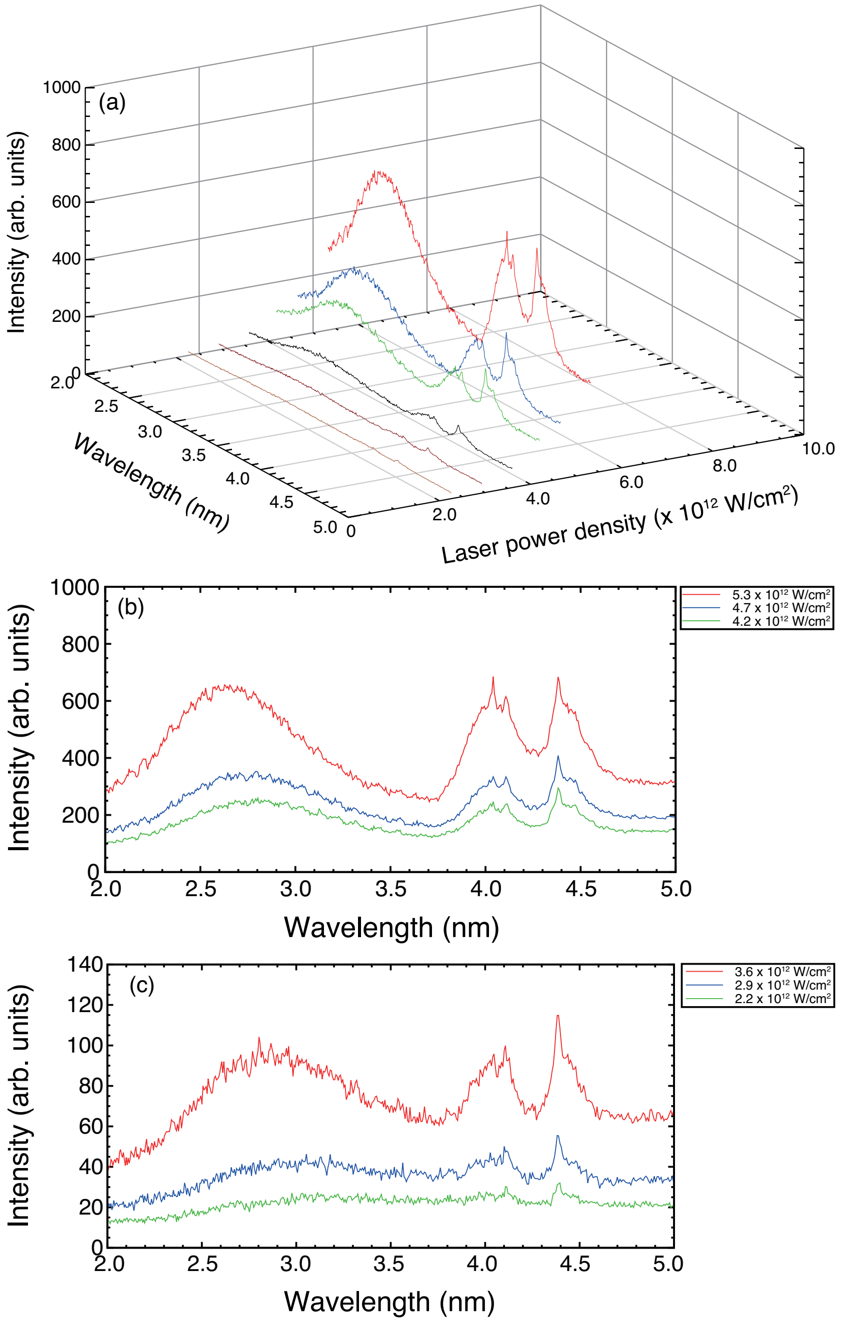

Figure 5.2 (a) Emission spectra from highly ionised bismuth plasmas generated by nanosecond laser pulse as a function of laser power densities and wavelength. (b) $4.2 - 5.3 \times 10^{12}$ W/cm^2, (c) $2.2 - 3.6 \times 10^{12}$ W/cm^2.

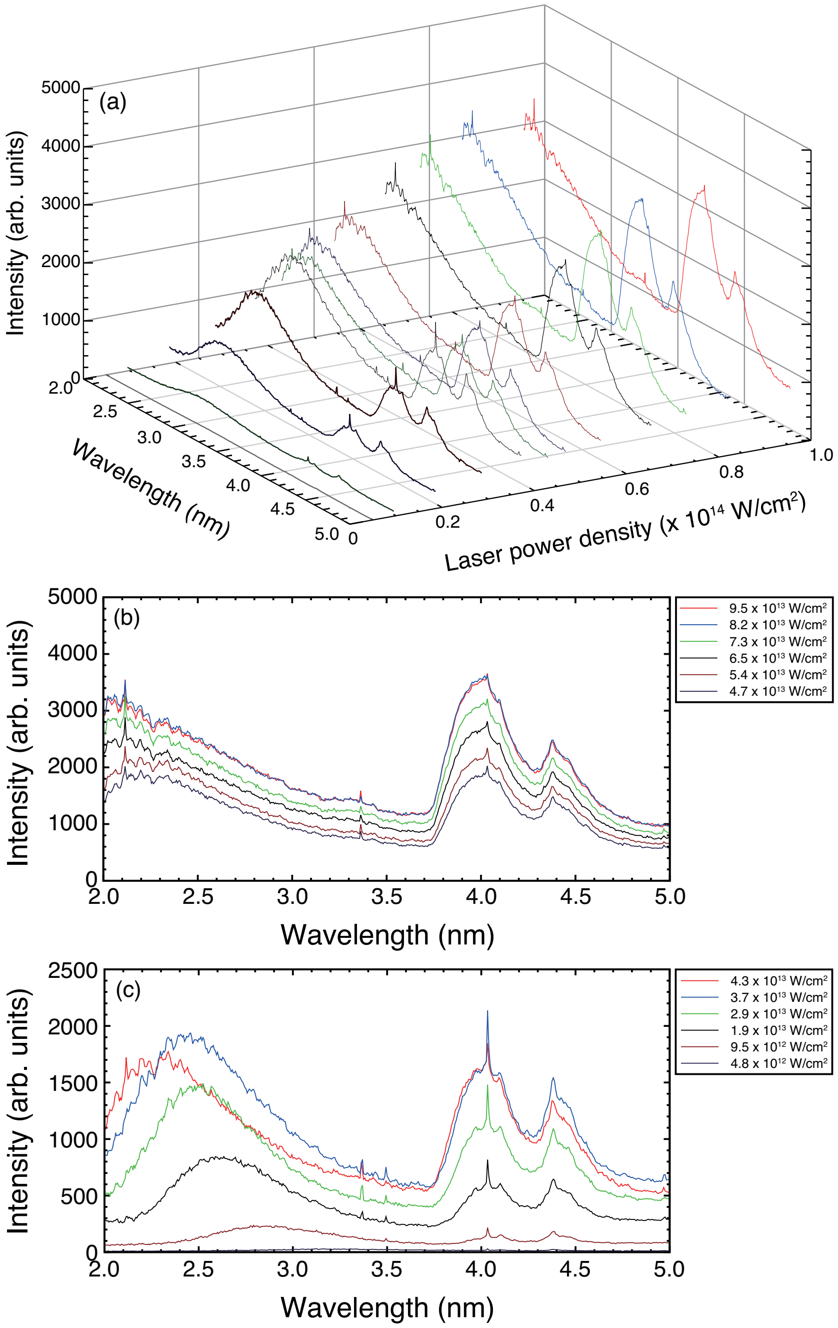

Figure 5.3 (a) Emission spectra from highly ionised bismuth plasmas generated by picosecond laser pulse as a function of laser power densities and wavelength. (b) $4.7 - 9.5 \times 10^{13}$ W/cm^2, (c) $4.8 \times 10^{12} - 4.3 \times 10^{13}$ W/cm^2.

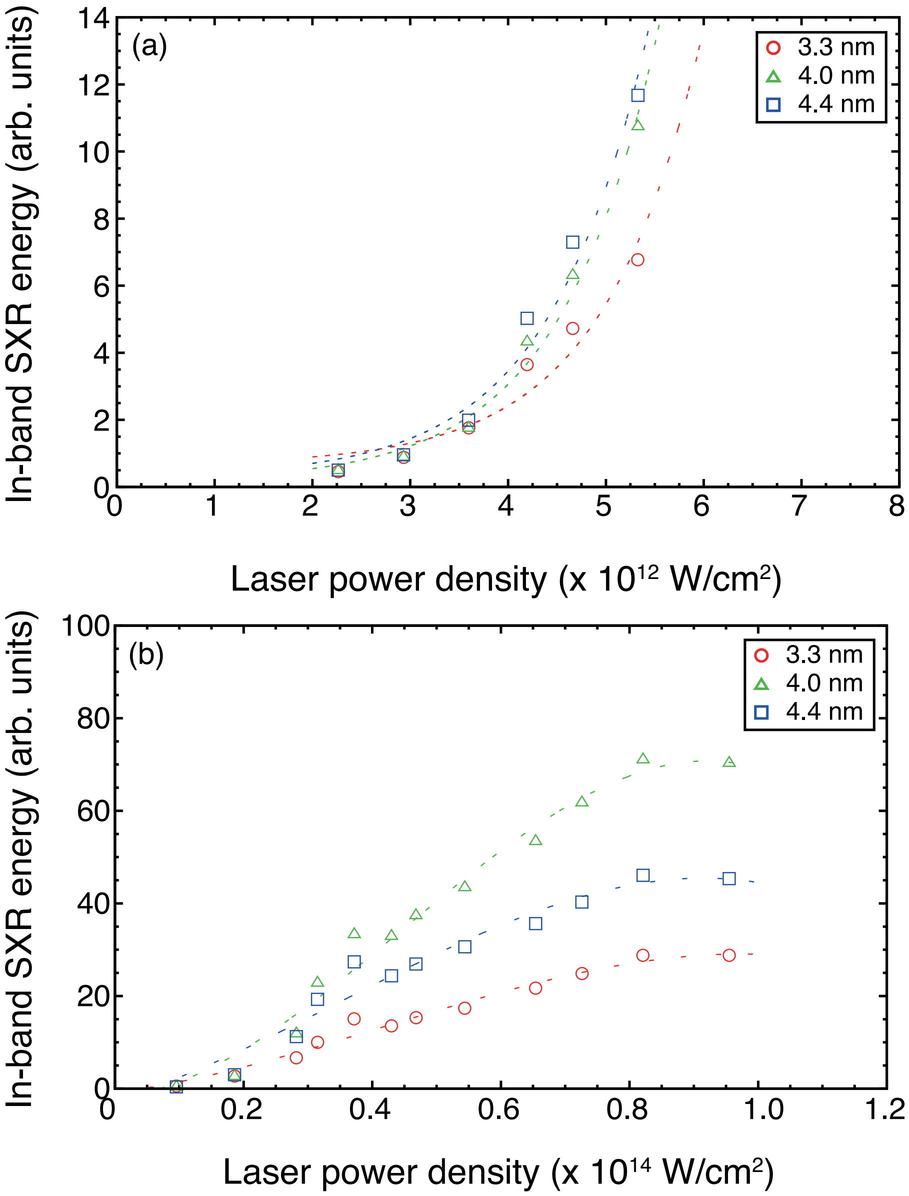

Figure 5.4 In-band SXR energy as a function of laser power densities, (a) for nanosecond laser pulse, (b) for picosecond laser pulse.

was not smooth at 4×10^{13} W/cm^2. This power density corresponds to the power density which big shift of the peaks in the 2-3 nm region was observed in figure 5.3(c).

Figure 5.5 shows the calculated broadband SXR energy as a function of laser power density. It was similar behaviour to in-band SXR energy for both lasers. It

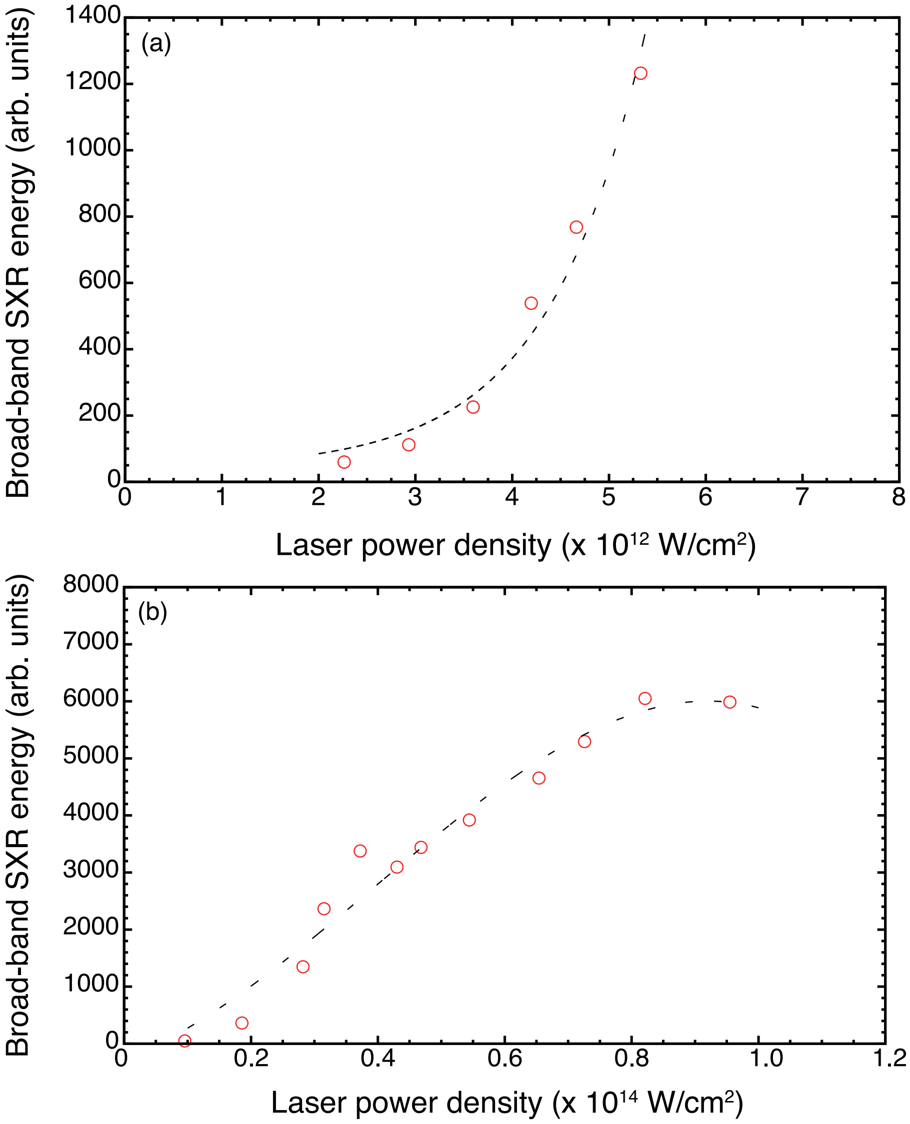

Figure 5.5 Broadband SXR energy as a function of laser power densities, (a) for nanosecond laser pulse, (b) for picosecond laser pulse.

was also not smooth at 4×10^{13} W/cm^2 for the picosecond laser case.

Figure 5.6 shows calculated spectral purities as a function of laser power density. For the case of nanosecond laser pulses, the spectral purity of 4.0 and 4.4 nm emission slowly increased with increasing laser power density. From the comparison of spectra in the picosecond case, laser power densities were too low for generating highly ionised bismuth plasmas which emit UTAs attributable to $4d - 4f$

transitions. Thus, it is expected that the spectral purity will keep increasing with increasing laser power density. On the other hand, the spectral purity for 3.3 nm emission slowly decreased with increasing laser power density. However, as can be seen from the spectra in figure 5.2, intense UTA emission at 3 nm which can be attributed to $4p-4d$ transitions was not observed except for continuum emission. Therefore, it can be expected that the spectral purity for this case was not affected by the UTA, but only affected by continuum emission.

For the case of picosecond laser plasmas, as can be seen from figure 5.6(b), it was found that there are changing points at 3×10^{13} W/cm^2 for all wavelengths. For the 4.0 nm case, it increases with increasing laser power densities from 2 to 5 $\times 10^{13}$ W/cm^2 and then, saturates at $\phi > 6 \times 10^{13}$ W/cm^2. However, the purity at 4.4 nm was a maximum at 3×10^{13} W/cm^2, and it was followed by slow decay and plateau while the purity for 4.0 nm increases. For the 3.3 nm case, the steep decrease was followed by a gradual increase at $\phi > 3 \times 10^{13}$ W/cm^2. In the spectra, figure 5.3, intense UTAs at 3.3 nm comes from $4p-4d$ transitions was not observed except for a small hump at $8-9 \times 10^{13}$ W/cm^2. Thus, it is not clear, however, this gradual increase might be affected by $4p-4d$ transitions.

For further analysis, these results were compered to calculation based on an average ion model, which is described in chapter 2 [1]. As described in chapter 2, the electron temperature, T_e, and average ion charge, Z, which are generated by the laser pulse, are determined by the atomic mass, A, the wavelength of laser pulse, λ (μm), and laser power density, ϕ_Laser [W/cm^2], according to

$$T_\mathrm{e} \simeq 5.2 \times 10^{-6} A^{1/5} (\lambda^2 I_\mathrm{Laser})^{3/5}\ [\mathrm{eV}] \tag{5.6}$$

$$Z \simeq \frac{2}{3}(A T_\mathrm{e})^{1/3} \tag{5.7}$$

Substituting equation 5.6 into equation 5.7, the relationship between the average ionic charge and laser power density is given by,

$$Z \simeq \frac{2}{3}(5.2 \times 10^{-6} A^{6/5} (\lambda^2 I_\mathrm{Laser})^{3/5})^{1/3}. \tag{5.8}$$

Figure 5.7 shows average ion stage as a function of laser power density.

As can be seen from 5.7, the average ion stage is Bi^{25} and Bi^{44} for the maximum power densities of the nanosecond and picosecond laser pulses used in this research, respectively. In the nanosecond case, it was found that power densities were too low to obtain emission from $4d-4f$ of bismuth according to a previous report [3]. This result suggests that it should be investigated again using more high power densities for the nanosecond case.

Previous work reported that emission wavelength of open $4f$ subshell ions of high-Z plasma move toward shorter wavelength, but in $4d$ ions moves to longer

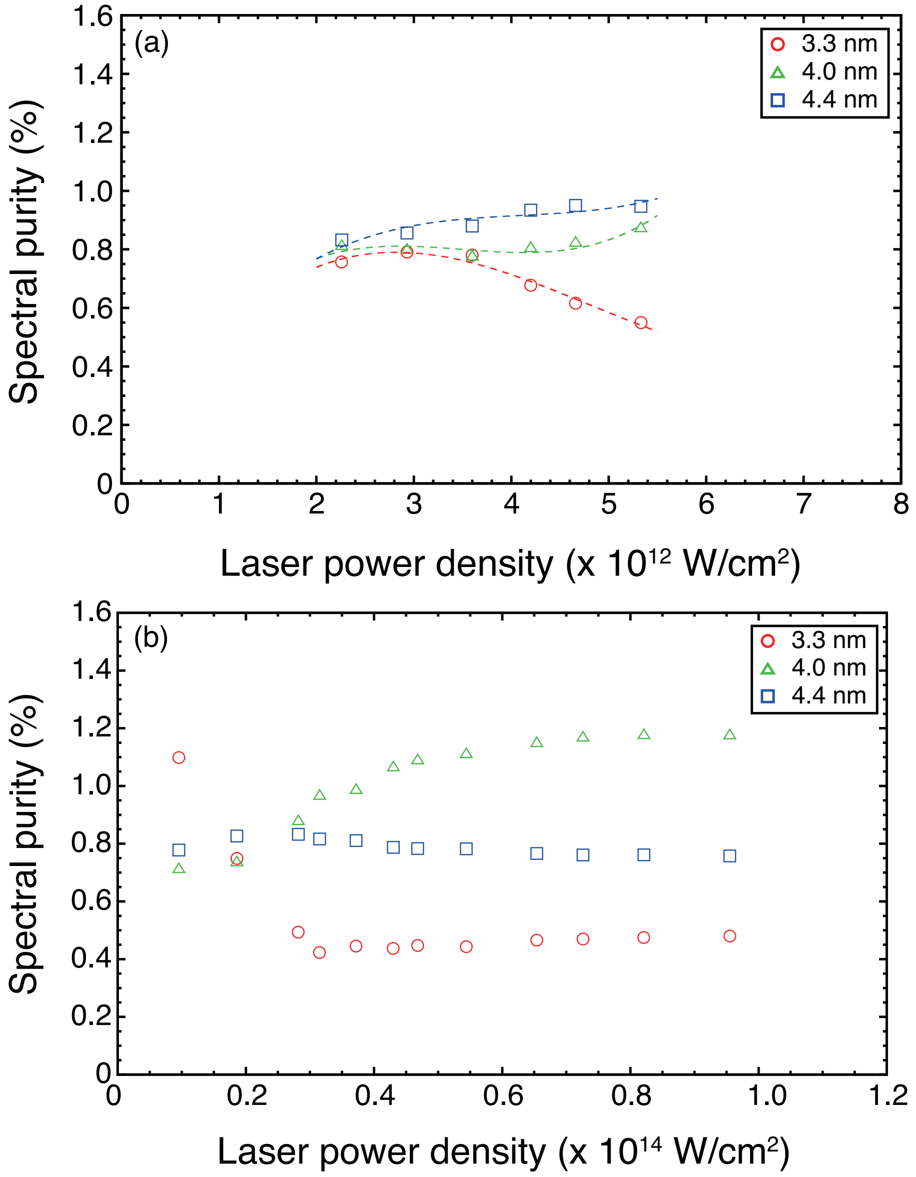

Figure 5.6 Spectral purity as a function of laser power densities, (a) for nanosecond laser pulse, (b) for picosecond laser pulse.

wavelength with increasing ion stage [9]. Numerical calculation shows that shortest wavelength of $4d - 4f$ transitions in bismuth appears in Bi^{37+}, and becomes longer with increasing ion stage [3]. The calculation also shows emission would be relatively low past Bi^{44+}.

The reason why the in-band energy for 4.0 nm was saturated at 8×10^{13} W/cm^2

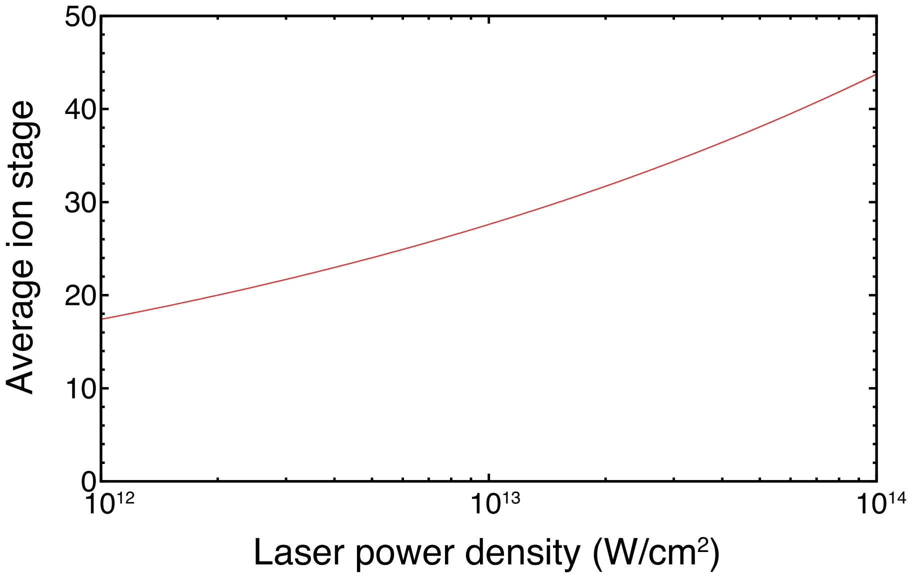

Figure 5.7 Average ion stage as a function of laser power density.

may be as follows. In this research, the ion stage, Bi^{44+}, corresponds to a maximum laser power density of about 1×10^{14} W/cm^2. As described, the average ion stage depends on laser power density. According to previous reports, one can not expect that there is a contribution to the in-band energy for 4.0 nm past Bi^{44+}.

This consideration also gives an explanation for the spectral purity behaviour. When the power density was 4×10^{13} W/cm^2 in the picosecond case, the average ion can be expected to be Bi^{36+} or Bi^{37+}. Bi^{37+} has the capability to emit at the shortest wavelength due to $4d - 4f$ transition around 4 nm. Thus, past that laser power density, there is less contribution to in-band energy for 4.0 nm from $4d - 4f$ transitions, but much more to out band, resulting in saturation of the spectral purity.

The calculation also shows spectra due to $4p - 4d$ transitions of bismuth [3]. According to the calculation, the emission attributed to $4p{-}4d$ transitions appears past Bi^{37+}. Hence, the change of the slope to a plateau in the spectral purity for 3.3 nm at 4×10^{13} W/cm^2 may be due to contribution to emission from $4p - 4d$ transitions to the spectra.

Figure 5.8 shows the conversion efficiency as a function of laser power density. As described, the spectrometer was not calibrated for energy, thus, calculated values do not absolute conversion efficiency. The conversion efficiencies were normalised to maximum values at each wavelength.

For the nanosecond case, the conversion efficiency was same behaviour as the

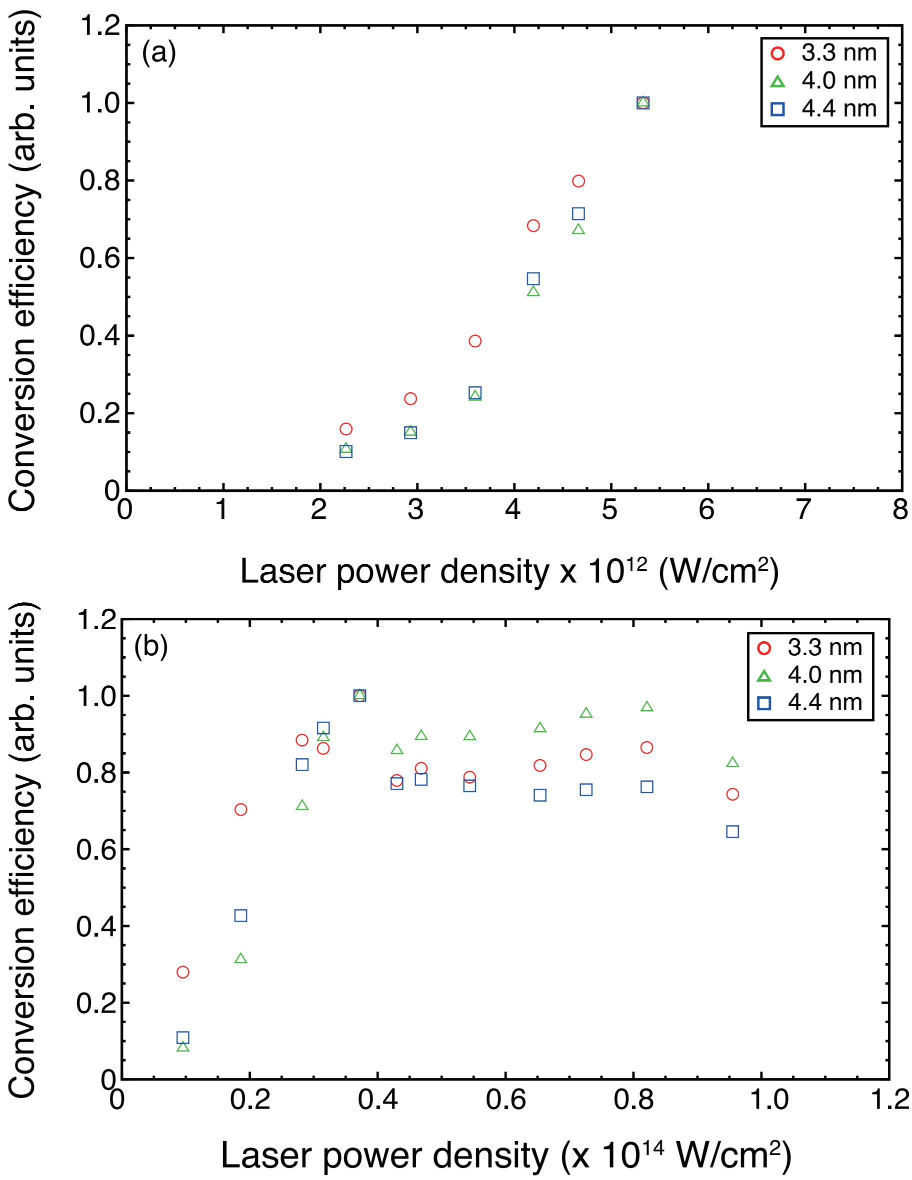

Figure 5.8 Conversion efficiencies as a function of laser power densities for the case of (a) nanosecond laser pulse and (b) picosecond laser pulse.

in-band energy. As described before, it is due to the laser power density being too low to ionise to the desired stages and needs further investigation.

On the other hand, for the picosecond case, the conversion efficiency increased with increasing laser power density below 4×10^{13} W/cm^2, and then plateaued. Thus, past 4×10^{13} W/cm^2, the in-band emission did not increase significantly, while the out band did increase. This result also can be concluded from the reasons described above for in-band energy and spectral purity.

From the results of spectral purity and conversion efficiency, for the SXR source using 4.0 nm, 7×10^{13} W/cm^2 is the optimum laser power density, while 3×10^{13} W/cm^2 is optimum for 4.4 nm operation. Conversion efficiency is an important value for practical sources for estimating output power and feasibility. Spectral purity also an important value, because out of band emission can destroy optics or cause flare on images. These results may indicate the capability of practical sources. However, it should be note that, in this research, only investigations using planar targets and Nd:YAG lasers were carried out. From the case of tin plasma based sources, it is clear that optimum conditions of laser power density are different for different target conditions and laser wavelength [10–14].

5.3 Conclusion

Emission spectra were observed from highly ionised bismuth plasmas, generated by the nanosecond, Surelite I, and picosecond, SL312, lasers at different laser power densities. The spectra were observed using an X-ray CCD camera attached on grazing incident spectrometer, XUV-235-II, which was placed at 45 degree with respect to the incident laser axis.

Emission originate from $4d-4f$ transitions were observed in the case of both lasers. However, intense emission due to $4p-4d$ transition, which is expected from numerical calculation [4], was not observed except for small hump at $8-9\times 10^{13}$ W/cm^2 in the case of the picosecond laser.

It was found that laser power densities generated by the nanosecond laser in this research were not sufficient to generate appropriate ions which emit radiation due to $4d-4f$ and $4p-4d$ transitions. Further investigation will be needed for nanosecond laser-produced bismuth plasmas.

The in-band energy of emission at 4.0 nm from picosecond laser-produced plasma, increased with increasing laser power density and became saturated at 8×10^{13} W/cm^2. The spectral purity of emission at 4.0 nm became saturated at 3×10^{13} W/cm^2. It can be concluded that the spectral emissive zone of $4d$ ions moves out of band with increasing ionisation.

For the case of the picosecond laser, the conversion efficiency of emission at 4.0 nm became saturated at 3×10^{13} W/cm^2. In order to explore the feasibility of creating a SXR light source using the UTA, the conversion efficiency should be measured by an absolutely calibrated SXR energy monitor, under different conditions, such as different wavelength of laser pulse and target conditions.

From these results, for best performance in terms of spectral purity and conversion efficiency of the SXR source based on the UTA at 4.0 nm, 7×10^{13} W/cm^2 is optimum laser power density, while 3×10^{13} W/cm^2 is optimum for 4.4 nm.

Reference

[1] D. Colombant and G. F. Tonon, “X-ray emisiion in laser-produced plasmas”, J. Appl. Phys. **44**, 3524 (1973).

[2] R. Kodama, T. Mochizuki, K. A. Tanaka, and C. Yamanaka, “Enhancement of extreme ultraviolet emission from a CO^2 laser-produced Sn plasma using a cavity target”, Appl. Phys. Lett. **91**, 231501 (2007).

[3] D. Kilbane, “Transition wavelengths and unresolved transition array statistics of ions with $Z = 72 - 89$”, J. Phys. B: At. Mol. Opt. Phys. **44**, 165006 (2011).

[4] T. Higashiguchi, T. Otsuka, N. Yugami, W. Jiang, A. Endo, B. Li, P. Dunne, and G. O’Sullivan, “Feasibility study of broadband efficient “water window” source”, Appl. Phys. Lett. **100**, 014103 (2012).

[5] C. S. Harte, T. Higashiguchi, T. Otsuka, R. D’Arcy, D. Kilbane, and G. O’Sullivan, “Analysis of tungsten laser produced plasmas in the extreme ultraviolet (EUV) spectral region”, J. Phys. B: At. Mol. Opt. Phys. **45**, 205002 (2012).

[6] F. Schäfers, H. C. Mertins, F. Schmolla, I. Packe, N. N. Salashchenko, and E. A. Shamov, “Cr/Sc multilayers for the soft-x-ray range”, Appl. Opt. **37**, 719 (1998).

[7] J. Birch, F. Eriksson, G. A. Johansson, and H. M. Hertz, “Recent advances in ion-assisted growth of Cr/Sc multilayer x-ray mirrors for the water window”, Vacuum, **68**, 275 (2003).

[8] F. Eriksson, G. A. Johansson, H. M. Hertz, E. M. Gullikson, U. Kreissig, and J. Birch, “14.5% near-normal incidence reflectance of Cr/Sc x-ray multilayer mirrors for the water window”, Opt. Lett. **28**, 2494 (2003).

[9] S. S. Churilov, R. R. Kildiyarova, A. N. Ryabtsev, and S. V. Sadovsky, “EUV spectra of Gd and Tb ions excited in laser-produced and vacuum spark plasmas”, Phys. Scr. **80**, 045303 (2009).

[10] H. Tanaka, A. Matsumoto, K. Akinaga, A. Takahashi, and T. Okada, “Comparative study on emission characteristics of extreme ultraviolet radiation from CO_2 and Nd: YAG laser-produced tin plasmas”, Appl. Phys. Lett. **87**, 041503 (2005).

[11] J. White, P. Dunne, P. Hayden, F. O’Reilly, and G. O’Sullivan, “Optimizing 13.5 nm laser-produced tin plasma emission as a function of laser wavelength”, Appl. Phys. Lett. **90**, 181502 (2007).

[12] S. Fujioka, M. Shimomura, Y. Shimada, S. Maeda, H. Sakaguchi, Y. Nakai, T. Aota, H. Nishimura, N. Ozaki, A. Sunahara, K. Nishihara, N. Miyanaga, Y. Izawa, and K. Mima, “Pure-tin microdroplets irradiated with double laser pulses for efficient and minimum-mass extreme-ultraviolet light source production”, Appl. Phys. Lett. **92**, 241502 (2008).

[13] V. Y. Banine, K. N. Koshelev, and G. H. P. M. Swinkels, “Physical processes in EUV sources for microlithography”, J. Phys. D: Appl. Phys. **44**, 253011 (2011).

[14] T. Tomie, “Tin laser-produced plasma as the light source for extreme ultraviolet lithography high-volume manufacturing: history, ideal plasma, present status, and prospects”, J. Micro/Nanolith. MEMS MOEMS **11**, 021109 (2012).

Chapter 6

Dual-pulse Irradiation Studies of Bismuth Plasmas

6.1 Introduction

As described already, plasmas generated by Nd:YAG laser are hot and dense, with a density of approximately $1.9 \times 10^{21}\,\mathrm{cm}^{-3}$ and an electron temperature of several hundred eV. Therefore much of the emitted radiation such as EUV and Soft X-ray, may be absorbed by the plasma itself. To understand these absorption effects and its impact on a plasma source, accurate analysis of absorption effects are important. For the case of tin plasma based EUV sources, many investigations were carried out to reduce the absorption effects and achieve a high power light source. As a result, laser pulses of longer wavelength, 10.6 µm, and mass limited targets are employed to reduce the absorption effects in next generation EUV lithography sources. These results came from experimental studies and numerical analysis was also needed. These studies are also important for this work and should be repeated for particular sources.

One method for reducing the effect of absorption is the dual-pulse irradiation technique. The dual-pulse irradiation technique involves the processes of pre-heating and re-heating, which are used in the generation and investigation of laser-produced plasmas. First, a pre-pulse generates pre-plasma, and this plasma expands into the vacuum, resulting in a gentle electron density gradient. The main pulse then propagates in the plasma, coupling more energy to the electrons. This technique can enhance the absorption of energy from the main laser pulse compared to the single pulse irradiation scheme. Injecting the main laser pulse at different times will also yield absorption of the laser energy by pre-generated plasma. The variation in the electron density gradient of the pre-generated plasma can be taken as a variation in the optical thickness. Thus, it is possible to obtain information on self-absorption effects by using the dual-pulse irradiation technique. This technique is successfully used in next-generation EUV lithography sources, laser induced spectroscopy and for investigations into nuclear fusion [1–5].

In this chapter, experimentally observed spectra using the dual-pulse irradiation technique are shown.

6.2 Experimental setup

Figure 6.1 shows a schematic of the experimental setup for dual-pulse irradiation. A frequency doubled Surelite I and the EKSPLA SL312 laser were employed to give a pre-pulse and main pulse, respectively. These lasers supply nanosecond and picosecond laser pulses, respectively. The laser pulses were focused by a plano-convex lens ($f = 120$ mm) onto a planar bismuth target placed in the target chamber. The target dimensions were as follows: W 1 cm × H 1 cm × T 1 mm. The target was mounted on an automatic stage and controlled by computer to avoid effects due to cratering [6], i.e. to use a fresh surface for every shot. The spot diameter was approximately 30-40 µm (FWHM). The maximum laser power densities were 4×10^{12} W/cm^2 for the nanosecond laser pulse, and 1×10^{14} W/cm^2 for the picosecond laser pulse, respectively.

Emission spectra from plasmas were observed using a grazing incident spectrometer, XUV-235-II, placed at 45 degrees with respect to the incident laser axis. Time-integrated spectra were measured using a thermoelectrically cooled back-illuminated X-ray charge coupled device (X-ray CCD) camera. The lasers and the X-ray CCD camera was synchronised by two delay generators (Stanford Research System, DG645 and DG535). The exposure time of the X-ray CCD camera was set to be 100 ms. The observed spectra was calibrated by using known carbon, nitrogen and silicon spectral lines.

The delay time was also controlled by the delay generator, DG645, and the delay time was measured by a PIN photo diode placed at just beside entrance window of the target chamber. The delay time was varied between -500 ns and 3 µs.

Figure 6.2 (a) and (b) show time-integrated emission spectra from the plasmas generated by the individual main-pulse and pre-pulse, respectively. The spectrum generated by the main pulse corresponds to the single pulse case.

For the case of single pulse irradiation, UTA emission was observed at 4.0 and 4.4 nm, as reported in chapter 5. Some features were observed in the spectra generated by the pre-pulse, however, the intensities were almost an order of magnitude less than those due to single pulse irradiation. It is expected that the conversion efficiency would be enhanced by varying the power density of pre-pulse [1], however, the power density of the pre-pulse was maintained constant in

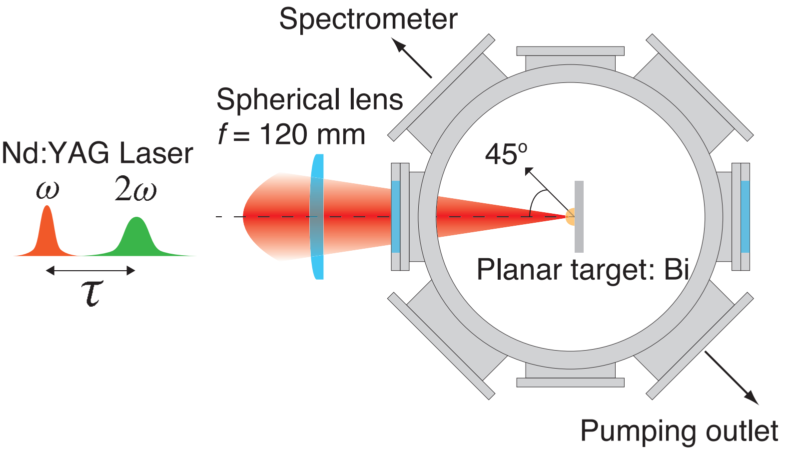

Figure 6.1 Schematic of the experimental setup for the dual-pulse irradiation method.

this research.

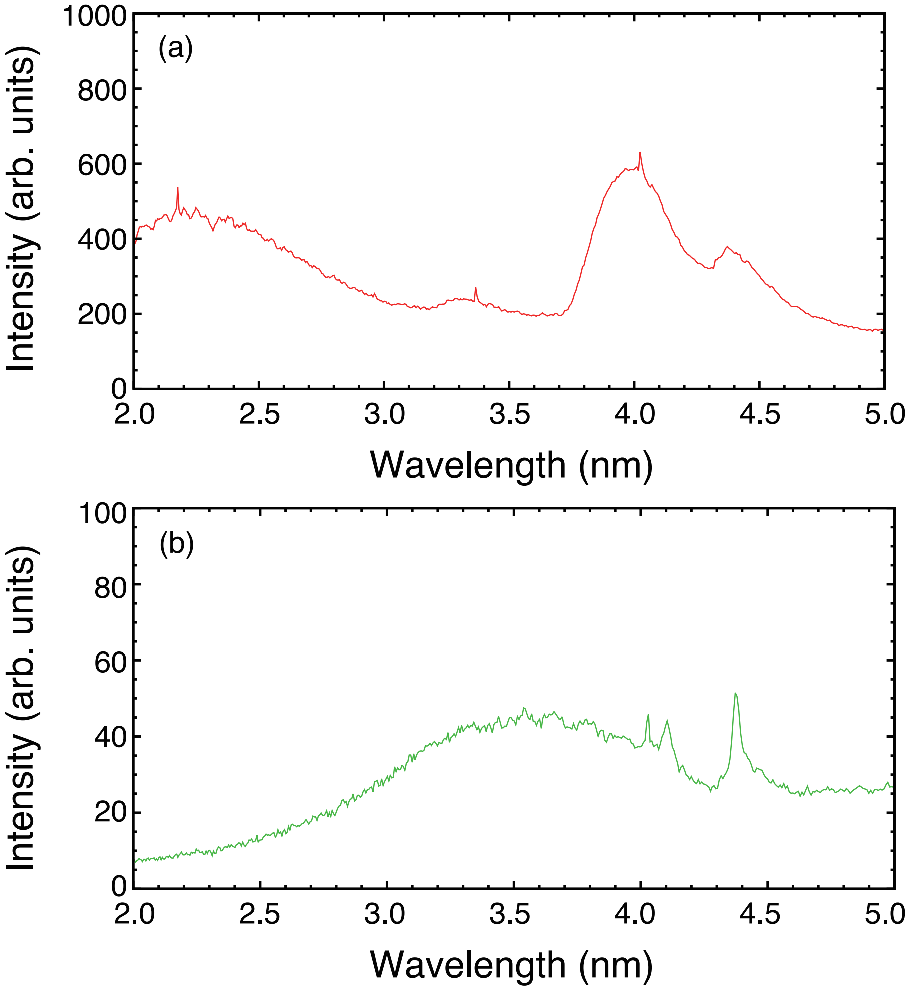

Figure 6.2 Emission spectra from a Bi plasma generated by (a) main-pulse, and (b) pre-pulse.

6.3 Results & discussion

Figures 6.3 and 6.4 show emission spectra from bismuth plasmas, which were generated by the dual-pulse irradiation scheme, at different delay times. For all delay times, emission attributable to $4d - 4f$ transitions around $4.0 - 4.4$ nm in highly ionised plasma was observed. However, except for enhancement around a delay of 6 ns, strong emission attributable to $4p - 4d$ transitions around 3.3 nm was not observed.

To study the dependence of the emission on the delay time, in-band SXR energies for 3.3, 4.0 and 4.4 nm were calculated. Figure 6.5 shows the in-band SXR energy dependence of the delay times: (a) 3.3, (b) 4.0 and (c) 4.4 nm. For comparison, the in-band SXR energy for single pulse irradiation is also shown as a dashed horizontal line. All data were normalised to the maximum values of the dual pulse irradiation. Figure 6.6 shows a zoomed-in region of figure 6.5.

The observed dependences can be characterised into three clear regions: region one is the increase of the in-band SXR energy, the second region is characterised by a decrease of the in-band SXR energy, and the third is the increase and plateau of the in-band SXR energy equal to the single-pulse case.

In region one, the in-band SXR energy increased steeply with increasing delay time between the two pulses at all wavelengths, resulting in maximum value at 6-10 ns. The maximum values showed an enhancement by a factor of 1.6 from its single-pulse value. This enhancement also can be seen from the spectra, in figure 6.3.

A reasonable explanation for the 6-10 ns peaks is follows. The pre-pulse interacts with the target, generating a hot and dense plasma, which expands freely into the vacuum. The main pulse is therefore not interacting with a cold solid target but with a hot plasma target. This difference enhances the absorption of energy from the main laser pulse compared to that obtained with single pulse irradiation, unless the second pulse comes either very early, or a long time after the pre-pulse. The main laser pulse is thus mainly absorbed by the first plasma. Hence, the main advantage of dual-pulse irradiation is to enable interaction of the main pulse with an existing plasma generated by the pre-pulse, without losing the laser energy to ionisation of the target and effectively using it for plasma heating. The dominance of this absorption mechanism can be expected to depend on the delay time.

As the pulse delay Δt is increased from zero, giving the first plasma time to expand, the effect of the first laser pulse in optimising the interaction of the second laser pulse increases. At 6-10 ns delay, the data show that the plasma and target conditions are appropriate at this delay time for the interaction between pre-generated plasma and the main laser pulse to be maximised and that the interaction volume is optimised.

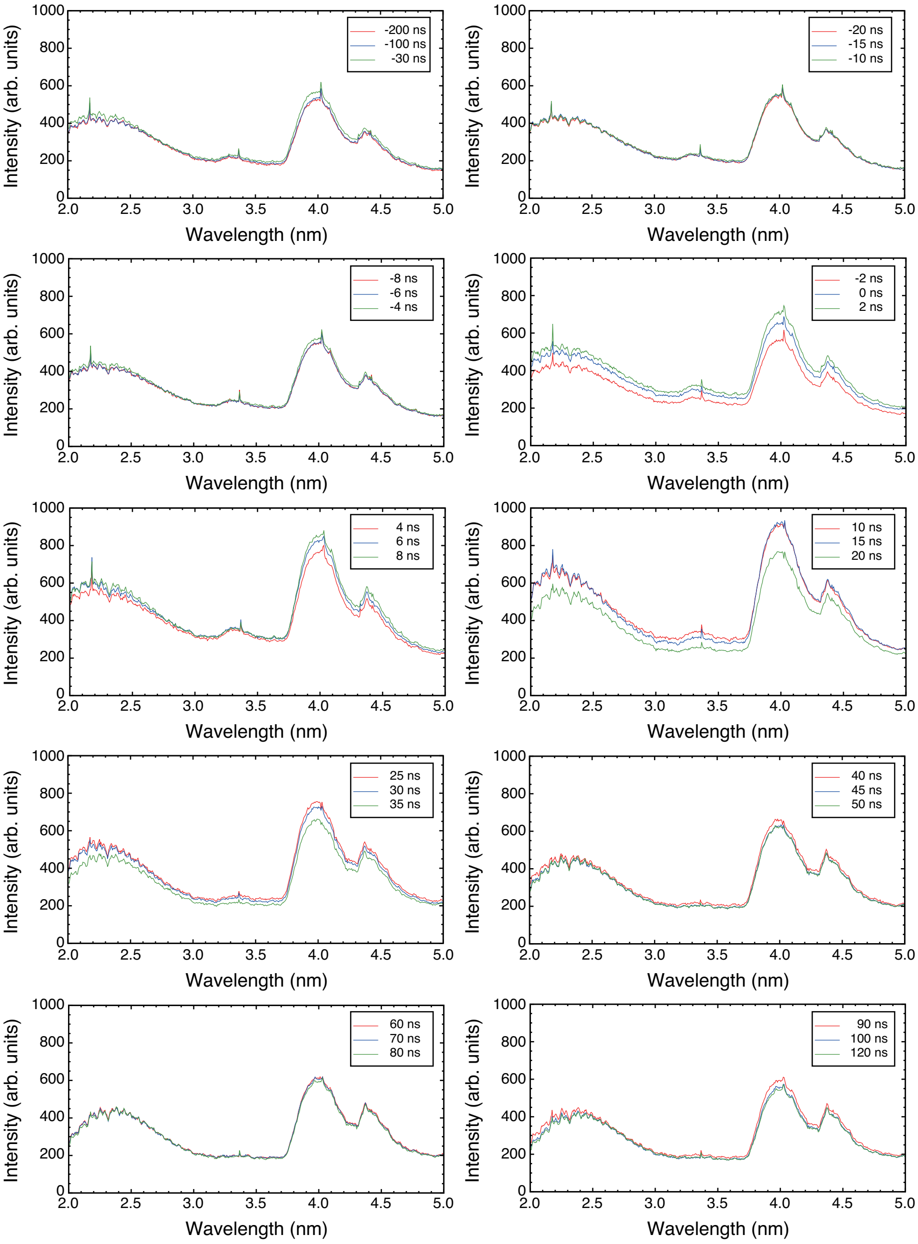

Figure 6.3 Emission spectra from Bi plasmas at different delay times A.

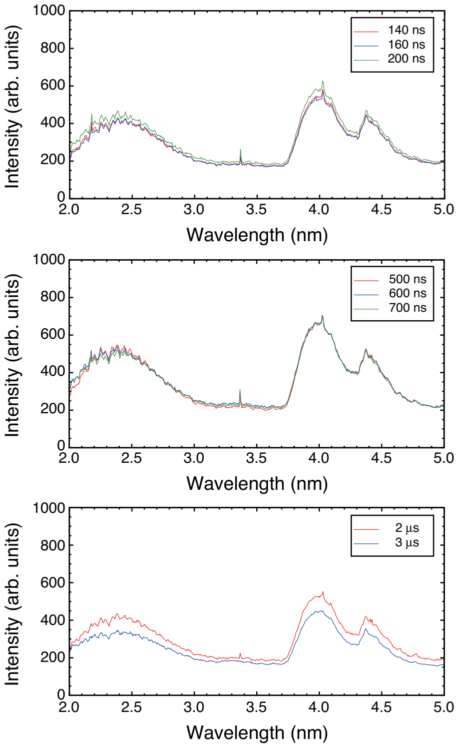

Figure 6.4 Emission spectra from Bi plasmas at different delay times B.

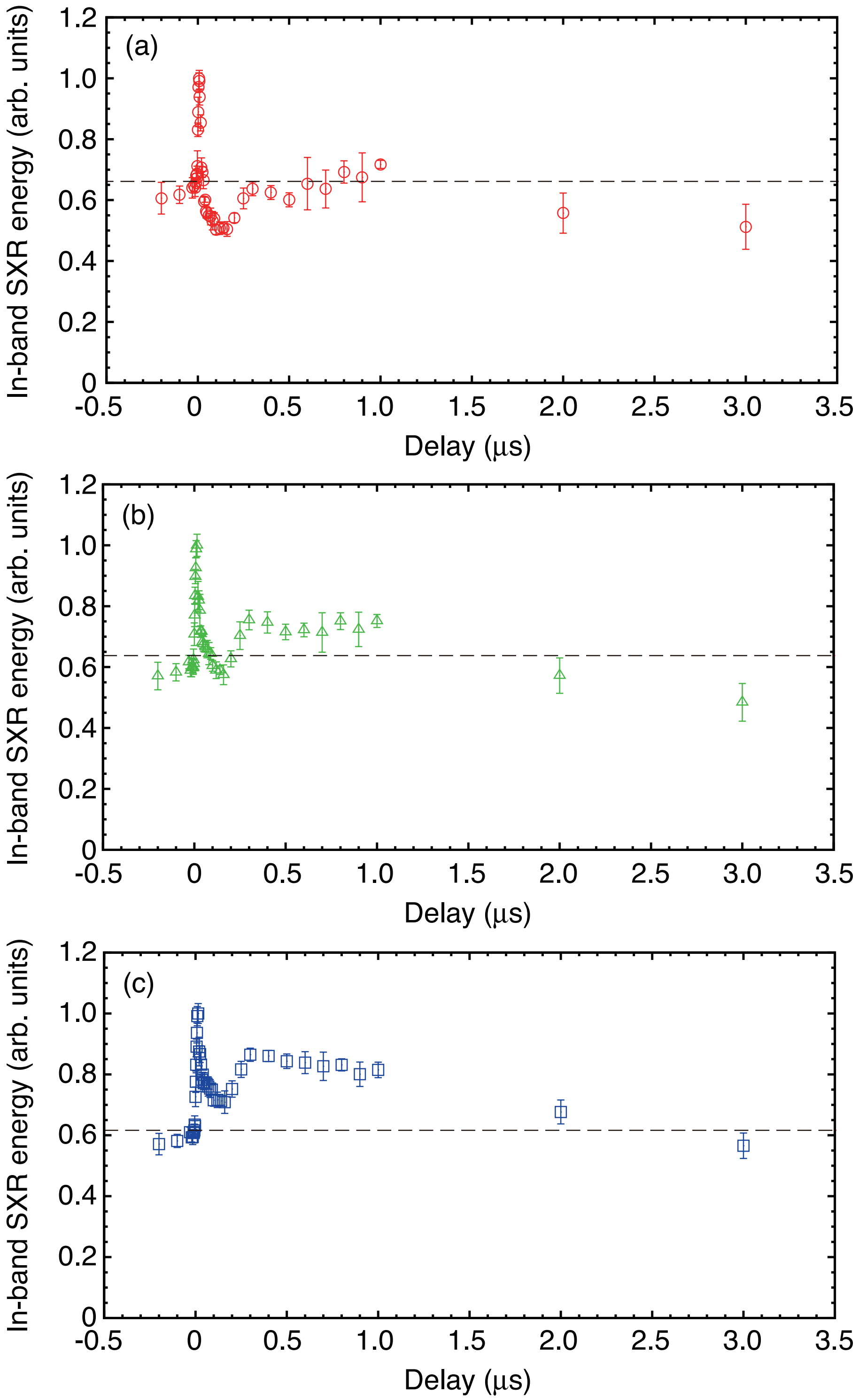

Figure 6.5 In-band SXR energy of (a) 3.3 nm, (b) 4.0 nm, (c) 4.4 nm, respectively

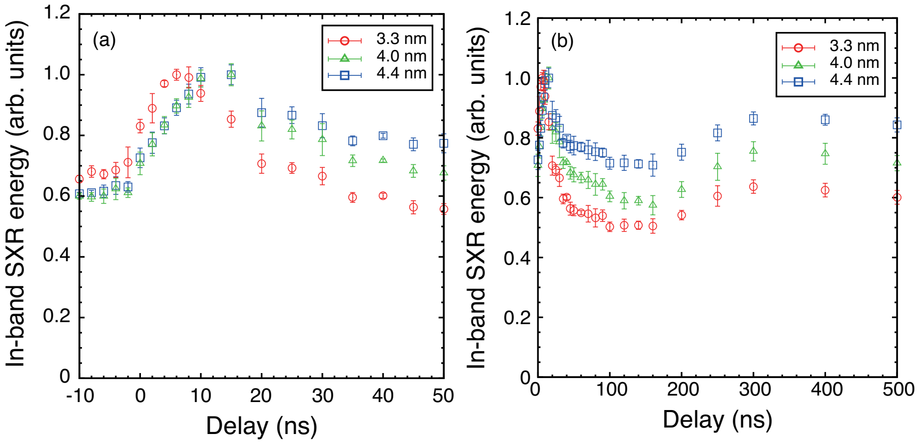

Figure 6.6 In-band SXR energy of (a) -10 - 50 ns, (b) 0 - 500 ns.

The time delay at which the in-band SXR energy was maximised was slightly different for 3.3-nm emission. It can be expected as the main pulse was injected before the pre-generated plasma cools down. Thus, this result might be due to differences in the required plasma temperature, however, there is no hydrodynamic code to calculate and conclude this for such high-Z ions.

When the time delay between the two laser pulses is increased beyond 10 ns, in region two, a rapid fall of the in-band SXR energy follows and intensity at all wavelengths declined even below the in-band SXR energy for single pulse irradiation shown by dashed horizontal lines for 3.3 and 4.0 nm at around 150 ns. For Δt >10 ns the pre-generated plasma has expanded into the vacuum, resulting in a large-scale length plasma and a reduced plasma density. This plasma will be cooler and contain mainly singly or doubly ionised ions. This large-scale length plasma may absorb the emission from the core of the plasma, while the lower density may reduce the absorption of the main laser pulse compared to that which occurs at the optimum delay time, 6-10 ns. From the results, it can be expected that the plasma is optically thick for emission at wavelengths of 3.3 and 4.4 nm and that the photons were absorbed by the low ion stages. The base line, the intensity of the continuum emission, is lower at 150 ns than that at 6-10 ns in figure 6.3 and 6.4

After that, in region three, the in-band SXR energy increased with increasing delay time, resulting in a second broad peak in the few hundred nanosecond range, and became a plateau where a slow decay can be observed for Δt > 100 ns for all wavelength.

In vacuum the pre-plasma density drops systematically as Δt increases. For very long time delays the pre-plasma has largely dissipated and the heating effect of the target is also reduced, implying that the main pulse is no longer affected by any plasma and that the interaction behaviour is similar to that of a single pulse incident on the target.

6.4 Conclusion

In this chapter, experimental results from the dual-pulse irradiation technique were shown. The advantage of dual-pulse irradiation is to enable interaction of the main pulse with an already generated plasma, without losing so much of the laser energy to ionisation of the target, effectively using it for plasma heating.

From emission spectra from highly ionised plasmas observed at a range of time delays, it was found that the intensity of 3.3, 4.0 and 4.4 nm emission was enhanced. Strong emission at 3.3 nm, attributable to $4p - 4d$ transitions, which was predicted by numerical calculation has yet to be observed, except for some enhancement around delays of 6 ns. The in-band SXR energy increased steeply with increasing time delay between the two pulses for all wavelengths, reaching a maximum value at 6-10 ns. The maximum value showed an enhancement by a factor of 1.6 compared to the single-pulse value. Absorption of the main pulse depends on the delay time in the dual-pulse irradiation technique. This result shows that the plasma and target conditions are most appropriate at this delay time for the interaction between the pre-generated plasma and the main laser pulse. When the time delay between the two laser pulses is increased beyond 10 ns, the in-band SXR energy decreased, declining even below the in-band SXR energy for single pulse irradiation. This is due to SXR absorption by the large-scale length plasma, while the lower density also reduces the absorption of the main laser pulse compared to that at the optimum delay time of 6-10 ns. For $\Delta t > 100$ ns, the in-band SXR energy increased with increasing delay time, resulting in a second broad peak in the few hundred ns range, and became a plateau with slow decay observed for all wavelengths. For very long time delays the first plasma has largely dissipated and the heating effect of the target is also reduced, implying that the main pulse was no longer affected by any plasma and the interaction behaviour is similar to that of a single picosecond pulse.

The times when in-band SXR energy were maximised were slightly different for 3.3 nm. According to previous reports, the emission at 3.3 nm can be attributed to $4p - 4d$ transitions of Bi^{38+} to Bi^{46+}, while the emission at 4.0 and 4.4 nm can be attributed to $4p - 4d$ transitions of Bi^{33+} to Bi^{40+}. Ion fraction depends on electron temperature. Thus, this result might be due to differences in the plasma temperature. However, there no hydrodynamic code was run to verify this for such high-Z ions.

The strong emission at 3.3 nm attributable to $4p - 4d$ transitions which was predicted by numerical calculation has yet to be observed, except for a fractional enhancement.

Reference

[1] R. Kodama, T. Mochizuki, K. A. Tanaka, and C. Yamanaka, “Enhancement of keV x-ray emission in laser-produced plasmas by a weak pre pulses laser”, Appl. Phys. Lett. **50**, 720 (1987).

[2] P. Dunne, G. O’Sullivan, and D. O’Reilly, “Prepulse-enhanced narrow bandwidth soft x-ray emission from a low debris, subnanosecond, laser plasma source”, Appl. Phys. Lett. **76**, 34 (2000).

[3] T. Higashiguchi, K. Kawasaki, W. Sasaki, and S. Kubodera, “Enhancement of extreme ultraviolet emission from a lithium plasma by use of dual laser pulse”, Appl. Phys. Lett. **88**, 161502 (2006).

[4] D. Nakamura, T. Akiyama, K. Okazaki, K. Tamaru, A. Takahashi, and T. Okada, “Ablation dynamics of tin micro-droplet irradiated by double pulse laser used for extreme ultraviolet lithography source”, J. Phys. D: Appl. Phys. **41**, 245210 (2008).

[5] M. Weidman, M Baudelet, S. Palanco, M, Sigman, P. J. Dagdigian, M. Richardson, “Nd:YAG-CO_2 double-pulse laser induced breakdown spectroscopy of organic films”, Opt. Express, **18**, 259 (2010).

[6] Y. Ueno, G. Soumagne, A. Sumitani, A. Endo, and T. Higashiguchi, “Enhancement of extreme ultraviolet emission from a CO^2 laser-produced Sn plasma using a cavity target”, Appl. Phys. Lett. **91**, 231501 (2007).

Chapter 7

Absorption Spectroscopy of Bismuth Plasmas

7.1 Introduction

Emission spectra from highly ionised plasmas have been shown in chapters 6 and 7. However, as described in the above chapters, the strong emission at 3.3 nm attributable to $4p - 4d$ transitions which was predicted by numerical calculation has yet to be observed, except for fractional enhancement in the dual-pulse irradiation experiment. Possible reasons for not observing this feature include the optical thickness of the Bi plasma itself and the inability to reach a sufficiently high plasma temperature. In addition, absorption and continuum emission were not included in the calculation.

To achieve a light source using plasma emission, an understanding of absorption effects of Bi ions is necessary. In order to obtain information on the optical thickness, absorption spectroscopy was carried out by way of the dual laser plasma photoabsorption technique. Absorption lines of Bi IV in the photon energy range 30-66 eV have already been reported by by Banahan *et al* [1]. However, absorption in the photon energy range above 66 eV to the water window region has not been reported.

In this chapter, the photoabsorption spectra of bismuth ions recorded using the dual laser plasma (DLP) technique are shown. Results from Cowan code and RTDLDA calculations are also shown.

7.2 Experimental setup

Figure 7.1 shows a schematic of the experimental setup, which is the same as that shown in chapter 4, except for the presence of an absorber plasma. The picosecond

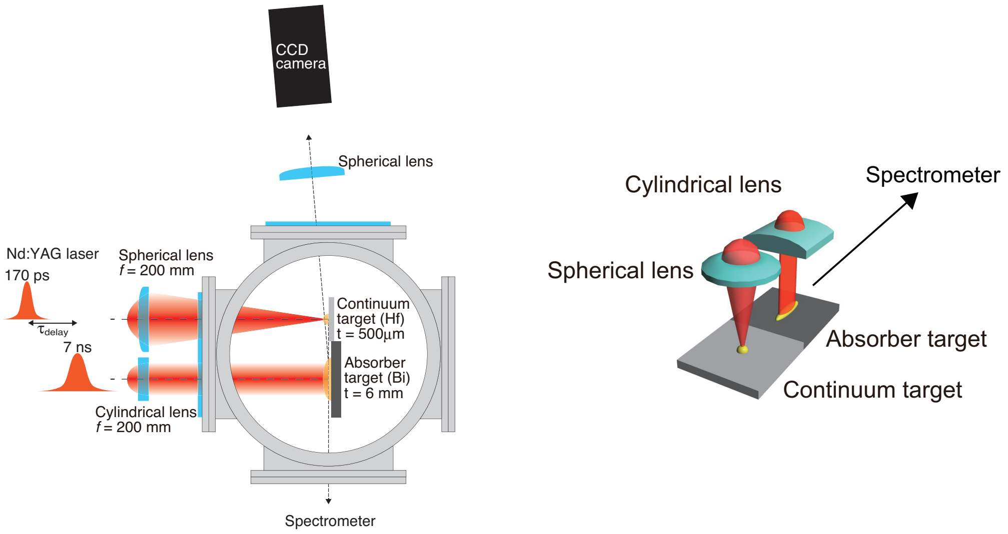

Figure 7.1 Schematic of the experimental setup for the dual laser plasma (DLP) technique.

laser pulse was focused by a plano-convex lens ($f = 200$ mm) onto a planar hafnium target placed in the target chamber, to generate a backlighting plasma. The absorbing plasma was generated by the nanosecond laser pulses, which were focused by a plano-convex cylindrical lens ($f = 200$ mm) onto a planar bismuth target placed in the target chamber. The target dimension was significantly larger than beam diameter at the focal point. The targets were mounted on an automatic stage and controlled by actuators from outside the chamber. The beam diameter on-target was approximately 400 µm (full width at half maximum: FWHM) in the case of the picosecond laser pulse, while the dimensions of the nanosecond pulse were 250 µ× 1 cm. Maximum laser power densities were 2.3×10^8 W/cm^2 for the nanosecond laser pulse, and 1.6×10^{11} W/cm^2 for the picosecond laser pulse, respectively.

Spectra from the plasmas were observed by a grazing incidence spectrometer, the UCD spectrometer, which was placed at 90 degrees with respect to the incident laser axis. Time-integrated spectra were measured by a thermoelectrically cooled back-illuminated X-ray charge coupled device (X-ray CCD) camera (Andor, DX436-BN). The lasers and the X-ray CCD camera were synchronised by delay generators (Stanford Research System, DG645 and DG535). The exposure time of the X-ray CCD camera was set to 1 second. The observed spectra were calibrated using known nitrogen and silicon emission lines.

As described in chapter 4, the ion stage distribution in the absorbing column is controllable by varying the laser power density. From the steady-state collisional-

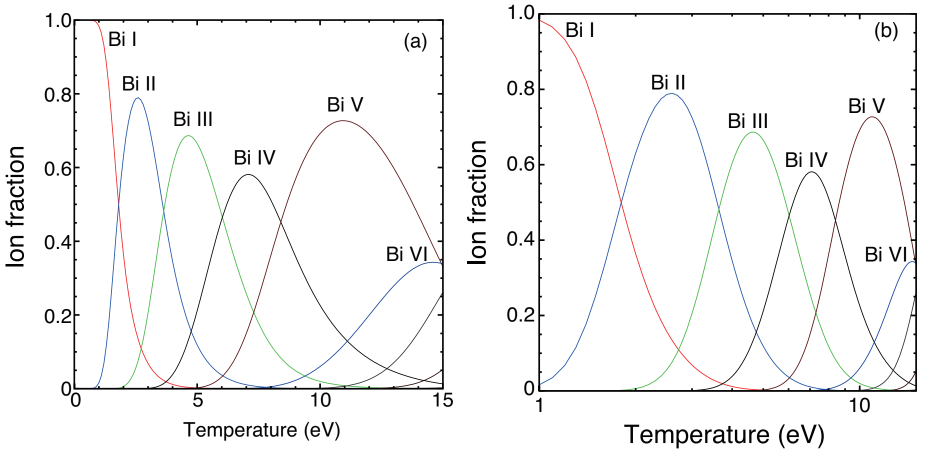

Figure 7.2 Ion distribution of a bismuth plasma as a function of electron temperature. (a) Linear X-scale, (b) Log X-scale. The calculation was done at an electron density of $1.0 \times 10^{21}\mathrm{cm}^{-3}$.

radiative ionisation model the ion fraction dependency on the electron temperature can be calculated [2]. Figure 7.2 shows the ion fraction as a function of electron temperature. Under the conditions of the laser power density employed in these experiments, the maximum electron temperature was calculated as 1.4 eV. Thus, the continuum radiation will be absorbed by neutral and singly ionised bismuth. Note that the laser power density was measured on burn paper, giving maximum spot sizes, so the power density presented represents the minimum laser power density.

7.3 Results and discussion

The photoabsorption spectra of bismuth ions in the $52 - 200$ eV photon energy region at different delay times are presented in 7.3. Measurements at lower energies were not possible due to the limited range available with the spectrometer. There are broad features and a gradual decreasing slope in the $70 - 125$ eV region. The absorbance at a delay time of 50 ns is lower than that of other delay times. In the case of shorter delays, the absorbing plasma had not fully expanded into the optical axis, thus, it is due to a low density of ions in absorber. And, not only a broad features but also narrow absorption lines were observed in about 150 to 200 eV region. Note that, the dip at 100 eV is due to $L-$ absorption edge of silicon present in the CCD array. From the calculation of the ion fractions, these absorption feature are expected to be due to neutral Bi and Bi^{+} ions.

A previous report was used in order to study the structures observed in the experimental spectra [1]. In this report, absorption lines of Bi IV attributed to $5d$ inner-shell excitations in the photon energy range 30-66 eV were shown. Absorption spectra observed in this current work in this photon energy region were compared to the results in previous report. The photoabsorption spectra of bismuth plasmas in the $52-200$ eV photon energy region at different delay times are presented in 7.3. Figure 7.4 shows the photoabsorption spectra of bismuth iones in in the photon energy range at different delay times. $5d$ absorption lines of Bi^{3+} have also been observed in this research, and they have disappeared at delay times past 125 ns. Thus, it can be concluded that Bi^{3+} or higher stages dominate for $\Delta t \leq 125$ ns, and Bi^{3+} or lower stages dominate for $\Delta t \geq 125$ ns. Assuming this condition, calculations were carried out in order to identify the structures of the experimental spectra for the delay times of 125 and 400 ns, which are dominated by Bi^{3+} or higher stages and Bi^{3+} or lower stages, respectively.

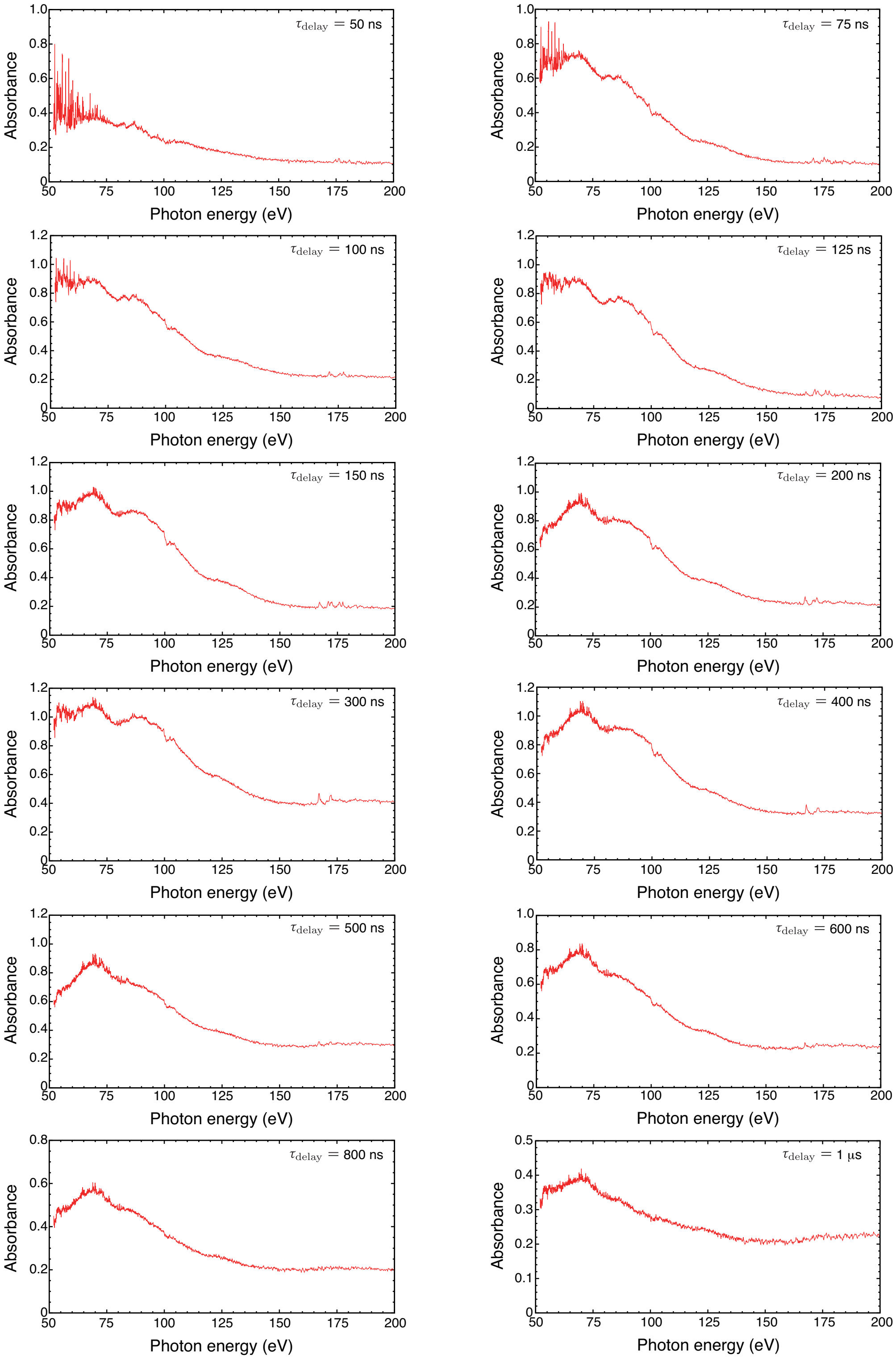

Figure 7.3 Absorbance of a bismuth plasma at a range of delay times.

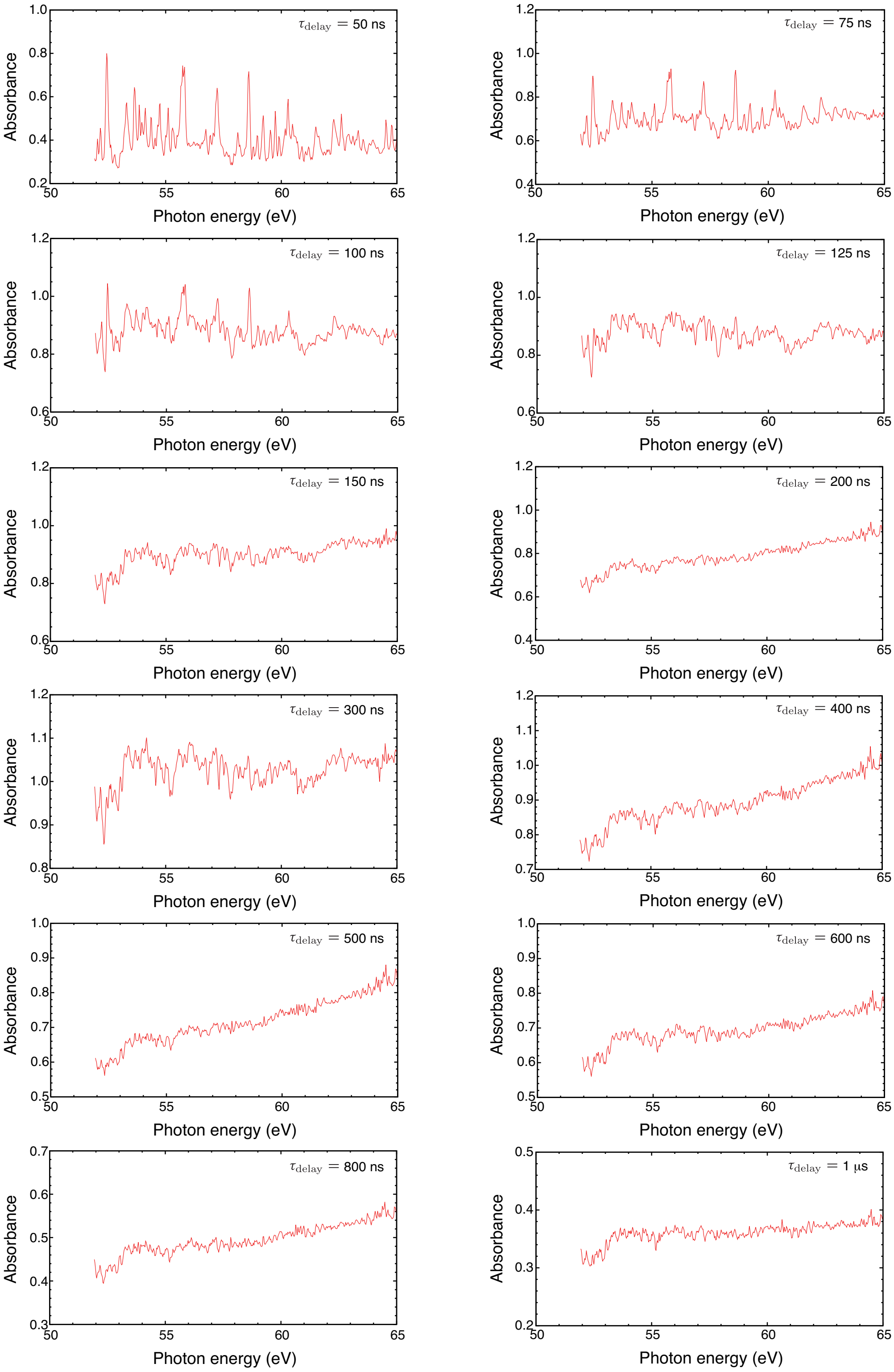

Figure 7.4 Absorbance of bismuth plasmas at different delay times.

7.3.1 Comparison with Cowan code calculations

Figures 7.5(a) and 7.6(a) show absorption spectra at delay times of 125 ns and 400 ns. These spectra were normalised to the maximum intensity in the photon energy range 150-200 eV. Relatively intense narrow absorption lines have been observed in this spectral region. As can be seen from the figure, some lines in figure 7.5(a) disappeared or weaken in figure 7.6(a), and the ratio of the intensity changes. This is due to the different dstribution of ions in the plasmas.

The Cowan code was employed to identify the features observed [3]. As described already, absorption lines of Bi IV were observed in the photon energy range 50-65 eV. Thus, it was assumed that the maximum ion stage was Bi IV. Calculated $4f$ inner-shell electrical dipole allowed transitions from the ground state in Bi I to Bi IV were as follows:

$$\begin{aligned}
\mathrm{Bi\,I}: 4f^{14}5s^25p^65d^{10}6s^26p^3 &\rightarrow 4f^{13}5s^25p^65d^{10}6s^26p^3nd\ (n \geq 6)\\
&\rightarrow 4f^{13}5s^25p^65d^{10}6s^26p^3mg\ (m \geq 5)\\
\mathrm{Bi\,II}: 4f^{14}5s^25p^65d^{10}6s^26p^2 &\rightarrow 4f^{13}5s^25p^65d^{10}6s^26p^2nd\ (n \geq 6)\\
&\rightarrow 4f^{13}5s^25p^65d^{10}6s^26p^2mg\ (m \geq 5)\\
\mathrm{Bi\,III}: 4f^{14}5s^25p^65d^{10}6s^26p &\rightarrow 4f^{13}5s^25p^65d^{10}6s^26pnd\ (n \geq 6)\\
&\rightarrow 4f^{13}5s^25p^65d^{10}6s^26pmg\ (m \geq 5)\\
\mathrm{Bi\,IV}: 4f^{14}5s^25p^65d^{10}6s^2 &\rightarrow 4f^{13}5s^25p^65d^{10}6s^2nd\ (n \geq 6)\\
&\rightarrow 4f^{13}5s^25p^65d^{10}6s^2mg\ (m \geq 5)
\end{aligned}$$

The calculated gf and convolved spectra of $4f \rightarrow nd$ ($n \geq 6$) and $4f \rightarrow mg$ ($m \geq 5$) transition arrays from Bi I to Bi IV ions are shown in figures 7.5 and 7.6. The gf values of transitions of the type $4f \rightarrow mg$ were lower than those of transitions of the type $4f \rightarrow nd$. Because of the large centrifugal repulsion for $l = 4$ the radial overlap between the $4f$ and mg wave functions will be close to zero and the resulting intensity will be lower.

From the calculations shown in figure 7.5 (b), it can be seen that absorption lines at 168 and 172.5 eV are attributable to Bi II, and absorption lines at 171.5 and 178 eV come from Bi III and Bi IV, respectively. The structure of the observed photoabsorption spectra above 180 eV is complicated, however, it seems to be associated with Bi III and Bi IV.

From the calculations shown in figure 7.6 (b), it can be also found that absorption lines at 168 and 172.5 eV are attributable to Bi II. However, the other structures in the observed photoabsorption spectra could not be identified. Moreover, absorption lines from neutral bismuth were not observed experimentally. It may be necessary to vary the height of the continuum source above the absorber target to allow observation of the Bi I spectrum.

The energies and gf values for $5p$ inner-shell electrical dipole allowed transitions were also calculated from the ground state for Bi I to Bi IV. The transitions were as follows:

$$\begin{aligned}
\mathrm{Bi\,I}: 5s^2 5p^6 5d^{10} 6s^2 6p^3 &\rightarrow 5s^2 5p^6 5d^{10} 6s^2 6p^3 ns \; (n \geq 7) \\
&\rightarrow 5s^2 5p^6 5d^{10} 6s^2 6p^3 md \; (m \geq 6) \\
\mathrm{Bi\,II}: 5s^2 5p^6 5d^{10} 6s^2 6p^2 &\rightarrow 5s^2 5p^6 5d^{10} 6s^2 6p^2 ns \; (n \geq 7) \\
&\rightarrow 5s^2 5p^6 5d^{10} 6s^2 6p^2 md \; (m \geq 6) \\
\mathrm{Bi\,III}: 5s^2 5p^6 5d^{10} 6s^2 6p &\rightarrow 5s^2 5p^6 5d^{10} 6s^2 6pns \; (n \geq 7) \\
&\rightarrow 5s^2 5p^6 5d^{10} 6s^2 6pmd \; (m \geq 6) \\
\mathrm{Bi\,IV}: 5s^2 5p^6 5d^{10} 6s^2 &\rightarrow 5s^2 5p^6 5d^{10} 6s^2 ns \; (n \geq 7) \\
&\rightarrow 5s^2 5p^6 5d^{10} 6s^2 md \; (m \geq 6)
\end{aligned}$$

Figure 7.7 shows the calculated gf spectra of Bi ions. The results predict that there is absorption in the photon energy range 80-150 eV. However, these spectra have yet to be observed in this research. It may be that the features do not appear in the spectrum due to lifetime broadening; similar behaviour has been observed in previous work on Pb III ions [6]. This work concluded that the decay process is substantially Auger decay and super-Coster-Kronig decay. This process is also similar to the $3p$ decay in the homologous Zn I isoelectronic sequence as indicated in the previous work on the M-shell photoabsorption of Ga^+ and Ge^{2+} [7, 8].

7.3.2 Comparison with RTDLDA calculations

In order to evaluate the photoabsorption cross section of Bi ions the relativistic time dependent local density approximation (RTDLDA) was employed [4, 5]. Figure 7.8 shows a comparison of experimentally observed absorption spectra and the calculated cross section of Bi^+ and Bi^{2+}. The calculated structures were similar to the experimental results and the cross sections did not change significantly with varying ion stage, resulting in maximum values of approximately 30 Mb at 65 eV. The calculated results show good agreement with experimental results, however, the narrow resonances were not observed in the experiment. These resonances are also predicted by the Cowan code, so a challenge is understanding the non-appearence of these lines.

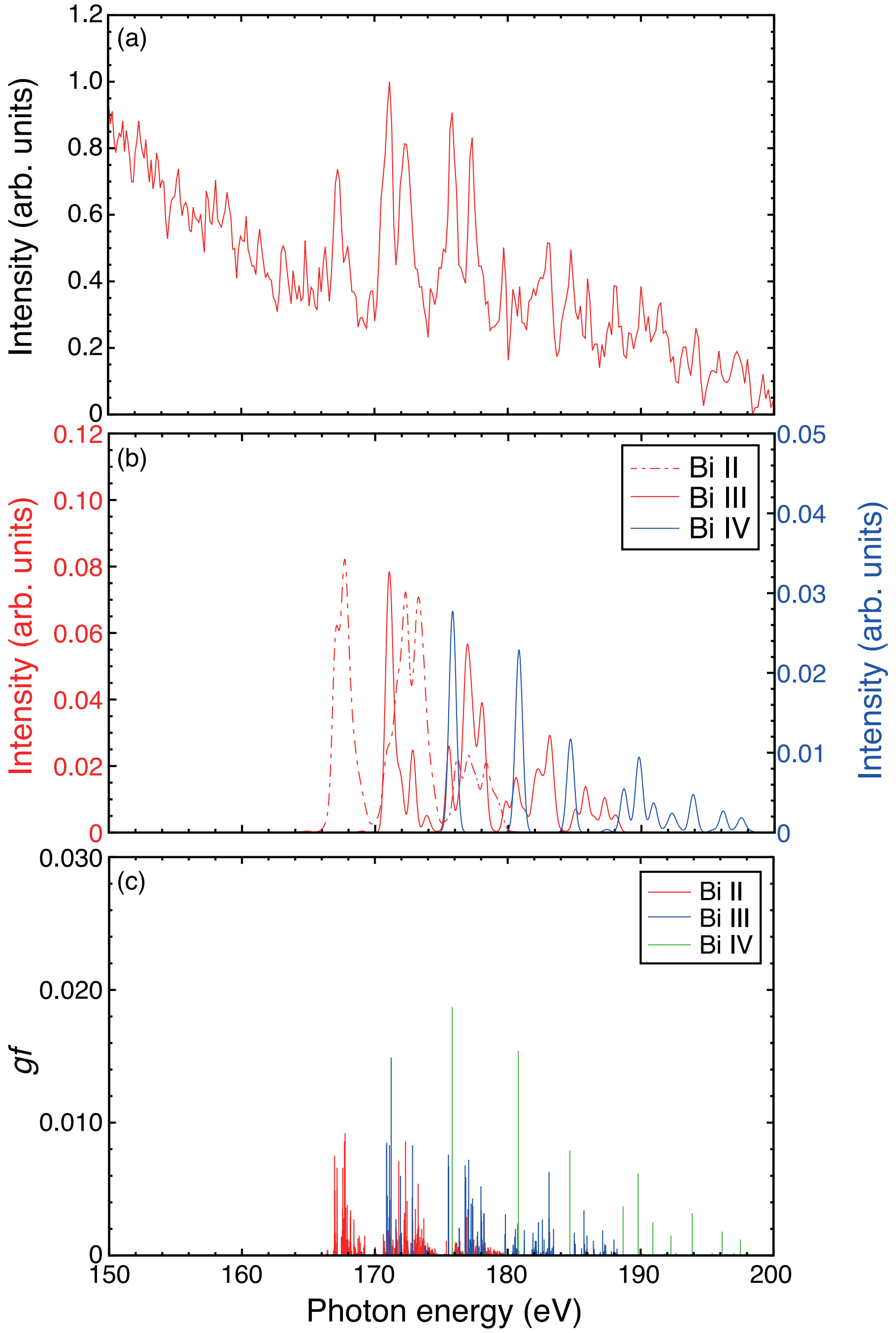

Figure 7.5 (a) Absorption spectra of a bismuth plasma at 125 ns. (b) Convolved spectra of Bi II, Bi III and Bi IV, (c) Calculated gf spectra of Bi II, Bi III and Bi IV.

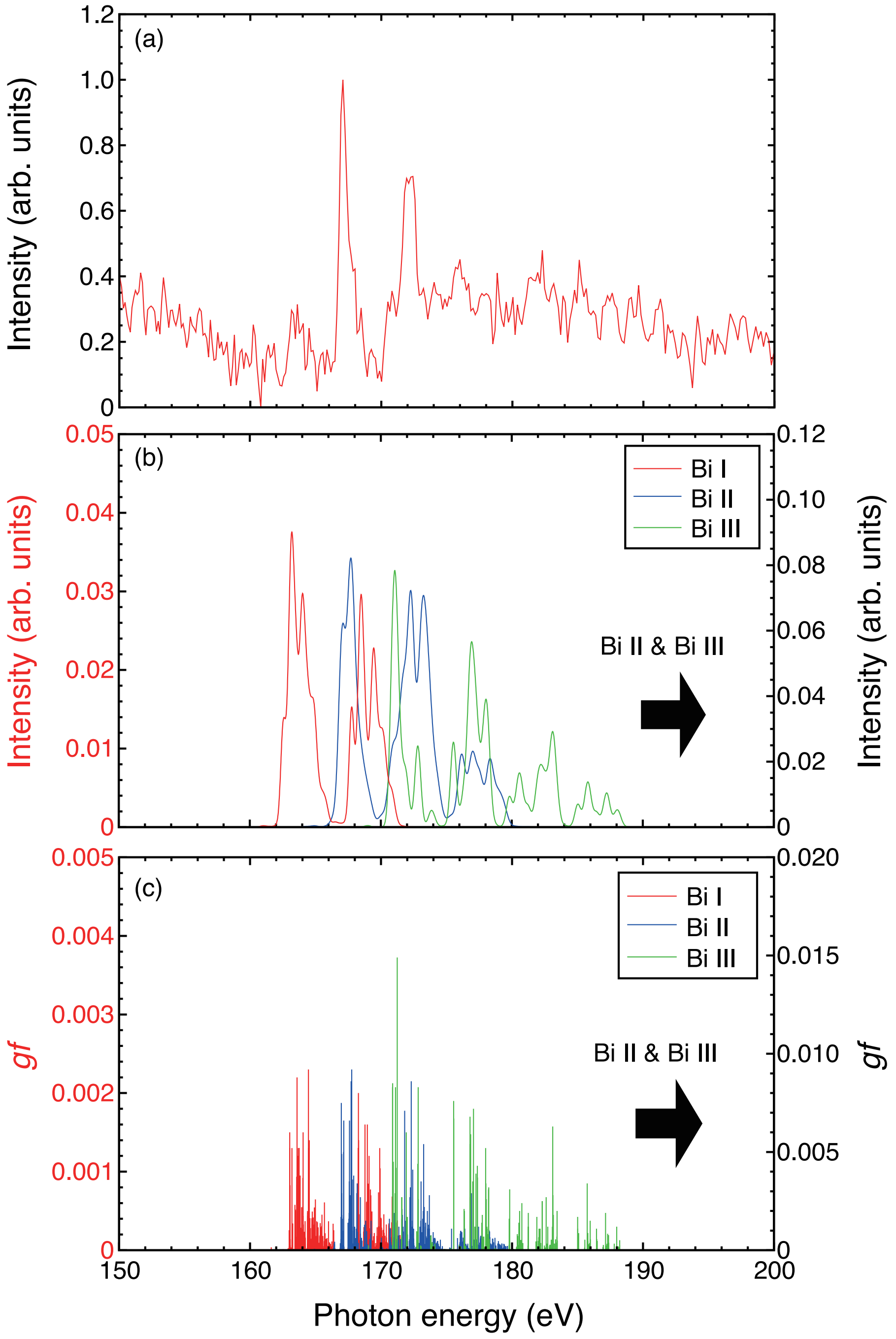

Figure 7.6 (a) Absorption spectra of a bismuth plasma at 400 ns. (b) Convolved spectra of Bi II, Bi III and Bi IV, (c) Calculated gf spectra of Bi II, Bi III and Bi IV.

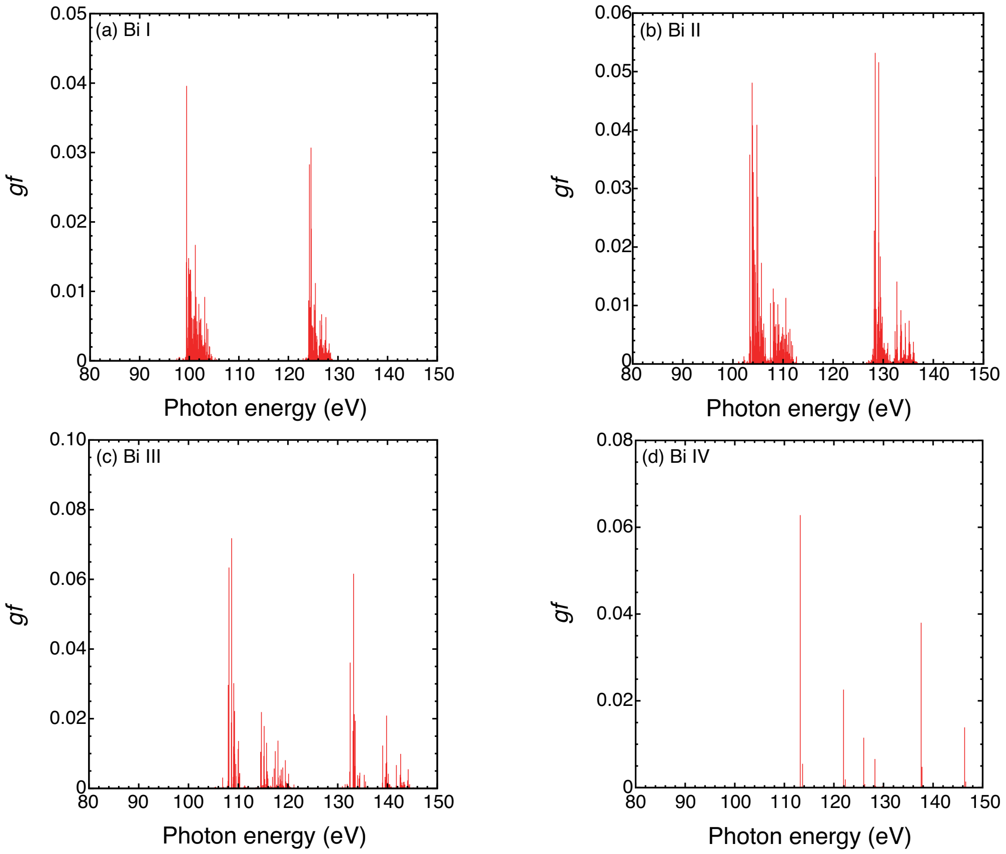

Figure 7.7 Calculated gf spectra of Bi ions for $5p$ inner-shell electrical dipole allowed transitions ($5p \rightarrow nd,\ ms$) of Bi ions.

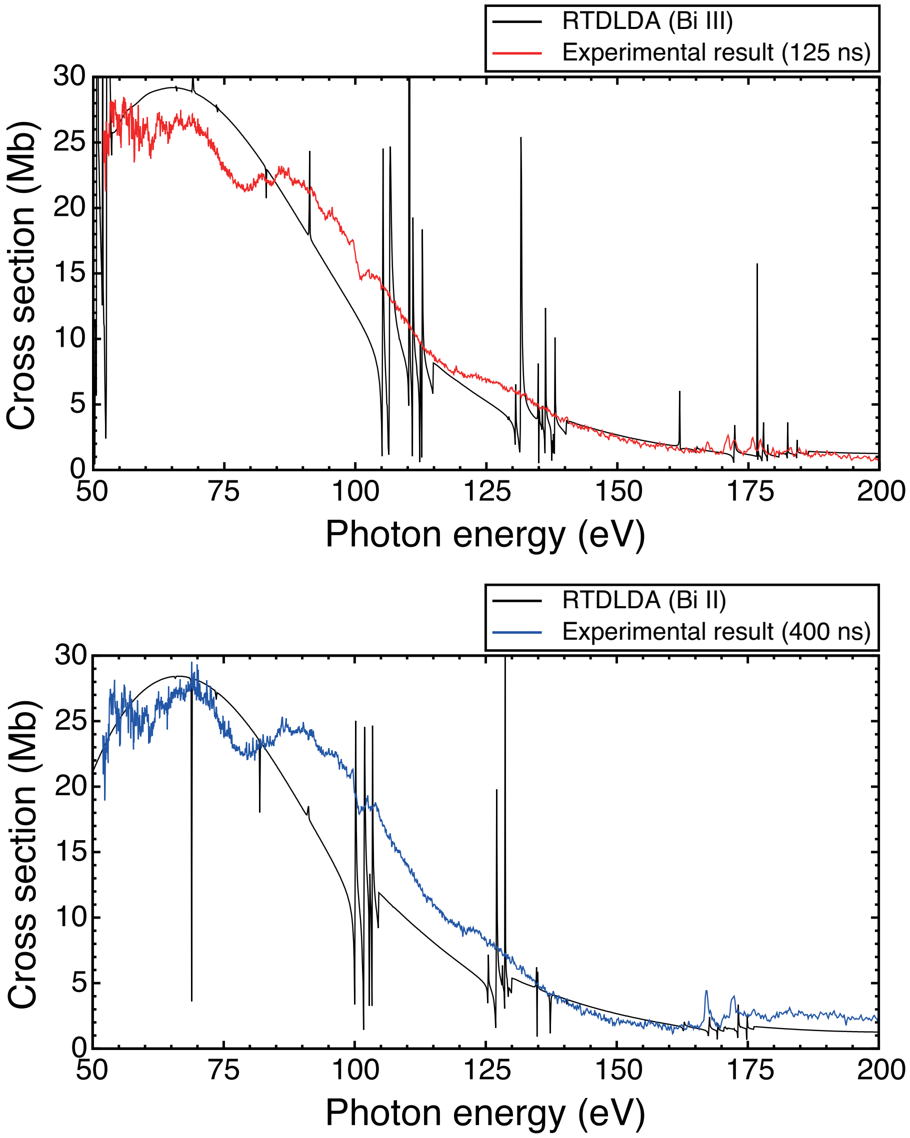

Figure 7.8 Calculated $4f$ photoabsorption cross section in (a) Bi III and (b) Bi II.

7.3.3 Conclusion

Photoabsorption spectra of Bi^{+}, Bi^{2+}, and Bi^{3+} ions have been observed in the $52 - 200$ eV photon energy region using the DLP technique.

Absorption lines observed in the 150–200 eV photon energy region were identified by comparison with Cowan code results. As a result, it was found that these lines come from $4f$ inner-shell excitations. Absorption lines at 168 and 172.5 eV are attributed to Bi^{+} ions, and absorption lines at 171.5 and 178 eV come from Bi^{2+} and Bi^{3+} ions, respectively. The structure of the observed photoabsorption spectra above 180 eV is complicated, however, it seems to be associated with Bi^{2+} and Bi^{3+} ions. Absorption lines from neutral Bi have yet to be observed experimentally. The observation of absorption lines associated with $4f$ inner-shell excitations is believed to be for the first time.

$5p$ inner-shell electrical dipole allowed transitions were also calculated from the ground state in Bi to Bi^{3+}. The results predict absorption in the photon energy range 80-150 eV. However, these features were not observed in this research, most likely due to the influence of fast decay processes, which remain to be calculated.

Photoabsorption cross sections of Bi ions were calculated by the RTDLDA method. The calculated results showed similar behaviour to the experimental observations and the photoabsorption cross sections did not change significantly with increasing ion stage, resulting in maximum values of approximately 30 Mb at 65 eV.

Finally, to develop water window sources, observation and evaluation of the photoabsorption spectra and photoabsorption cross section in the $280 - 516$ eV photon energy region must be carried out in the near future.

Reference

[1] C. Banahan, C. McGuinness, J. T. Costello, D. Kilbane, J-P Mosnier, E. T. Kennedy, G. O'Sullivan, and P. v. Kampen, "The 5d photoabsorption spectra of Pb III and Bi IV", J. Phys. B: At. Mol. Opt. Phys. **41**, 205001 (2008).

[2] D. Colombant and G. F. Tonon, "X-ray emisiion in laser-produced plasmas", J. Appl. Phys. **44**, 3524 (1973).

[3] R. D. Cowan, "THE THEORY OF ATOMIC STRUCTURE AND SPECTRA", (UNIVERSITY OF CALIFORNIA PRESS, 1981).

[4] A. Zangwill and D. A. Liberman, "A NONRELATIVISTIC PROGRAM FOR OPTICAL RESPONSE IN ATOMS USING A TIME- DEPENDENT LOCAL DENSITY APPROXIMATION", Comput. Phys. Commun. **32**, 63 (1984).

[5] D. A. Liberman and A. Zangwill, "A RELATIVISTIC PROGRAM FOR OPTICAL RESPONSE IN ATOMS USING A TIME-DEPENDENT LOCAL DENSITY APPROXIMATION", Comput. Phys. Commun. **32**, 75 (1984).

[6] C. McGuiness, "The XUV Photoabsorption and Photoionisation Spectra of Selected Ions: Techniques, Results and Theory", (PhD. thesis, School of Physics, University College Dublin, 1996).

[7] P. Dunne, G. O'Sullivan, and V. K. Ivanov, "Extreme-ultraviolet absorption spectrum of Ga^+", Phys. Rev. A **48**, 4358 (1993).

[8] P. Dunne, G. O'Sullivan, and V. K. Ivanov, "The M-shell photoabsorption spectrum of Ge^{2+}", J. Phys. B: At. Mol. Opt. Phys. **28**, 1241 (1995).

Chapter 8

Conclusions and Future Work

Emission and absorption spectra of gadolinium and bismuth plasmas were studied in this research.

The peak emission wavelength from gadolinium and terbium plasmas, which may drive next generation lithography sources at 6.x nm, were 6.8 nm and 6.5 nm, respectively [1, 2]. Four 13.5 nm from tin plasma sources, there are Mo/Si mirrors with maximum reflectivity at 13.5 nm. However, the La/B_4C mirror for 6.x nm [3, 4], has a peak reflectivity which is slightly displaced from the emission maxima of both elements.

In the photoabsorption spectra of gadolinium ions, the $4d$ giant resonance was observed. This supports the observation of the angular dependence of the emission spectra of Gd plasmas, observed in previous research [5]. Development of 6.x nm sources should follow the path of varying the wavelength of the laser pulse and target conditions as has been done for tin based plasma sources.

The UTA peak wavelength depends on atomic number of the target material. Emission spectra from Bi plasmas were observed to have a UTA peak around 4 nm attributable to $4d - 4f$ transitions. Calculated results in a previous report also predict strong UTA emission at 3.3 nm attributable to $4p - 4d$ transitions for plasma temperatures higher than 900 eV [6]. However, this UTA emission has yet to be observed, except for small enhancement in the dual-pulse irradiation experiment. Possible reasons for not observing this feature are: the optical thickness of the Bi plasma itself, an inability to reach a sufficiently high plasma temperature, and difference of excitation mechanisms.

The in-band SXR energy, spectral purity and conversion efficiency for 3.3, 4.0 and 4.4 nmwere presented in this research. The results were shown to be in agreement with calculations using the CR-model [7], resulting in optimum laser power density of $4 \times 10^{13} \mathrm{W/cm^2}$. Development of water-window sources should follow the path of varying the wavelength of the laser pulse and target conditions as has been done for tin based plasma sources.

Photoabsorption spectra of Bi ions in the photon energy range 52-200 eV were observed, showing $4f$ photoabsorption in good agreement with numerical calculation by Cowan code [8]. However, $5p$ photoabsorption spectra have yet to be observed. The structure of the photoabsorption spectra were similar to RTDLDA calculation [9, 10] results and the cross sections did not change significantly with increasing ionisation, resulting in maximum values of approximately 30 Mb at 65 eV. The photoabsorption cross section of Bi ions were seen to be lower at higher photon energies. To develop water window sources based on bismuth, both observation and evaluation of photoabsorption spectra and photoabsorption cross sections in the $280-516$ eV photon energy region must be carried out in the future. The observation of absorption lines associated with $4f$ inner-shell excitations is believed to be new.

Figure 8.1 shows preliminary experimental results regarding (a) angular dependence of spectra and (b) photoabsorption spectra of Bi ions in the $100-450$ eV photon energy region. It was found that emission spectra do not depend on the viewing angle and the the photoabsorption cross section is not high for singly or doubly ionised ions. Further analysis and experiments will be performed in the near future.

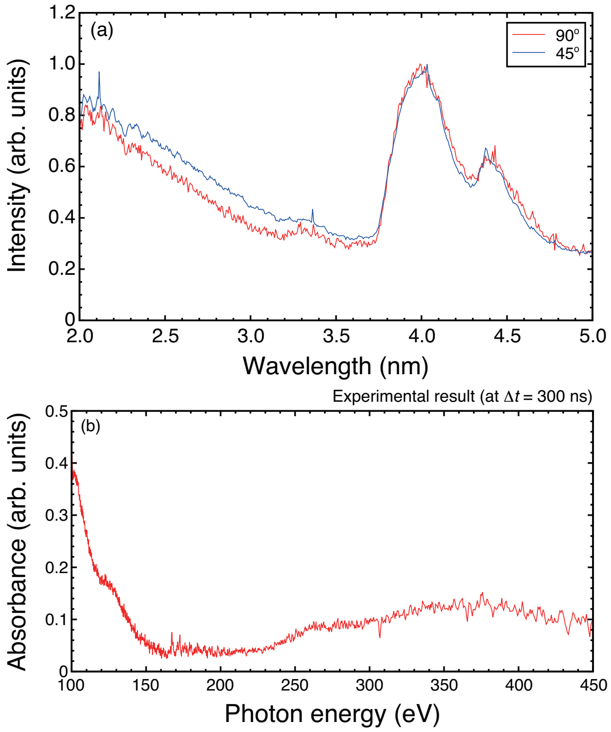

Figure 8.1 (a) Emission spectra from highly ionised bismuth plasmas observed at different viewing angle. (b) The photoabsorption spectra of Bi ion in the 100−450 eV photon energy region.

Reference

[1] T. Otsuka, D. Kilbane, J. White, T. Higashiguchi, N. Yugami, T. Yatagai, W. Jiang, A. Endo, P. Dunne, and G. O'Sullivan, "Rare-earth plasma extreme ultraviolet sources at 6.5-6.7 nm", Appl. Phys. Lett. **97**, 111503 (2010).

[2] T. Otsuka, D. Kilbane, T. Higashiguchi, N. Yugami, T. Yatagai, W. Jiang, A. Endo, P. Dunne, and G. O'Sullivan, "Systematic investigation of self-absorption and conversion efficiency of 6.7 nm extreme ultraviolet sources", Appl. Phys. Lett. **97**, 231503 (2010).

[3] S. S. Andreev, M. M. Barysheva, N. I. Chkhalo, S. A. Gusev, A. E. Pestov, V. N. Polkovnikov, D. N. Rogachev, N. N. Salashchenko, Yu. A. Vainer, and S. Yu. Zuev, "Multilayer X-Ray Mirrors Based on La/B_4C and La/B_9C", Tech. Phys. **55**, 1168 (2010).

[4] V. V. Medvedev, R. W. E. van de Kruijs, A. E. Yakshin, N. N. Novikova, V. M. Krivtsun, E. Louis, A. M. Yakunin, and F. Bijkerk, "Multilayer mirror with enhanced spectral selectivity for the next generation extreme ultraviolet lithography", appl. Phys. Lett. **103**, 221114 (2013).

[5] C. O'Gorman, T. Otsuka, N. Yugami, W. Jiang, A. Endo, B. Li, T. Cummins, P. Dunne, E. Sokell, G. O'Sullivan, and T. Higashiguchi, "The effect of viewing angle on the spectral behavior of a Gd plasma source near 6.7 nm", Appl. Phys. Lett. **100**, 141108 (2012).

[6] T. Higashiguchi, T. Otsuka, N. Yugami, W. Jiang, A. Endo, B. Li, P. Dunne, and G. O'Sullivan, "Feasibility study of broadband efficient "water window" source", Appl. Phys. Lett. **100**, 014103 (2012).

[7] D. Colombant and G. F. Tonon, "X-ray emisiion in laser-produced plasmas", J. Appl. Phys. **44**, 3524 (1973).

[8] R. D. Cowan, "THE THEORY OF ATOMIC STRUCTURE AND SPECTRA", (UNIVERSITY OF CALIFORNIA PRESS, 1981).

[9] A. Zangwill and D. A. Liberman, “A NONRELATIVISTIC PROGRAM FOR OPTICAL RESPONSE IN ATOMS USING A TIME- DEPENDENT LOCAL DENSITY APPROXIMATION”, Comput. Phys. Commun. **32**, 63 (1984).

[10] D. A. Liberman and A. Zangwill, “A RELATIVISTIC PROGRAM FOR OPTICAL RESPONSE IN ATOMS USING A TIME-DEPENDENT LOCAL DENSITY APPROXIMATION”, Comput. Phys. Commun. **32**, 75 (1984).

Acknowledgement

First of all, I would like to thanks Prof. Noboru Yugami and Prof. Padraig Dunne for their guidances, advices. Especially, I would like to thank Prof. Padraig Dunne for reviewing my thesis which was written in Japanese english, "Japanish".

I would like to thanks Prof. Gerry O'Sullivan, Prof. Takeshi HIgashiguchi, Dr. Emma Sokell, Dr. Fergal O'Reilly, Dr. Tom McCormack also. I could not carry out experiment without your idea, and summarise without your help.

I had the very good fortune that I could meet really nice colleague and friends in Ireland. I would like to thanks everyone who worked with me. I owe a special thanks to Dr. Paddy. Sorry for always asking silly questions, thank you for your patient help. Huge thanks to Dr. Tony, Dr. Bhuvan, Dr. Niksa, Dr. Paul, Dr. Ken, Dr. Oran, Dr. Deirdre and Dr. Rebekah. Colm and Thomas, I couldn't survive without your help and guidance. Thanks a lot. Also big thanks to SpecLab., Rob, Enda, Elaine, Girum, Li, Niall and Frank. Ah, lads, thanks, Jay, GB, Fee. Experiences in Ireland are my treasure. I would never forget your help and guidances. Thank you, thank you, thank you so much.

I was very lucky to have a great colleague in Utsunomiya University. First, endless thanks to Dr. Hiromitsu Terauchi. If you had been not in PhD course, I wouldn't have decided to enter the course. I also owe a huge thanks to Mami, Tsuchiya, Yamamoto, Irino, Kameda, Takafumi, Fuminori, Nakata, Kasama, Anno, Miyazawa, Kikuchi and Nagata. Discussing, eating, sleeping, getting chewed out, making presentation, carrying out experiment, we were always together when we were master's course student. That times are my origin of my scientific life. I would never forget. Thank you. And all of the people who were in our lab., (too many to write here). Thanks a lot. I hope you have a great life.

I am sorry if your name were not here. But I appreciate your help and guidance to here. Thank you.

Finally, I would like to thanks my family, Dad, Mam, Grandma, Sister, Aunt, Uncle, Cousins, Cats and Dog. Now, I am on the start line of my life. I don't know what is waiting in my way. Anyway, I will do it. I would never forget your support. Thank you.

This work was supported by JSPS KAKENHI Grant Number 24·10265.